Indentation and Wear Behavior of Superelastic TiNi Shape Memory Alloy

by

Rabin Neupane

Submitted in partial fulfilment of the requirements
for the degree of Master of Applied Science

at

Dalhousie University
Halifax, Nova Scotia
March 2014

TABLE OF CONTENTS

LIST OF TABLES

LIST OF FIGURES

ABSTRACT

TiNi shape memory alloy is characterized by shape memory and superelastic effects which occur due to reversible martensite transformation. It has been recently found that TiNi alloy has superior dent and wear resistance compared to other conventional materials. The stress-induced martensite transformation exhibited by this alloy contributes to its dent and wear resistance. Much work is required to establish the fundamental principals governing the superelastic behavior of TiNi under wear and indentation conditions. Understanding the superelastic behavior helps to employ superelastic TiNi in applications where high impact loading is expected as in gears and bearings. In this study the superelastic behavior of shape memory alloys under reciprocating sliding wear and indentation loading conditions was investigated. The deformation behavior of superelastic Ti-Ni alloys was studied and compared to AISI 304 stainless steel. Dominant wear and deformation mechanisms were identified.

LIST OF ABBREVIATIONS AND SYMBOLS USED

Symbols	Description
μ	Coefficient of friction
τ_s	Surface shear strength
σ	Uniaxial Stress
σ_f	Detwinning finish stress
σ^{Af}	End stress for reverse transformation into austenite
σ^{As}	Start stress for reverse transformation into austenite
σ^{Mf}	End stress for forward transformation into martensite
σ^{Ms}	Start stress for forward transformation into martensite
σ_s	Detwinning start stress
σ_y	Yield strength (MPa)
ε	Strain
a	Contact radius (m)
A	Contact area (m^2)
A_f	Austenite finish temperature (°C)
A_s	Austenite start temperature (°C)
AISI	American Iron and Steel Institution
B19’	Martensite phase
B19	Intermediate martensite phase
B2	Austenite phase
C	Indentation Depth
COF	Coefficient of friction
E	Young’s Modulus
EDS	Energy Dispersive x-ray Spectroscopy
F	Force (N)
F_N	Applied load
F_X	Tangential load (N)
F_Z	Normal load (N)
h	Displacement (m)

H	Hardness
k	Specific wear rate
K	Wear coefficient
M_d	Superelastic temperature limit
M^d	Detwinned martensite
M_f	Martensitic finish temperature (°C)
M_s	Martensitic start temperature (°C)
M^t	Twinned martensite
MEMS	Micro-electro-mechanical Systems
Ni	Nickel
N	Newton
P	Indenter load
R	Effective Radius (m)
s	Sliding distance
SE	Superelasticity
SEM	Scanning Electron Microscopy
SMA	Shape Memory Alloy
SME	Shape Memory Effect
SIM	Stress-induced Martensite
T	Temperature (°C)
Ti	Titanium
TiNi	Titanium Nickel
UMT	Universal Micro-Tribometer
v	Poisson's Ratio
W	Volume worn per unit sliding distance
WC	Tungsten carbide
XRD	X-Ray Diffraction

ACKNOWLEDGEMENTS

The author would like to acknowledge the guidance, words of encouragement and unwavering support offered by Dr. Zoheir Farhat throughout the entirety of this project. The author would like to thank the Natural Sciences and Engineering Research Council of Canada (NSERC) for financial support. The efforts of Dr. Paul Bishop and Dr. Robert Bauer are greatly appreciated. Furthermore, the author would like to thank the materials engineering group at Dalhousie University, including Md. Aminul Islam. The excellent technical advice and contributions offered by Mr. Dean Grijm and Mrs. Patricia Scallion is greatly appreciated.

Finally, the author would like to acknowledge the support of his family and friends, who have always been there for him throughout his academic career.

1 INTRODUCTION

Overview and Objective

TiNi shape memory alloy was discovered by Buehler and coworkers at the Naval Ordnance Laboratory while working on heat shielding materials and was named "NiTiNOL" (Kumar & Lagoudas, 2008). Shape memory alloys are materials characterized by shape memory effect and pseudoelasticity (superelasticity). TiNi alloy exhibits shape memory and superelasticity at different temperatures, i.e., shape memory is achieved at low temperature while superelasticity at higher temperature (Lagoudas, 2008). Materials exhibiting superelastic effect show high recoverable strain during deformation due to stress-induced martensitic transformation. During loading, the austenite phase transforms to detwinned martensite accompanied by large deformation. The reverse transformation from martensite to austenite occurs upon unloading, accompanied by large recoverable strain. Superelastic TiNi alloy has the capacity to accommodate high impact loading without permanent deformation. That is, upon unloading both elastic and pseudoelastic deformation are recoverable. In the case of conventional materials, upon loading material goes through recoverable elastic deformation, followed by non-recoverable plastic deformation and only elastic deformation is recovered during unloading (Li, 1998).

TiNi is widely used in a variety of applications in automotive, aerospace, and biomedical industries due to their high corrosion resistance, good fatigue properties, high mechanical damping and good ductility. Recent studies have shown that superelastic TiNi has superior wear and dent resistance compared to other conventional materials. The superior wear resistance of superelastic TiNi alloy was attributed to its stress-induced martensitic transformation, i.e, low E/H ratio, high deformation recovery and large contact area (Farhat & Zhang, 2010).

Furthermore, in addition to dent resistance, denting rate (loading rate) is also of significant importance to applications where denting is expected. Substantial amount of work has been done towards understanding the effect of strain rate under tensile properties i.e. uniaxial loading, of superelastic TiNi. But, only limited work has been done on investigating the dependency of superelasticity on loading rate of TiNi under

indentation loading i.e. under localized compressive load. Understanding the indentation behavior helps increase the utilization of shape memory alloys in applications where high loading rate, high wear, and denting are common, as in gears and bearings. A recent study has shown a relationship between loading rate and superelasticity under indentation loading ((Amini, He, & Sun, 2011), (Shahirnia, Farhat, & Jarjoura, 2011)). The objective of the present work is to investigate the dent and wear resistance of superelastic Ti-Ni alloys. Further, the effect of loading rate (i.e., denting rate) on superelasticity will be assessed. Also, an attempt will be made to enhance the current interpretation of indentation data for superelastic alloys through the coupling of deformation and reversible martensitic transformation that take place during indentation loading.

To achieve the objective of this work, the superelastic effect of Ti-Ni alloys under reciprocating and indentation conditions was investigated. Wear tests were performed under different normal loads, reciprocating frequencies, and time intervals, while indentation tests were performed under various loading conditions using spherical and sharp indenters.

The organizational outline of this thesis is as follows. A review of shape memory alloys, crystal structure, martensitic phase transformation, mechanical behavior, effects of indentation loading conditions, and wear behavior are provided in Chapter 2. Materials and experimental methods used to achieve the research objectives are outlined in detail in Chapter 3. Experimental results and relevant discussions are given in Chapter 4. Conclusions of this research and recommendations for future work are summarized in Chapter 5.

2 LITERATURE REVIEW

2.1 TiNi Shape Memory Alloy

TiNi shape memory alloys are widely known for shape memory and superelastic effects which occur due to reversible martensitic transformation. The superelastic effect of TiNi is characterized by large recoverable deformation associated with reversible stress-induced martensitic transformation. The reversible martensite transformation takes place as a result of applied heat or mechanical load (Kumar & Lagoudas, 2008). TiNi alloy exhibits shape memory at low temperature and superelastic behavior at higher temperature.

TiNi alloy has been widely used in a variety of applications, such as, automotive, aerospace, biomedical and micro-electro-mechanical systems (MEMS). It has been recently found that TiNi alloy has superior wear resistance compared to other conventional materials such as steels, Ni-based, and Co-based tribo-alloys ((Li, 1998), (Zhang & Farhat, 2009). Superelastic TiNi alloy has high ability to accommodate large scale deformation without generating permanent damage (Li, 1998). In the case of conventional materials wear and indentation resistance depend on their mechanical properties like strength, hardness, toughness, ductility, work hardening and crystallography texture ((Li, 1998), (Zhang & Farhat, 2009), (Li, 2000)). However, for superelastic TiNi stress-induced martensitic transformation also contributes to the dent and wear resistance. This behavior makes the understanding of wear and denting behavior of superelastic TiNi difficult.

Previous studies showed that superelasticity of TiNi alloy is considerably affected by testing conditions during wear, i.e. tribo-system. The role of reversible martensite transformation in the wear process of TiNi is studied by Farhat et al ((Farhat & Zhang, 2010). They performed sliding wear tests on Ti, Ni, AISI 304 stainless steel and TiNi at sliding speed of 40 m/min and a normal load of 40N at room temperature. Amongst all the materials tested, TiNi exhibited the lowest wear rate whereas Ti showed the highest. High elastic recovery ratio and low E/H contributed to the superior wear resistance of TiNi ((Li, 1998) (Farhat & Zhang, 2010)). Lin, et al (Lin, He, Chen, Liao, & Lin, 1997) investigated the effect of various loads on the wear characteristics of TiNi shape memory alloy. Their results showed that during sliding wear, weight loss increases with increasing

load according to Archard's law (Archard, 1953). They suggested that under low loads, the interface between the martensite and parent austenite phase is fairly mobile and the strain is within the superelastic strain range. However, under high loads superelasticity is not completely functional and deformation occurs by slip. Further, recent studies have shown a relationship between loading rate and superelasticity under indentation conditions ((Amini & Sun, 2010), (Amini, He, & Sun, 2011), (Shahirnia, Farhat, & Jarjoura, 2011)). However, much work is needed to understand the effect of loading rate under indentation loading of superelastic TiNi alloy.

2.2 Phase Diagram and Crystal Structures of TiNi

To improve the shape memory and superelastic characteristics of TiNi alloys, understanding their phase diagram is essential (Otsuka & Ren, 2005). It was Laves and Wallbaun (Vogel & Wallbaum, 1938) who discovered a single phase TiNi at high temperature having equiatomic composition and bounded by Ti_2Ni and $TiNi_3$ phases. Later the decomposition of TiNi into Ti_2Ni and $TiNi_3$ at temperature 650^o C and 800^o C was first reported by Duwez and Taylor (Duwezand & Talor, 1950). Detail examination of the phase diagram by Poole and Hume-Rothery (Poole & Hume-Rothery, 1954) determined the solubility limits of TiNi alloy at higher temperature above 900^o C and found very steep boundary on Ti-rich side close to 50Ni, whereas significant decline in solubility on Ni-rich side with lowering temperature. Further investigations led to confirmation of eutectoid decomposition of TiNi into Ti_2Ni and $TiNi_3$, which was previously observed by Duwez and Taylor. Purdy and Parr (Purdy & Parr, 1961), observed reversible transformation i.e. TiNi phase transforms to π phase, which occurs at low temperature. Nishida et al. studied diffusion controlled transformation on Ti-52Ni alloy at high temperature and found that Ti_3Ni_4, Ti_2Ni_3, and $TiNi_3$ phases may exist depending upon aging temperature and time (Nishida, Wayman, & Honma, 1986). After being controversial for more than three decades, the most reliable TiNi phase diagram was created and is shown in Figure 2.1. The shape memory and superelastic characteristics are exhibited by the alloy having equiatomic composition in the central region bounded by Ti_2Ni and $TiNi_3$ phases.

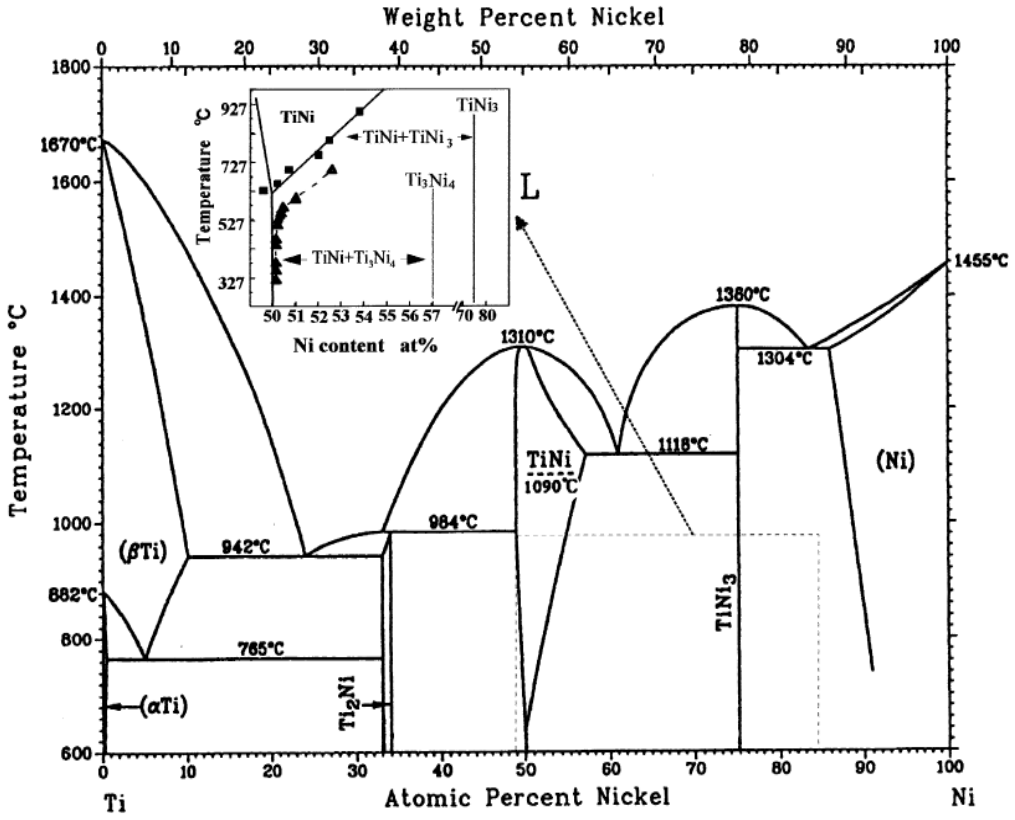

Figure 2.1 Phase diagram of TiNi (Otsuka & Ren, 2005)

2.2.1 Martensite

Martensite is a low temperature phase of TiNi and has different crystal structure from the austenite phase of TiNi. Martensite (B19') has monoclinic crystal structure and is more stable compared to an intermediate martensite phase (B19, orthorhombic crystal structure) as shown in Figures 2.2 and 2.3 (Otsuka & Ren, 2005). An intermediate B19 martensite phase forms before B19' martensite phase. The martensite phase can have different crystal structures based on the compositions and alloying elements. This type of transformation occurs due to shear lattice distortion (Kumar & Lagoudas, 2008).

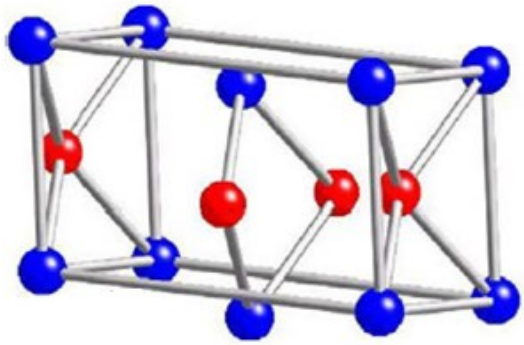

Figure 2.2 Crystal structure of B19 martensite (Guda Vishnu & Strachan, 2010)

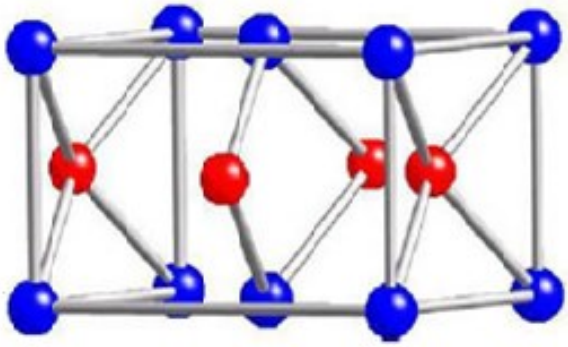

Figure 2.3 Crystal structure of B19' martensite (Guda Vishnu & Strachan, 2010)

Crystals that are formed during martensitic transformation can have different orientations, which are called variants. Martensitic crystals exist in two forms, twinned martensite (M^t) and detwinned martensite (M^d) (Figures 2.4 and 2.5). Twinned martensite is formed by combination of "self-accommodated" martensitic variants (Kumar & Lagoudas, 2008) and detwinned martensite is reoriented martensitic variants that grow at the expense of other less favorable oriented variants.

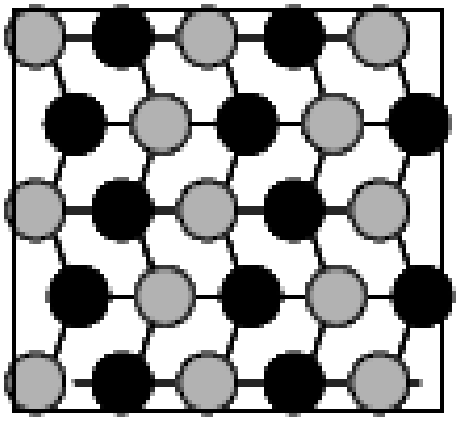

Figure 2.4 Twinned Martensite (Kumar & Lagoudas, 2008)

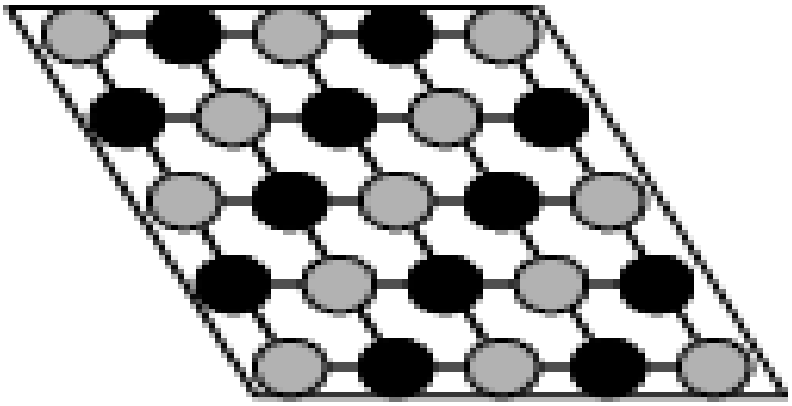

Figure 2.5 Detwinned Martensite (Kumar & Lagoudas, 2008)

2.2.2 Austenite

Austenite is a high temperature phase of TiNi as compared to martensite phase and has cubic crystal structure, B2 (Figure 2.6). B2 has a lattice constant of 0.3015 nm at room temperature. Being a parent phase, austenite (B2) plays an important role in martensitic transformation and is also associated with shape memory behavior.

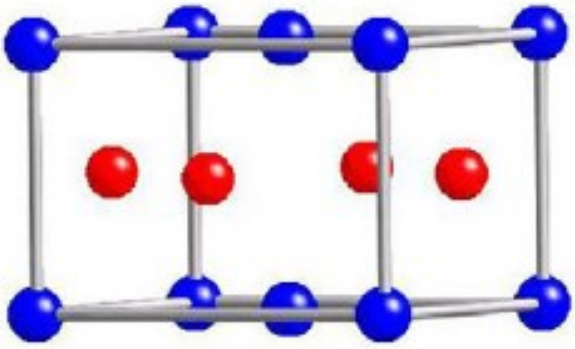

Figure 2.6 Austenite, parent phase of TiNi (Guda Vishnu & Strachan, 2010)

2.2.3 R-Phase

R-phase forms before B19' martesnite phase during martensitic phase transformation under specific conditions and has a trigonal crystal structure. The R-phase transformation phenomenon is linked to shape memory and superelastic effects of shape memory alloys. R-phase transformation is characterized by a sudden increase in electrical resistivity of TiNi.

2.3 Martensite Phase Transformation in TiNi

Martensitic transformation is defined as a transformation from one structure to another by diffusionless shear displacement, i.e. shear lattice distortion. As stated above, TiNi shape memory alloy exhibits shape memory and superelastic effects due to reversible martensite phase transformation. The phase transformation of TiNi can be induced either by heating or mechanical loading.

Temperature induced martensitic phase transformation is associated with four characteristic temperatures, M_s (martensite start), M_f (martensite finish), A_s (austenite start), and A_f (austenite finish). During phase transformation, TiNi alloy is cooled from the parent austenite phase, to a temperature below M_f without applying any mechanical load, to form twinned martensite. As stated above, martensite is a low temperature phase with a low geometrical symmetry, while austenite is a high temperature phase with a high geometrical symmetry. Hence, twinned martensite is formed by combination of self-accommodated martensite variants. This transformation from the austenite phase to the martensite phase is called forward transformation. Upon heating to a temperature above A_f, martensite transforms back to austenite, hence the transition is called reverse

transformation. During phase transformation, macroscopic shape changes are negligible because each variant of a group of variants accommodate the strains of the other variants. The phase transformation from austenite to martensite and martensite to austenite occurs upon cooling and heating, respectively. The diagram representing temperature induced phase transformation without mechanical load is shown in Figure 2.7.

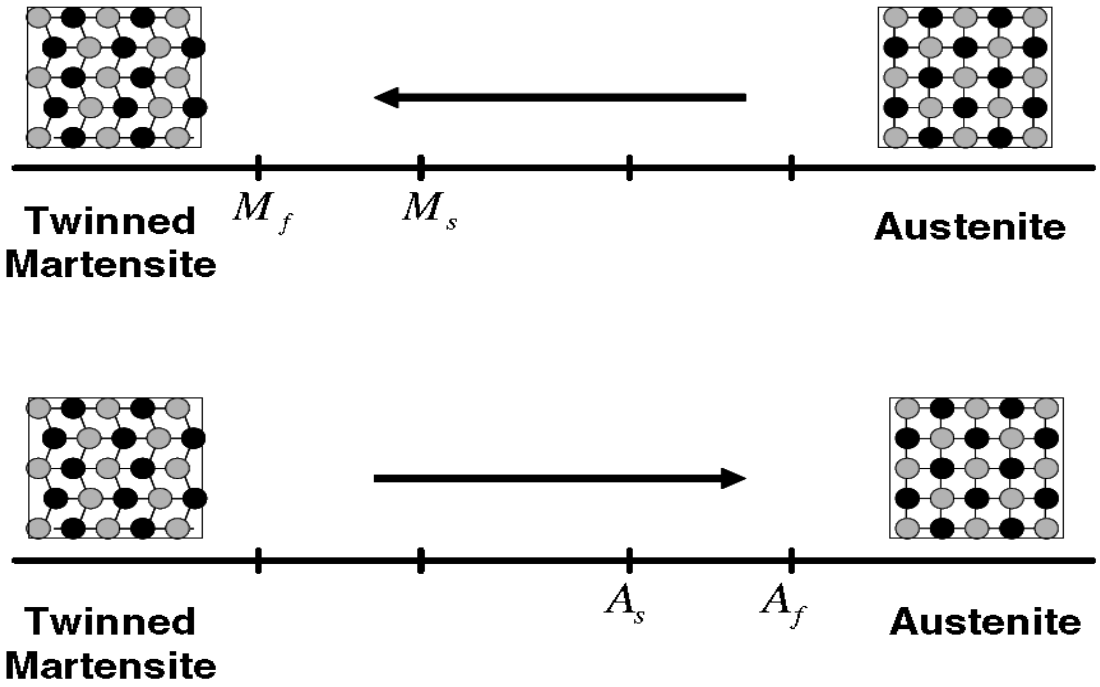

Figure 2.7 Temperature induced phase transformation of TiNi without mechanical load (Kumar & Lagoudas, 2008)

When external stress is applied to twinned martensite, it transforms to detwinned martensite due to reorientation of variants. The detwinning process results in macroscopic shape changes which remain after unloading. The detwinning process of TiNi with an applied stress is shown is Figure 2.8. Upon heating to a temperature above A_f, a reverse transformation occurs and detwinned martensite transforms back to austenite with complete shape recovery (Figure 2.9).

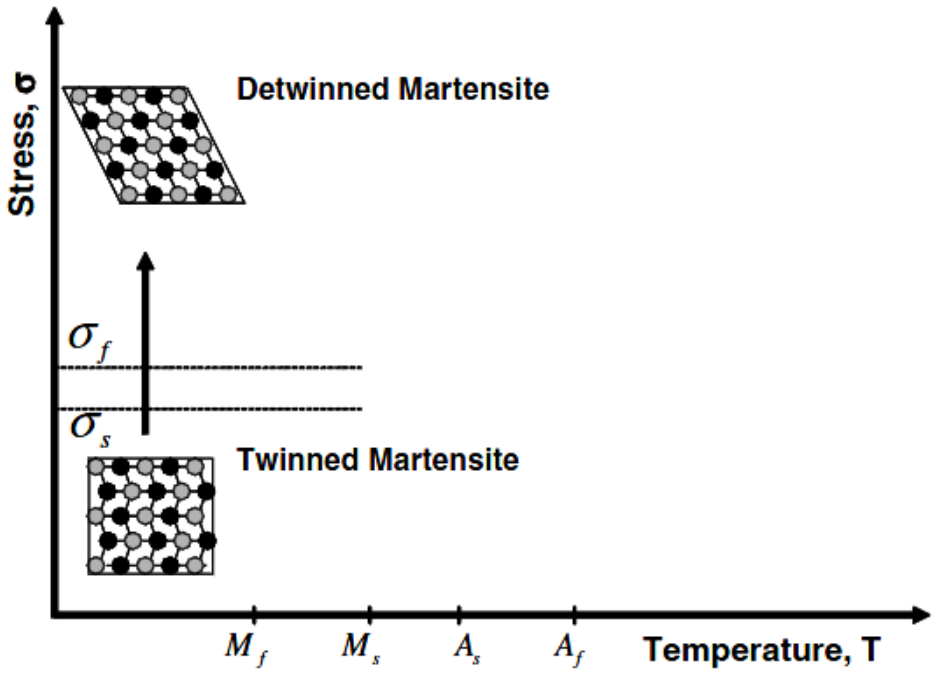

Figure 2.8 Detwinning process of TiNi under an applied stress

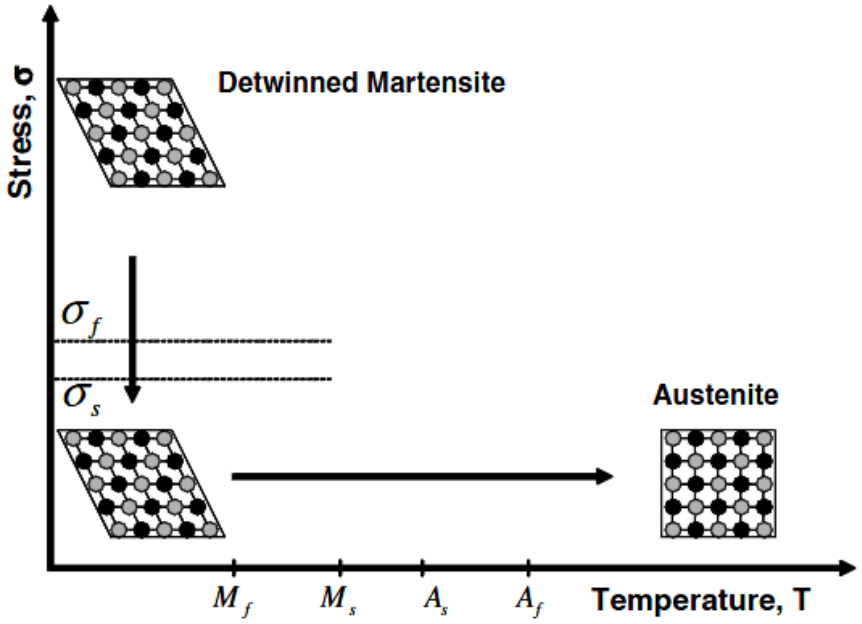

Figure 2.9 Reverse transformation upon heating of TiNi

2.4 Mechanical Behavior of TiNi

Shape memory and superelasticity are unique characteristic of TiNi shape memory alloy which occur due to reversible martensite transformation. These characteristics are discussed below.

2.4.1 Shape Memory Effect

The shape memory effect was discovered by Buehler and coworkers in an equiatomic TiNi alloy, i.e. 50et%TiNi, in early 1960s (Kumar & Lagoudas, 2008). Shape memory effect is the ability of a material to recover macroscopic strain and return to its original shape upon heating. Upon cooling the TiNi from the parent austenite phase (point A in Figure 2.10) in the absence of external stress, it transforms to twinned martensite (point B). When the twinned martensite is subjected to a mechanical load, the martensite varients reorient and transform into detwinned martensite (point C). The minimum stress required to initiate the detwinning process is the detwinning start stress (σ_s) and the reorientation process ends at the detwinning finish stress (σ_f). The detwinned structure remains after unloading from point C to D. Upon heating in the absence of load, the reverse transformation initiates as the temperature reaches A_s (point E) and ends at A_f (point F). The detwinned martensite transforms back to austenite phase (point A) with a large strain recovery, i.e. the original shape is regained.

Furthermore, when cooling the austenite phase (point A), in the presence of external load above detwinning start stress, it transforms to detwinned martensite (Point C) directly. Upon heating above A_f, the reverse transformation i.e. detwinned martensite to austenite, occurs with full strain recovery.

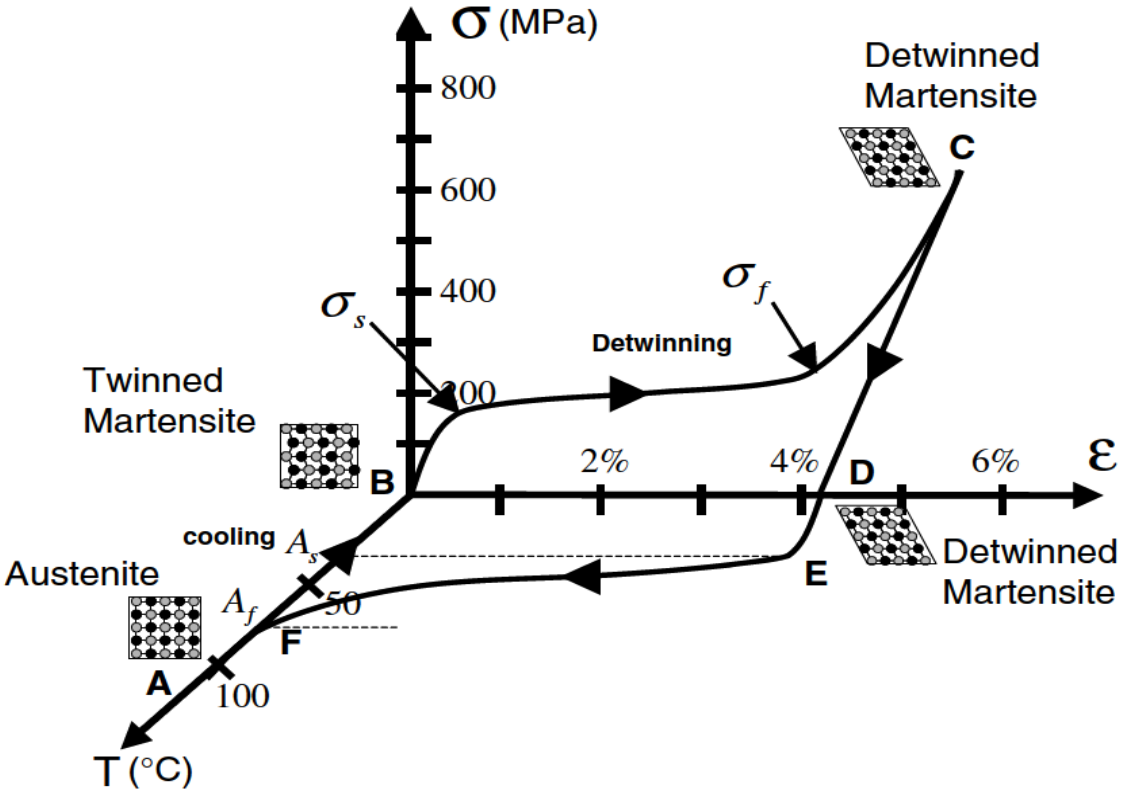

Figure 2.10 Schematic diagram representing stress-strain-temperature data exhibiting the shape memory effect (Kumar & Lagoudas, 2008)

2.4.2 Superelastic Effect

The superelastic or pseudoelastic behavior is defined as the ability of a material to recover large strain upon unloading. The superelastic behavior of TiNi is associated with the stress induced martensitic transformation. During loading, the austenite phase transforms to detwinned martensite accompanied by large deformation. The reverse transformation from martensite to austenite occurs upon unloading, accompanied by large recoverable strain. The stress levels at which the martesnite transformation starts and ends are named σ^{Ms} and σ^{Mf}, respectively. Similarly, the stress levels at which the reverse transformation starts and ends are termed σ^{As} and σ^{Af}, respectively. Furthermore, upon unloading full strain recovery occurs if the temperature is above A_f and partial strain recovey occurs if the temperature is between M_s and A_f. A schematic of a loading path demonstrating superelastic behavior of TiNi is shown in Figure 2.11.

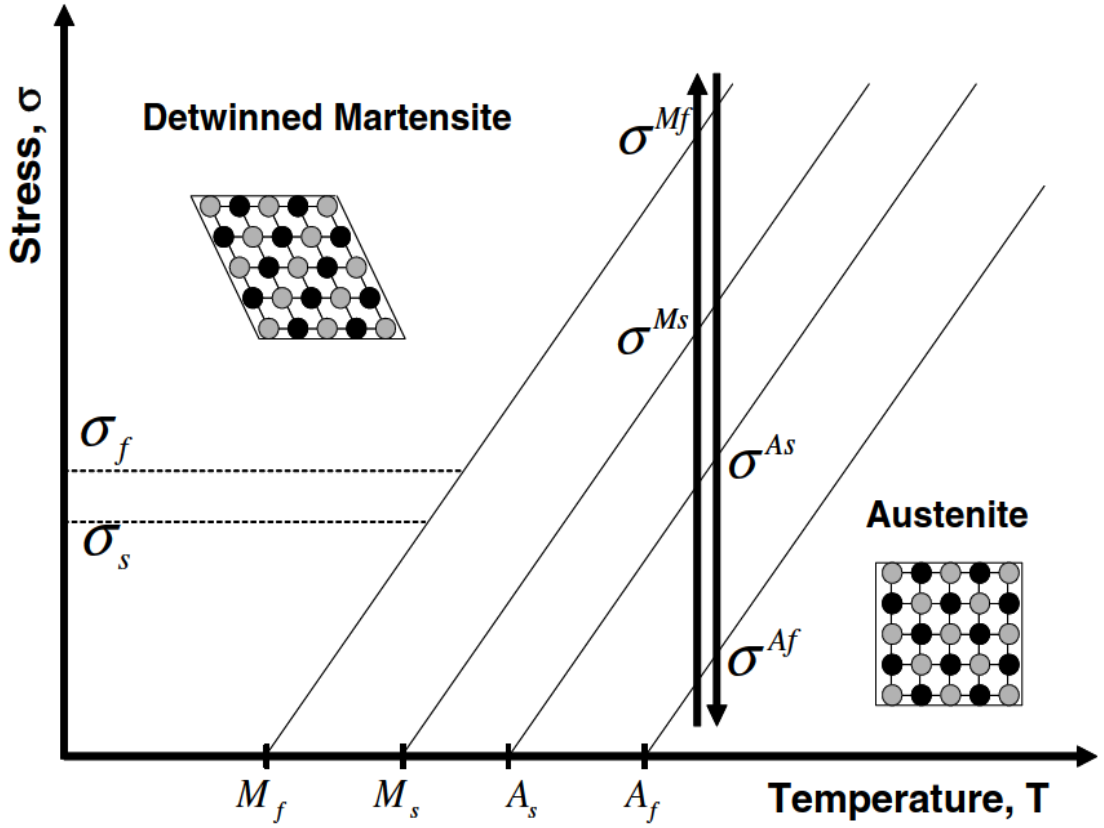

Figure 2.11 Schematic diagram representing superelastic effect in TiNi (Kumar & Lagoudas, 2008)

2.4.3 Stress-Strain Curve of Superelastic TiNi Alloy

A stress-strain curve for superelastic TiNi alloy is illustrated in Figure 2.12. The stress-strain curve represents a typical deformation behavior of superelastic alloys. The first initial rise in stress-strain curve of superelastic TiNi is due to elastic deformation of austenite (A to B). This is followed by a stress plateau, a large recoverable deformation and phase transition from austenite to martensite as a result of stress-induced martensitic transformation (B to C). At the end of the plateau region, the material enters into an eleastic/plastic deformation mode and behaves like conventional metals (C to D). Upon unloading, martensite transforms back to the austenite phase and the large deformation is recovered during the process. Upon unloading, martensite to austenite phase transition (D to A) occurs with large recoverable strain. The transformation from martensite to austenite starts at σ^{As} i.e. start stress for the reverse transformation and ends at σ^{Af} i.e. finish stress for the reverse transformation. Materials exhibiting superelastic behavior

have large elongation during deformation due to suppression of necking and have high strain rate sensitivity (Dieter, 1976).

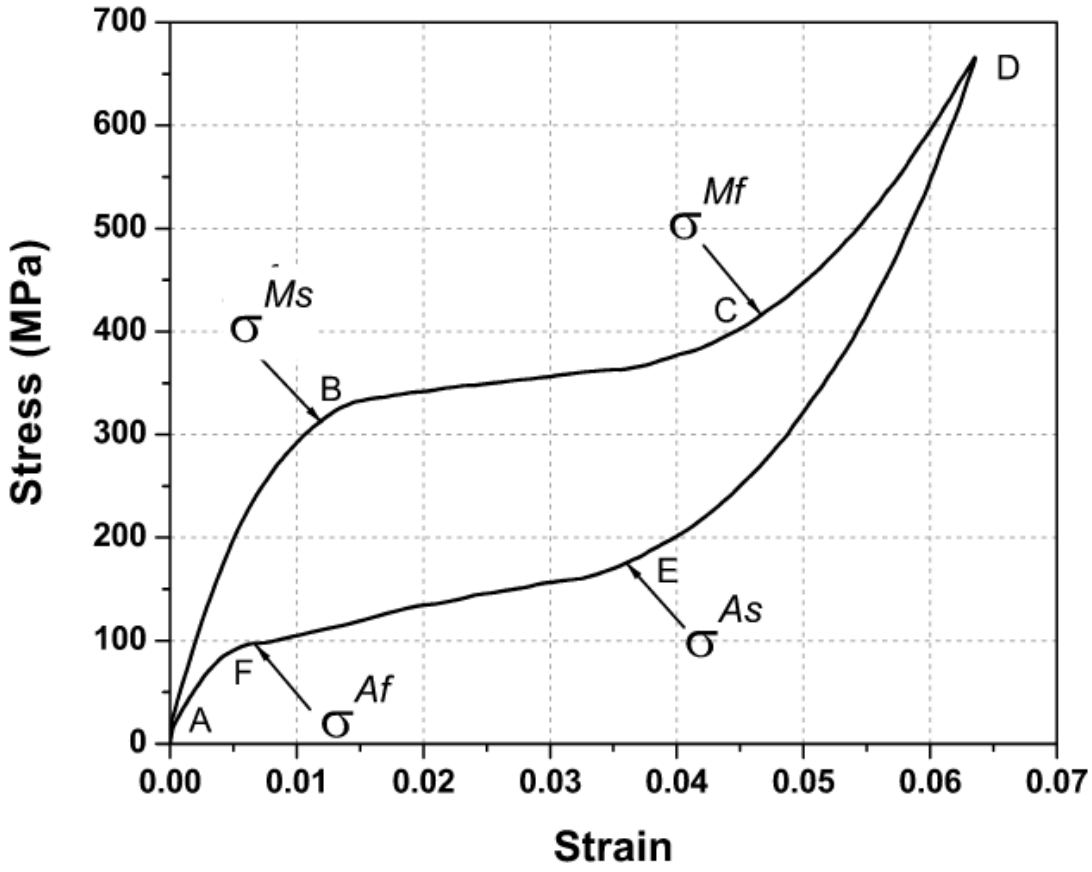

Figure 2.12 A typical stress-strain curve of superelastic TiNi alloy (Kumar & Lagoudas, 2008)

Both shape memory effect and superelastic behavior can occur in the same TiNi alloy, depending on the testing temperature. As mentioned above, shape memory and superelastic behavior occurs due to reversible martensitic transformation which could be induced thermally or mechanically. However, the martensite transformation cannot occur at a temperature above the superelastic temperature limit, M_d (Figure 2.13). Above M_d, the austenite deforms plastically by slip, as the stress required for slip is lower than that for austenite-to-martensite transformation stress. Hence, at temperatures above M_d, TiNi behaves like conventional material and no superelasticity is observed.

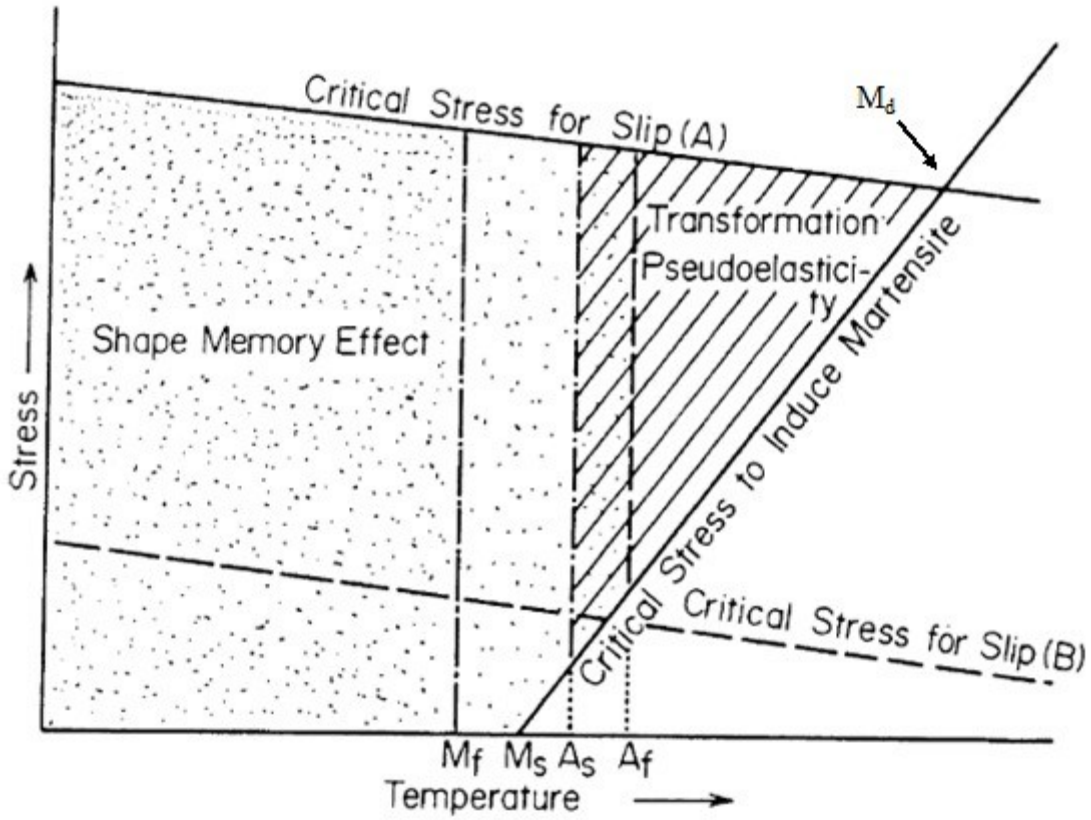

Figure 2.13 Schematic diagram showing shape memory and superelasticity regions, (A) and (B) represents high and low critical stress, respectively (Otsuka & Ren, 2005)

2.5 Indentation Behavior of Superelastic TiNi Alloy

Instrumented indentation methods have been extensively used in recent years to assess mechanical properties of materials. Hardness and elastic modulus are frequently calculated from load-depth data obtained from micro- and nano-indentation tests. Much work has been undertaken to exploit indentation techniques to study materials and coatings at small indentation scale ((Qian, Sun, & Xiao, 2006), (Yan, Sun, Feng, & Qian, 2007), (He & Sun, 2010), (Tabor, 1996), (Cheng & Cheng, 2004), (Oliver & Pharr, 1992), (Xu & Agren, 2004), (Cheng & Cheng, 2005), (Ebenstein & Pruitt, 2006)). The study of indentation behaviour of conventional materials is complex and involves elastic, elasto-plastic and plastic deformations underneath an indenter. For superelastic materials, such as TiNi, the above deformations are coupled with a reversible stress-induced martensitic transformation, which adds to the complexity of the problem. Current indentation theories and models ((Cheng & Cheng, 2004), (Nix & Gao, 1998), (Hertz, 1896), (Oliver & Pharr, 2004)) deal mainly with the deformation of single phase materials with no phase transition and fail to explain behaviour when extended to materials that undergo phase transformation during indentation. More recently, researchers attempted to extended current theories to study the mechanical properties of multi-phase functional materials ((Qian, Xiao, Sun, & Yu, 2004), (Ni, Cheng, & Grummon, 2003), (Feng, Qian, Yan, & Sun, 2008)).

The most commonly employed method in determining hardness and elastic modulus from load-displacement curves, generated from indentation experiments, was developed by Oliver and Pharr (Oliver & Pharr, 1992). This method is developed for single-phase materials and produces excellent results. However, when applied to multi-phase materials that undergo phase change during indentation, such as superelastic TiNi, it fails to produce properties that describe the material. Kang and Yan (Kang & Yan, 2010) have shown that indentation hardness of superelastic alloys cannot be used directly to measure the phase transition stress or the yield stress. Oliver and Pharr method only considers the upper 25% of the unloading curve in calculating hardness and elastic modulus, which works fine for single-phase homogeneous materials. However, in the case of superelastic TiNi, regions of martensite, austenite and transformation zones coexist and their volumes vary with load and depth. This behavior gives rise to hardness and elastic modulus depth

dependency. The dependence of mechanical properties on depth, obtained by indentation techniques for TiNi, has been reported in the open literature ((Kan, Yan, Kang, & Sun, 20013), (Zhang, Cheng, & Grummon, 2007), (Amini, Yan, & Sun, 2011)).

Hardness and elastic modulus depth dependency for single-phase homogeneous materials have been studied extensively ((Ma, Long, Pan, & Zhou, 2008), (De Guzman, Neubauer, Flinn, & Nix, 1993), (Xue, Hwang, Li, & Huang, 2002)). Nix and Gao (Nix & Gao, 1998) explained the drop in hardness with depth by strain gradient plasticity theory and the density of geometrically necessary dislocations ((Fleck & Hutchinson, 1997), (Gao, Huang, Nix, & Hutchinson, 1999), (Huang, Gao, Nix, & Hutchinson, 2000)). Nix and Gao Theory predicted that hardness is inversely proportional to the square root of indentation depth and that the dependency for most materials is only significant for depths below 500 nm. However, the depth dependency in superelastic TiNi extends to higher depths below the surface than predicted by the strain gradient plasticity theory. The dependency in superelastic TiNi is mostly due to reversible martensitic transformation and the associated changes in the effective elastic modulus of the system that takes place during loading.

Unfortunately, the load-depth behaviour of superelastic TiNi is not well understood. In order to understand the mechanical properties of superelastic TiNi generated in indentation experiments, the load-depth curve needs to be studied by taking into account phase transition. However, more work is required to develop an understanding of the behaviour of superelastic TiNi under indentation.

2.5.1 Effect of Loading Rate on Superelastic TiNi

Recent studies have shown a relationship between loading rate and superelasticity under indentation conditions. Many results show that TiNi behavior is loading rate and temperature dependent ((Amini, He, & Sun, 2011), (Farhat, Jarjoura, & Shahirnia, 2013), (Shahirnia, Farhat, & Jarjoura, 2011), (Amini & Sun, 2010)). For example, Amini et al. (Amini, He, & Sun, 2011) studied the effect of loading rate on maximum nanoindentation depth for nano-grained superelastic TiNi shape memory alloy during stress-induced phase transformation. Here, TiNi alloy (Ni-56.4% Ti-43.6%) with grain size in the range of 50-100 nm was used. They reported load versus depth curves that show high recoverable

deformation with a negligible amount of plastic deformation. They generated indentation curves of superelastic TiNi at different loading rates with spherical tip radius 5.23 μm at room temperature (Figure 2.14). According to Figure 2.14, the maximum indentation depth decreases with increasing loading rate. They attributed this behavior to the release of latent heat of phase transition, and the strong temperature dependence of transformation stress of TiNi.

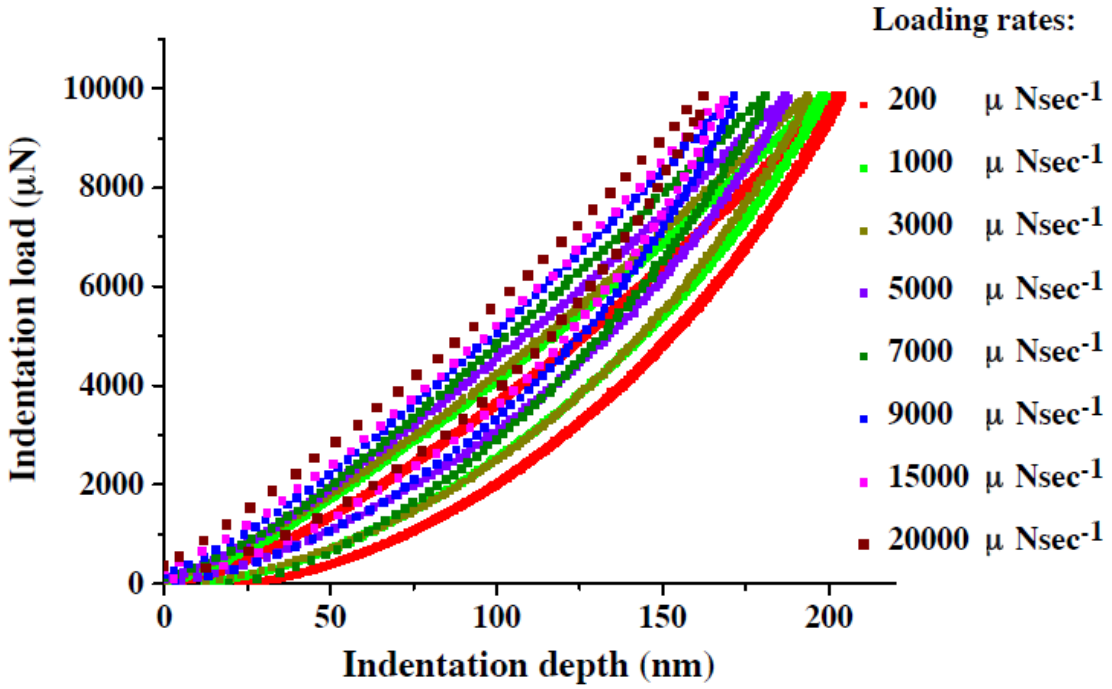

Figure 2.14 Indentation curve of superelastic TiNi at different loading rate at room temperature (Amini, He, & Sun, 2011)

Shahirnia et al. studied the effects of temperature and loading rate on the deformation characteristics of superelastic TiNi shape memory alloys under localized compressive loads (Shahirnia, Farhat, & Jarjoura, 2011). They performed the indentation tests using the loading rates of 1, 10, and 20N/min and four different temperatures, 25, 60, 100, and 150^{o} C. The load-depth curves showed full deformation recovery during unloading as a result of elastic and superelastic behavior. They showed that the maximum depth of indentation decreases with increase in the loading rate from 1 to 20 N/min i.e. at high loading rate, superelasticity diminishes and austenite to martensite transformation stress rises.

Some studies have shown that under uniaxial loading the dependency of superelasticity on loading rate is a result of the increase of austenite to martensite transition stress due to heating of the deformation zone during the deformation process ((Wang, Lei, Zhou, Wang, & Zhang, 2011), (Lin, Tobushi, Tanaka, Hattori, & Makita, 1994), (Liu, Li, & Ramesh, 2002), (Tobushi, Yoshirou, Takashi, & Kikuaki, 1998), (Dayananda & Rao, 2008)). However, a simple heat model proposed by Farhat et al. (Farhat, Jarjoura, & Shahirnia, 2013) showed that the temperature rise during indentation is insignificant and that the drop in the superelastic effect (under indentation) with increasing loading rate is not due to temperature accumulation in the transformation zone. They attributed the degradation of superelasticity as a result of increasing loading rate to the retardation of phase transformation i.e. the retardation of twin boundary mobility. However, more work is required to understand the dependency of superelasticity on loading rate of TiNi under indentation loading conditions.

2.6 Wear

Wear is defined as damage to a surface or material removal from a solid surface, due to relative motion between a surface and contacting substance. Wear is usually referred as the materials loss, but it also involves displacement of materials as a result of plastic deformation although no material removal occurred. During plastic deformation, the shape of the materials is changed due to relative motion between the two surfaces without material loss. Material loss, material displacement, changes in topology and changes in surface chemistry occur during wear (Jin & Wei, 2009). In this section, different wear mechanisms and the wear behavior of superelastic TiNi alloy are discussed.

2.6.1 Wear Mechanism

Sliding wear is a continuous unidirectional or reciprocating relative motion between two moving bodies in contact under load. Sliding wear mechanisms are identified based on the type of material removal process. Many different mechanisms of sliding wear are proposed in the literature ((Bhushan, 2002), (Jin & Wei, 2009), (Stachowiak & Batchelor, 2005), (Gohar & Homer, 2008)). However, the most commonly named mechanisms of

wear in the literature include abrasion, adhesion, fatigue wear and delamination. These sliding wear mechanisms are discussed in detail in the sections below.

2.6.1.1 Abrasive Wear

Abrasive wear is defined as damage to a surface when placed in contact with either particles or surface with greater or equal hardness (Jin & Wei, 2009). It is the most common wear mechanism, which occurs by ploughing action on a soft surface by hard material. The rate of abrasion depends on the characteristics of each surface, the presence of abrasives between the two surfaces, their relative speeds and other environmental conditions (ASM Handbook: Volume 18, 1992). Abrasive wear can be divided into two-body and three-body abrasion. Hard material sliding on a softer surface results in two-body abrasion. Three-body abrasive wear is caused by loose particles i.e. wear debris, trapped between the sliding surfaces. Three-body abrasive wear normally results in a lower material removal rate than two-body abrasive wear for a given load and sliding distance ((Stachowiak & Batchelor, 2005), (ASM Handbook: Volume 18, 1992)). Several mechanisms have been proposed to explain how material is removed from a surface during abrasion. Because of the complexity of abrasion, no one mechanism entirely accounts for all observed material loss. The abrasive wear process occurs by the combined effect of ploughing, wedge formation, microcutting, microfatigue, and microcracking ((Stachowiak & Batchelor, 2005), (ASM Handbook: Volume 18, 1992)).

The process of displacing material sideways and the formation of grooves and ridges is referred to as ploughing. Ploughing does not directly result in any real material loss as this occurs under light load. In this case, material loss can occur through microcracking of ridges as a result of repeated sliding. A wedge formation on the front of an abrasive tip results in a fairly mild form of abrasive wear. During wedge formation, the amount of material displaced from the groove is greater than the material displaced to the side.

Cutting mechanism is considered as the most severe form of wear for ductile materials (ASM Handbook: Volume 18, 1992). The cutting mechanism occurs when hard asperity or sharp grit cuts the softer surface and removes a chip, i.e. wear debris. This behavior results in a high amount of material removal and low displaced material. The degree of penetration is crucial to the transition from ploughing and wedge formation to cutting in ductile materials. Due to repeated sliding, substantial surface and subsurface plastic

deformation occurs (Stachowiak & Batchelor, 2005). This subsurface deformation leads to strain hardening which results in lower abrasive wear. Microfracture occurs when forces exerted by abrasive grains exceed the fracture toughness of the materials which is common for brittle materials such as ceramic.

Material properties such as hardness, elastic modulus, yield strength, melting temperature, crystal structure, microstructure, and composition all affect abrasive wear ((Stachowiak & Batchelor, 2005), (Gohar & Homer, 2008), (ASM Handbook: Volume 18, 1992)). The relative hardness (the ratio of the abrasive hardness H_o to the test piece hardness H) significantly influence abrasive wear characteristics as shown in Figure 2.15. Not only material properties, but environmental factors such as, the type of abrasive and its characteristics, temperature, speed, load, and humidity affect the wear rate. The hardness of the abrasive particles is important to the rate of abrasion of the subject material (ASM Handbook: Volume 18, 1992). The shape of the abrasive particles is also important, it influences the contact stress, the transition from elastic to plastic contact, and the shape of the groove produced in the material. Materials abraded by round particles results in low wear as compared to sharp particles. The increase in the toughness of abrasive particles leads to increased material loss. Abrasive wear increases with rise in temperature as a result of decrease in hardness and yield strength of the meterial. It has also been found that the rate of abrasion increases to some extent with increasing speed (range from 0 to 2.5 m/s) (ASM Handbook: Volume 18, 1992).

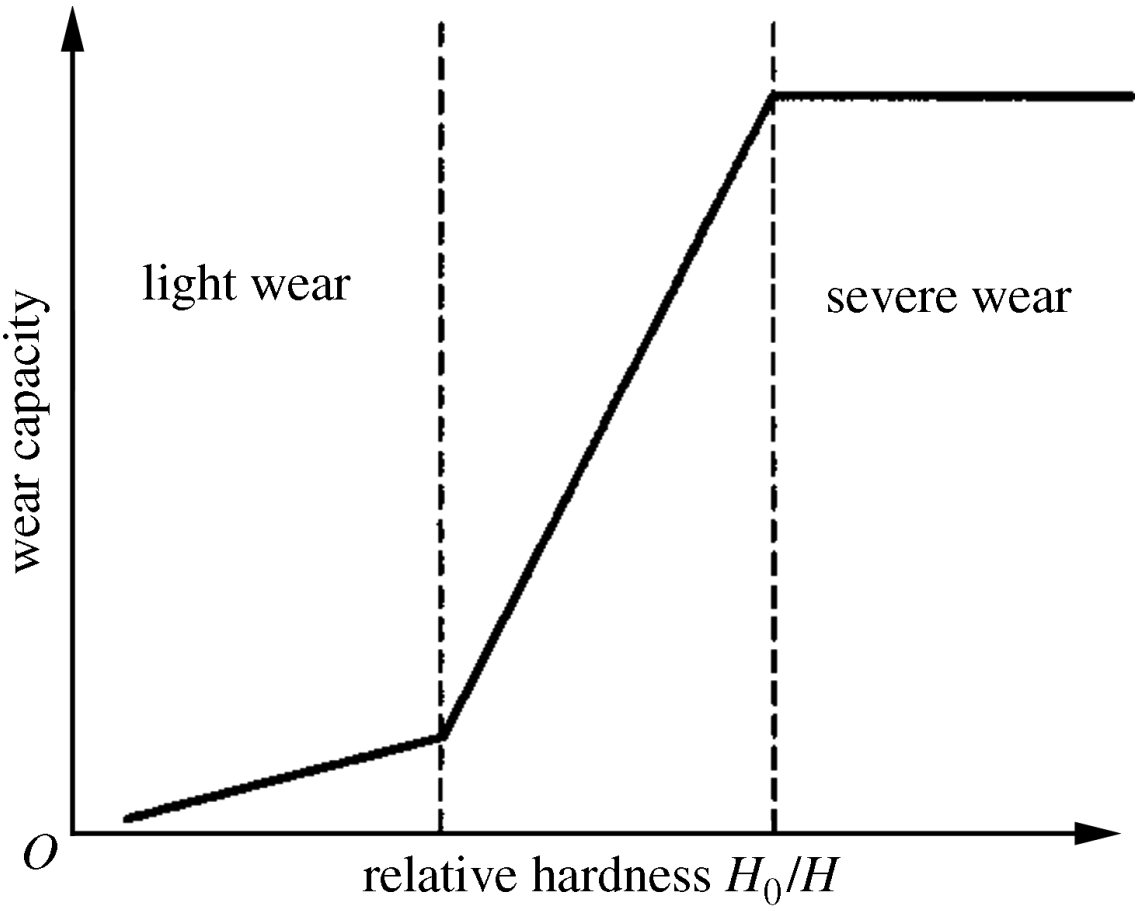

Figure 2.15 Relative hardness effect on wear (Wen & Huang, 2012)

2.6.1.2 Adhesive Wear

Adhesive wear takes place when two surfaces are placed in sliding contact under a normal load ((Jin & Wei, 2009), (Stachowiak & Batchelor, 2005), (Gohar & Homer, 2008), (ASM Handbook: Volume 18, 1992), (Bowden & Tabor, 1950)). Adhesion occurs when asperities of the two surfaces make physical contact and these contact regions form asperity junctions ((Bhushan, 2002), (Jin & Wei, 2009)). Continued sliding causes the junction to be sheared and results in the detachment of a fragment from one surface and attachment to the other surface. The number of junctions depends on surface roughness, the applied normal load and the chemical compatibility of materials in contact. In the case of significantly weak asperity junction, shearing will occur at that interface and results in zero wear. However, for high strength asperity junction, fragments may come off the soft surface and attach to the harder material, or else detach as debris. The formation of wear debris depends on the mechanical properties of the contact materials and the geometry of the asperities on the contacting surfaces.

Adhesive wear can well be described by Archard's law of wear (Archard, 1953),

$$W = KF_N/H \qquad \text{Equation 2.1}$$

where, W is the volume worn per unit sliding distance, F_N is the applied load, H is the hardness of the softer material in contact and K is the wear coefficient. Moreover, Bowden and Tabor ((Bowden & Tabor, 1950), (Bowden & Tabor, 1964) suggested that the adhesion component of friction is due to the formation and rupture of interfacial bonds. These bonds are the result of interfacial interatomic forces developing between two surfaces in contact. If sliding is to take place, a friction force is needed to shear the weakest tangential planes at the area of contact.

If the shear strength at the interface is τ_i, which is assumed to be the bulk shear strength of the weaker material, the force required to break a junction between two asperities in contact will be given by $\tau_i A_r$, that is F_T. Using the relationship, $A_r=F_N/H$, the adhesion component of friction (μ_a) becomes,

$$\mu_a = \frac{F_T}{F_N} = \frac{\tau_i}{H} \qquad \text{Equation 2.2}$$

where, H is the hardness of the softer material.

2.6.1.3 Fatigue Wear

Fatigue wear is observed when a material undergoes cyclic loading i.e. sliding, rolling and impact wear processes. In this mechanism, shear forces during the sliding process causes strain near the surface. As plastic strain accumulates, the movement of dislocations lead to the formation of surface cracks. Under repeated loading and unloading cycles, cracks grow and propagate through the material resulting in the breakup of large fragments (wear debris) and forming large pits on the surface ((Bhushan, 2002), (Jin & Wei, 2009)). Fatigue wear can occur even if the coefficient of friction is low and lubricant is present. A schematic illustration of fatigue wear behavior is shown in Figure 2.16.

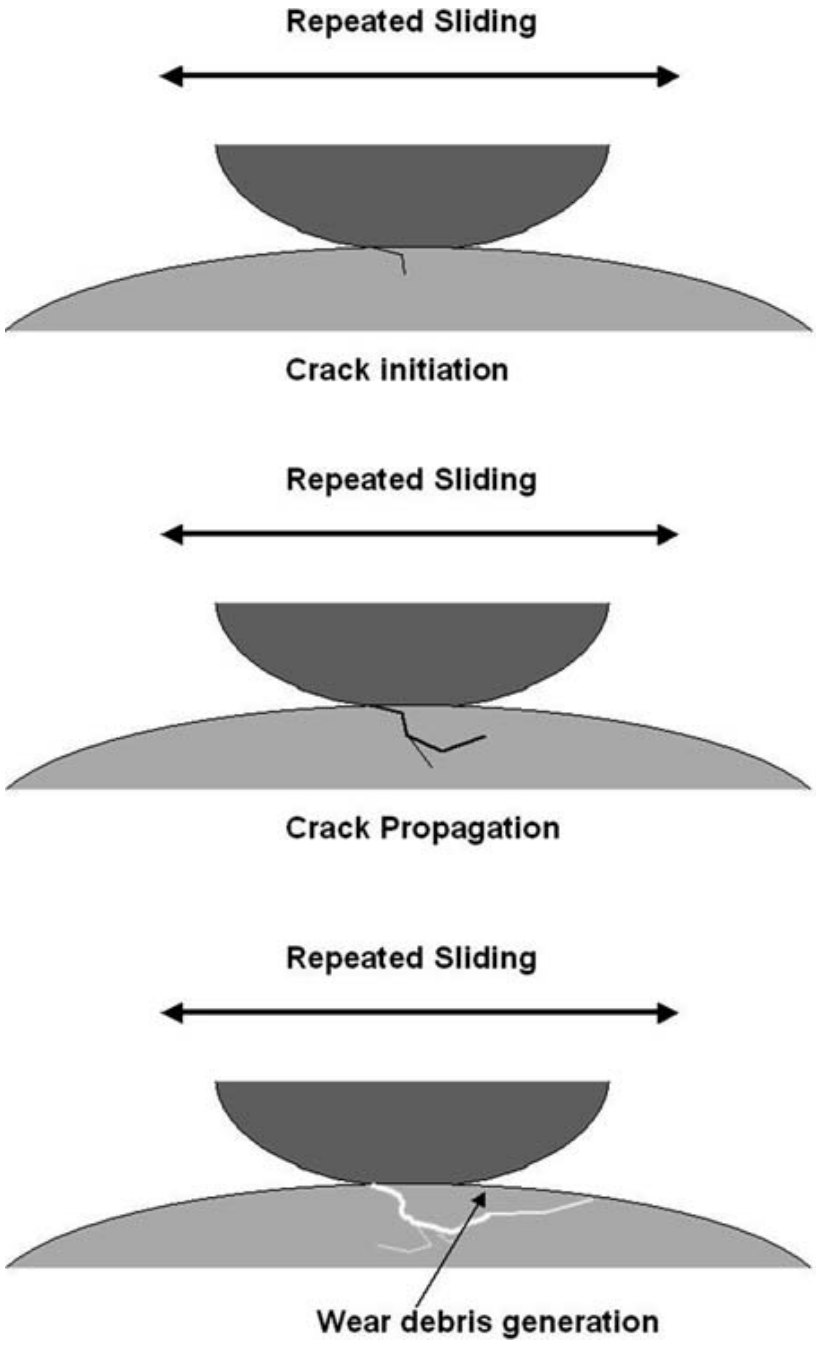

Figure 2.16 Schematic diagram of fatigue wear behavior (Jin & Wei, 2009)

2.6.1.4 Delamination Wear

Delamination occurs when two sliding surfaces come into contact, and normal and tangential loads are transmitted through the contact regions by adhesive and plowing actions ((Suh, 1977), (Hirth & Rigney, 1976), (Wen & Huang, 2012)). The asperities of the softer surface are easily deformed and fractured by repeated loading. A relatively smooth surface is generated, either when these asperities are deformed or removed. Once the surface becomes smooth, the contact is not just an asperity-to-asperity contact, but become an asperity-plane contact and each point along the softer surface experiences repeated loading. The surface traction exerted by the harder asperities on the softer surface induces plastic shear deformation which accumulates under the surface. As the subsurface deformation continues, cracks nucleate below the surface. As the cyclic loading continues, cracks propagate parallel to the surface and finally shear at certain weak positions and thin sheet-like wear particle delaminate.

2.7 Wear Behavior of Superelastic TiNi Alloy

Recent studies have shown that TiNi alloy has superior wear resistance compared to other conventional materials such as steels, Ni-based, and Co-based tribo-alloys ((Li, 1998), (Zhang & Farhat, 2009)). Wear resistance of conventional materials depend on their mechanical properties like strength, hardness, toughness, ductility, work hardening, and crystallography texture ((Li, 1998), (Zhang & Farhat, 2009), (Li, 2000)). However, for superelastic TiNi, stress-induced martensite transformation also contributes to the wear resistance. This behavior makes the understanding of wear behavior of superelastic TiNi difficult. Superelastic TiNi alloy has high ability to accommodate large scale deformation without permanent damage (Li, 1998). In the case of conventional wear-resistance material, it does not have the ability to accommodate large scale deformation without generating permanent damage.

Liang et al. (Liang, Li, Jin, Jin, & Li, 1996) studied wear behavior of superelastic TiNi alloy during sliding wear, impact abrasion and sand-blasting erosion. They compared TiNi samples with high and low superelastic behavior obtained by varying the heat treatment. Their results showed that samples with high superelasticity had higher wear resistance than those with low superelasticity.

Furthermore, sliding wear behavior of superelastic TiNi alloy was studied by Zhang et al. (Zhang & Farhat, 2009) on superelasitc TiNi, pure Ti and Ni using pin-on-disc configuration. In their work, superelastic TiNi alloy showed about 30 and 10 times higher wear resistance than pure Ti and Ni, respectively. The dominant wear mechanisms observed for TiNi were abrasion and delamination of subsurface cracks as a result of cyclic loading ((Zhang & Farhat, 2009), (Farhat & Zhang, 2010)). Sliding wear tests on Ti-50.3 at %Ni alloy and 2Cr13 steel were performed by Li et al (Li & Liu, 1999). They found that TiNi alloy has much higher wear resistance than steel, although it has a lower hardness. The superior wear resistance of superelastic TiNi alloy was attributed to low E/H ratio, high elastic recovery ratio and large contact area (Zhang & Farhat, 2009).

Previous studies showed that superelasticity of TiNi alloy is considerably affected by test conditions during wear, i.e., wear load, sliding distance, sliding speed, temperature, etc. Lin, et al (Lin, He, Chen, Liao, & Lin, 1997) investigated the effect of various wear loads, sliding speed, and sliding distance on the wear characteristics of TiNi shape memory alloy. Two TiNi alloys ($Ti_{50}Ni_{50}$ and $Ti_{49}Ni_{51}$) were tested and compared against Cr-steel. The results showed that during sliding wear, weight loss increases with increasing load according to Archard's law (Archard, 1953). They suggested that under low loads, the interface between the martensite and parent austenite phase is fairly mobile and the strain is within the superelastic strain range. However, under high loads superelasticity is not completely functional and deformation occurs by slip. They found that, during sliding wear tests, weight loss increases with the increasing sliding distance, especially for higher sliding distance. They attributed this behavior to interaction among wear mechanisms, which accelerate the wear rate. Yan et al. (Yan, Liu, & Liu, 2013) studied the wear behavior of martensitic TiNi shape memory alloy under ball-on-disc sliding tests with varying applied loads and sliding cycles. Three surface degradation stages were identified, a near-zero wear stage (characterized by very low coefficient of friction (COF) and formation of crown-like structure on the wear tracks), a transition wear stage (characterized by increase in COF after a certain number of sliding cycles, and steady COF thereafter), and an abrasive wear stage (characterized by sudden increase in COF and debris formation within 100 sliding cycles).

Lin et al. (Lin, He, Chen, Liao, & Lin, 1997) found that weight loss decreases with increasing sliding speed which they attributed to strain rate hardening. This behavior shows that at a given load high strain rate will reduce the deformation strain due to the hardening effect and, hence, reduce wear rate. SEM examination of worn surfaces showed dense and short fatigue cracks under high sliding speed, whereas deep and long fatigue cracks under low sliding speed. These deep and long fatigue cracks increase the wear rate, hence, more weight loss.

In addition, during sliding wear of TiNi, in the parent austenite phase, the applied strain is mostly transformed to elastic strain due to the formation of stress-induced martensite transformation. This elastic strain does not promote wear damage and, upon unloading, the stress-induced martensite transforms back to the parent austenite phase. Two other important factors have been reported that contribute to the superior wear resistance of superelastic TiNi alloy ((Lin, He, Chen, Liao, & Lin, 1997), (Liu & Li, 2000)). First, the contact area between the asperity and the surface increases due to superelasticity. This phenomenon reduces the stress concentration in the contact region, and hence, reduces wear damage. Second, micro-crack nucleation and propagation can be stabilized due to superelastic behavior. In the case of conventional materials, the strain energy of crack tips is released by plastic deformation or crack propagation, whereas in superelastic TiNi strain energy is partially absorbed and stored in the stress-induced martensite variants.

3 EXPERIMENTAL METHODS

The various methods used in sample analysis and data collection are highlighted in this chapter.

3.1 Materials

Equiatomic superelastic TiNi alloy sheets with dimensions of 450 mm x 95 mm x 1 mm and an austenite finish temperature (A_f) of 15^o C were obtained from Johnson Matthey Inc. The TiNi alloy plates were flat annealed and pickled at source. The TiNi sheets were oxide free and in semi polished conditions. The superelastic TiNi plates were cut into coupons of 15 mm x 15 mm x 1 mm and mounted in Bakelite. Mounted specimens were ground using 240, 320, 400 and 600 grit SiC abrasive paper followed by polishing with 1, 0.3 and 0.05 μm aluminum oxide abrasive. The chemical compositions (weight %) of the as-received superelastic TiNi alloy is given in Table 3.1. The polished specimens were used in indentation and reciprocating wear tests.

Table 3.1 Chemical composition of superelastic TiNi (wt %)

Elements	Ni	Ti	Fe	C	O	H	Others
Wt%	55.99	43.68	0.05	< 0.05	0.0216	< 0.005	< 0.20

60NiTi aged, annealed, and solution treated blocks having dimensions of 45 mm x 45 mm x 5 mm were obtained from NASA, Glenn Research Center. The blocks of 60NiTi were cut into squares of 14 mm x 14 mm x 5 mm, mounted in Bakelite and polished as described above. The chemical composition (weight %) of the as-received 60NiTi under aged, annealed, and solution treated conditions are given in Table 3.2.

Table 3.2 Chemical composition of aged, annealed, and solution treated 60NiTi (wt %)

Elements	Ni	Ti	Fe	Al	Cu	Ca	Others
Aged 60NiTi wt%	57.22	40.07	0.009	0.017	0.017	0.012	< 0.10
Annealed 60NiTi wt%	60.23	41.79	0.007	0.019	0.014	0.009	< 0.10
Solution treated 60NiTi wt%	61.52	43.16	0.009	0.021	0.011	0.015	< 0.10

AISI 304 stainless steel plates with dimensions of 50 mm x 50 mm x 2 mm were also tested for comparison. The steel plates were cut into squares of 20 mm x 20 mm x 2 mm, mounted in Bakelite, polished as mentioned above and tested. AISI 304 stainless steel was used for comparison as it exhibits similar hardness to superelastic TiNi.

3.2 Materials Characterizations

3.2.1 Optical Microscopy

In order to investigate the microstructure, optical microscopy was performed on superelastic equiatomic TiNi, aged 60NiTi, annealed 60NiTi, and solution treated 60NiTi samples. The polished specimens were etched using a solution consisting of 10 ml HF, 25 ml HNO_3 and 150 ml H_2O. Metallographic images were captured using a Unitron Optical Microscope equipped with a Micro Metrics digital camera and images were examined using Micrometrics SE Premium image analysis software.

3.2.2 Optical Profilometer

Following reciprocating wear and indentation tests, wear tracks and indentations were scanned using a non-contact white light optical profilometer. The optical profilometer was built, assembled and programmed at the Advance Tribology Laboratory at Dalhousie University. The optical profilometer uses a high resolution Chromatic Confocal Sensor optical pen attached to STIL Initial controller (STIL, France) and two stepper motors with 3.175 μm step size (Figure 3.1). The measuring range of the optical pen is 4.0 mm

with working distance of 16.4 mm and maximum slope angle of +/- 21^{o}. Software integration for optical pen and stepper motors was performed using Visual Basic.

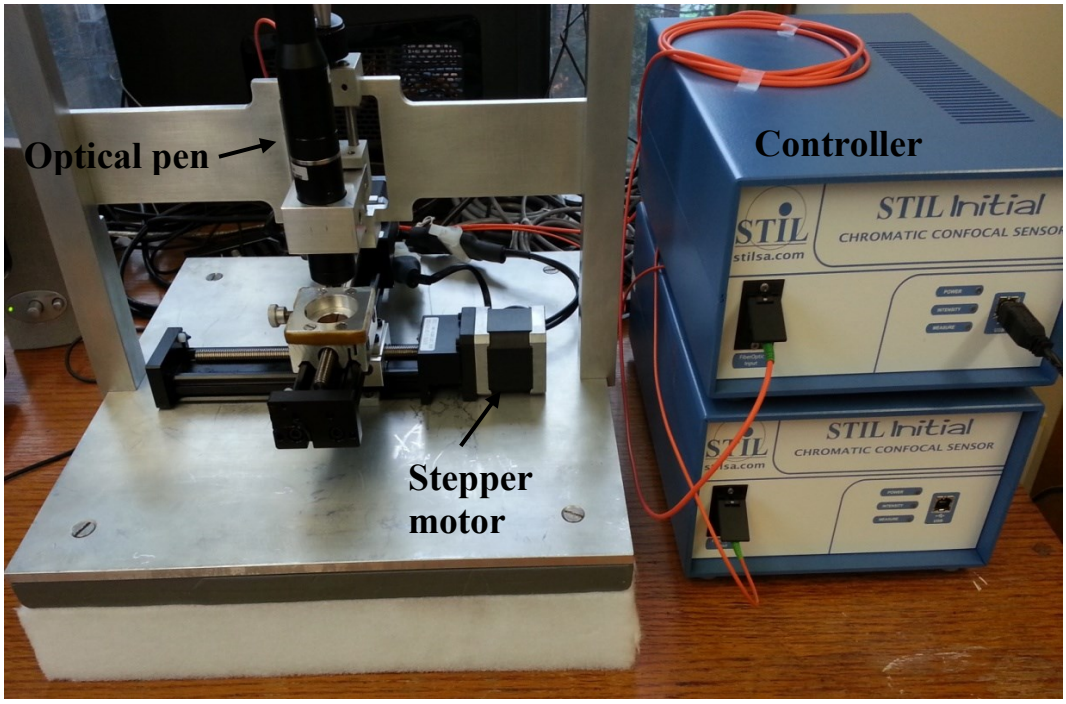

Figure 3.1 Optical profilometer

3.2.3 SEM/EDS

Hitachi S-4700 cold field Scanning electron microscopy was used to examine worn surfaces of superelastic TiNi alloy samples, wear debris collected during wear tests and indentation samples. The samples were mounted to an aluminum sample stubs and a copper tape was employed for good conductivity. Wear debris were secured by ultra smooth carbon adhesive tabs on 15 mm diameter aluminum samples stubs. The SEM was operated at an accelerating voltage of 15 kV, beam current of 10 μA, and working distance of 12 mm. An Oxford® X-Sight 7200 Energy Dispersive X-ray Spectroscopy was used for chemical analysis of wear tracks and wear debris. INCA software was used for evaluating the acquired spectra.

3.2.4 X-ray Diffraction

The X-ray diffraction tests were performed to identify phases and crystal structures of superelastic TiNi, aged 60NiTi, annealed 60NiTi, and solution treated 60NiTi samples. The XRD tests were carried out using a high speed Bruker D8 Advance XRD system as

shown in Figure 3.2. The XRD system uses a high speed LynxEye^{TM} detector and CuKα radiation with a wavelength of 1.54 Å , tube current of 40 mA and tube voltage of 40 kV. Samples were scanned from a 2θ angle of 20^{o} to 140^{o} with a step size of 0.049^{o}. Diffraction patterns were analyzed using Bruker's EVA software and compared to known diffraction patterns present in the International Center for Diffraction Data (ICDD) powder diffraction files (PDF) database.

Figure 3.2 D8 Advance XRD system

3.3 Nano and Microindentation Properties

3.3.1 Nanoindentation

Nanoindentation experiments were performed using a multi-function nano-mechanical system developed by Bruker, USA with a nanohardness head and a controller. The instrument uses a Berkovich diamond pyramid indenter with an angle of 65.3^{o} between the tip axis and the faces of the triangular pyramid. The displacement of indentation and the load are measured independently with resolutions of 0.03 nm and 0.1 μN. Hardness and elastic modulus of TiNi and 60NiTi were calculated from depth versus load curves using Oliver and Pharr method (Oliver & Pharr, 1992). The hardness is calculated according to,

$$H = \frac{P}{24.5h_c^2} \qquad \text{Equation 3.1}$$

where, h_c is the contact depth of penetration and can be calculated from,

$$h_t = h_c + \left[\frac{2(\pi-2)}{\pi}\right]\frac{P_{max}}{dP/dh} \qquad \text{Equation 3.2}$$

where, h_t is the total penetration depth, P_{max} is the maximum load and dP/dh is the slope of the unloading curve. The elastic modulus of the system is given by,

$$E^* = \frac{dP}{dh}\frac{1}{2}\frac{\sqrt{\pi}}{\sqrt{A}} \qquad \text{Equation 3.3}$$

where,

$$\frac{1}{E^*} = \frac{(1-\nu^2)}{E} + \frac{(1-\nu_i^2)}{E_i} \qquad \text{Equation 3.4}$$

where, E and ν are the elastic modulus and Poisson's ratio for the specimen and E_i and ν_i are the same parameters for the Berkovich indenter. In this study E_i and ν_i were taken as 1141 GPa and 0.07, respectively. The loading rate and maximum load combinations were varied according to Table 3.3, i.e., a total of 108 tests for equiatomic TiNi, and 189 tests for 60NiTi (aged, annealed and solution treated) were performed and each test was repeated twice.

Table 3.3 Nanoindentation test conditions

Loading rate (mN/min)	300, 600, 1800, 3000, 4200, 6000, 18000, 24000, 30000, 36000, 42000, 48000
Max load (mN)	40, 70, 100, 200, 250, 300, 350, 400, 450

3.3.2 Microindentation Tests

In order to understand the denting behavior of superelastic TiNi alloy at high load, microindentation tests were performed with various loading rates using spherical and sharp indenters. Indentation tests were conducted using a Universal Micro-Tribometer (UMT) system developed by Bruker, USA. A tungsten carbide ball indenter with a diameter of 3.18 mm and a hardness of HRA 92 was used as a spherical indenter, while a pyramidal diamond indenter was used as a sharp indenter. The indenter holder is directly attached to a 1000 N load sensor and a polished sample was secured directly underneath. The load was applied using a motor attached to a load sensor that can measure the normal load with an accuracy of 0.01 N. Depth sensing capacitive sensor with an accuracy of 0.01 μm was also attached to the system. The calibrated normal load (Fz) and indentation depth (C) were measured and continuously recorded using a data acquisition system every 0.5 seconds during the test. Each indentation test was performed twice to insure repeatability of results and the overall variation was found to be less the 10%. Indentation tests were performed on AISI 304 steel for comparison using a maximum load of 700N and various loading rates. Test conditions for superelastic TiNi and AISI 304 steel are given in Table 3.4.

Table 3.4 Microindentation test conditions using a maximum load 700N (spherical and sharp indenters)

Spherical/Sharp indenter (TiNi)	**Loading rate (N/min)**	23, 35, 38, 46, 53, 70, 87, 140, 175, 233, 350, 700, 1400, 2800
Spherical/Sharp indenter (304 steel)	**Loading rate (N/min)**	23, 46, 70, 140, 350, 1400

Furthermore, indentations were made using a spherical indenter (3.18mm diameter) and a sharp pyramidal diamond indenter under loads of 60, 100, and 150 kg (588, 980, and 1470N) using Leco R600 Rockwell hardness tester. Prior to tesing, specimens were ground and polished as above.

3.4 Tribological Characterization

3.4.1 Reciprocating Wear Test

To investigate the tribological properties of superelastic TiNi and 60NiTi, reciprocating wear tests were conducted. Dry reciprocating wear tests were performed using a Universal Micro-Tribometer (UMT) system. This test method involves a ball upper counter-face that slides against a flat lower specimen in a linear back and forth sliding motion, having stroke length of 5.03 mm. The load on the flat specimen is applied vertically downward with a motor driven carriage that uses a load sensor for feedback to maintain a constant load. The specimens were securely fastened inside the wear chamber. The setup for reciprocating wear test is shown in Figure 3.3. All tests were conducted at room temperature with relative humidity of 40-55%.

A 6.3 mm diameter tungsten carbide ball having a hardness of HRA 92 was used as a counter-face material. A WC ball was selected because it has much higher hardness than superelastic TiNi alloy. This minimizes wear of the counterface and prevents shape change, which can lead to change in the contact geometry of the tribo-system, hence, change in mean pressure during testing. The tungsten carbide ball was mounted inside a ball holder which is attached directly to a suspension system and a load sensor that controls and records forces during the test. The instantaneous values of the calibrated normal load (Fz), tangential load (Fx), and depth of wear track (Z) were measured and continuously recorded using a data acquisition system. The data automatically computes the variation of the coefficient of friction ($\mu = Fx/Fz$) with time.

Wear tests for superelastic TiNi were performed under normal loads of 20, 40, 60, 80 and 100N with varying reciprocating frequencies ranging from 5 to 20 Hz and varying time from 30 to 180 minutes. Wear tests for aged, annealed and solution treated 60NiTi were performed under normal loads of 20, 40, and 60N with varying reciprocating frequencies ranging from 5 to 20 Hz and varying time from 30 to 180 minutes. The weight of the

specimen was measured before and after each test to determine individual weight-loss at 30 minutes time intervals. The test method is based on ASTM standard G133-05(2010) (ASTM Standard G133-05(2010)), i.e. standard test method for reciprocating sliding wear. The test method simulates motion and vibration that are encountered by bearings in service (Pike & Conway-Jones, 1992). Experiments were designed to cover a range of parameters based on expected load, frequency and stroke length that bearings may be subjected to.

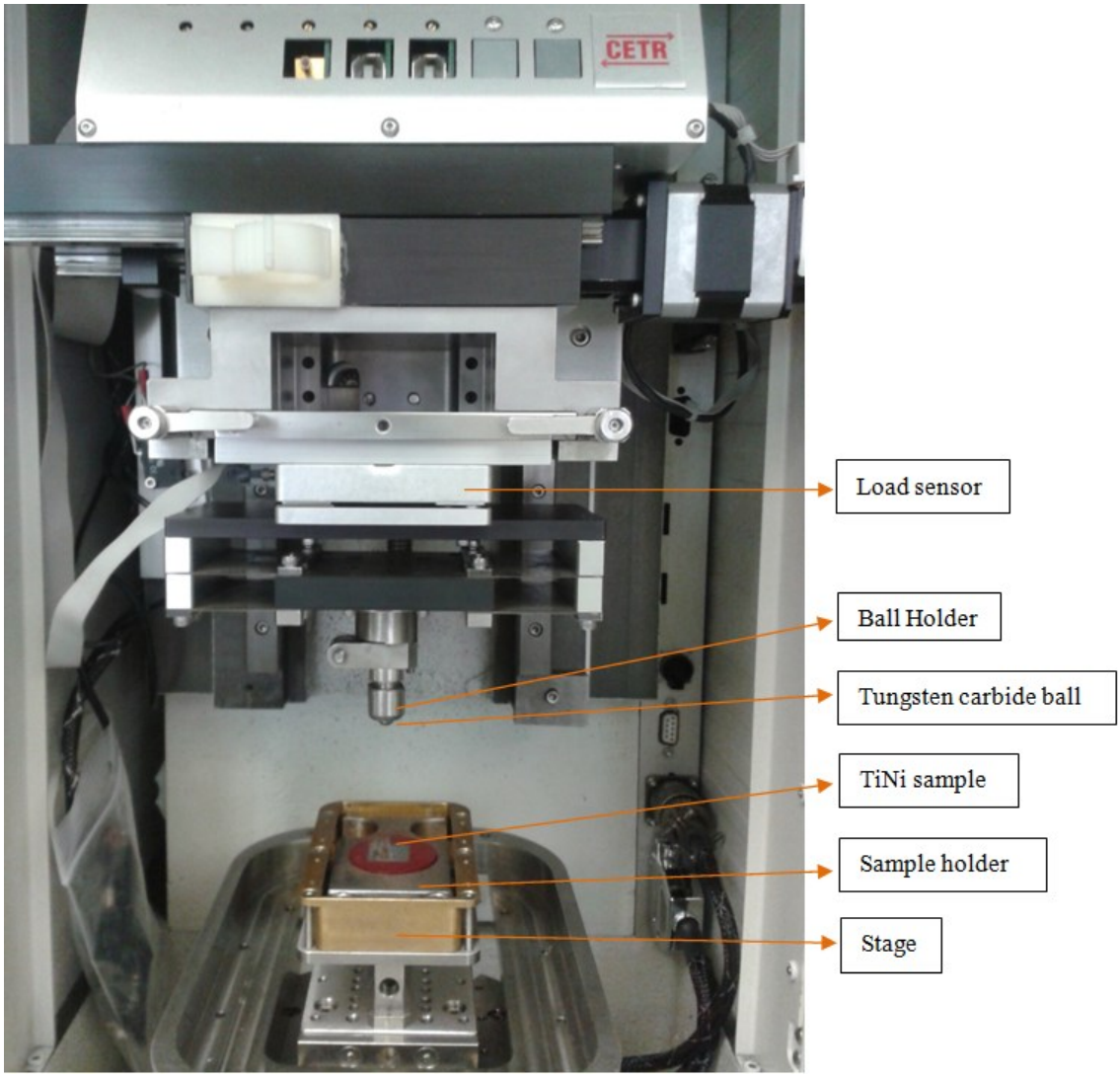

Figure 3.3 Reciprocating wear tester

4 RESULTS AND DISCUSSION

4.1 Materials Assessment

Optical micrographs of equiatomic TiNi, aged 60NiTi, annealed 60NiTi, and solution treated 60NiTi are shown in Figures 4.1-4.4. Superlastic TiNi alloy (Figure 4.1) shows grain structure consisting of regular equiaxed grains. The grain size appears to be uniform with an average size of 20 μm. On the other hand, aged, annealed, and solution treated 60NiTi show somewhat irregular and less uniform grain structure (Figures 4.2, 4.3 and 4.4). The average grain size appears to be 100 μm.

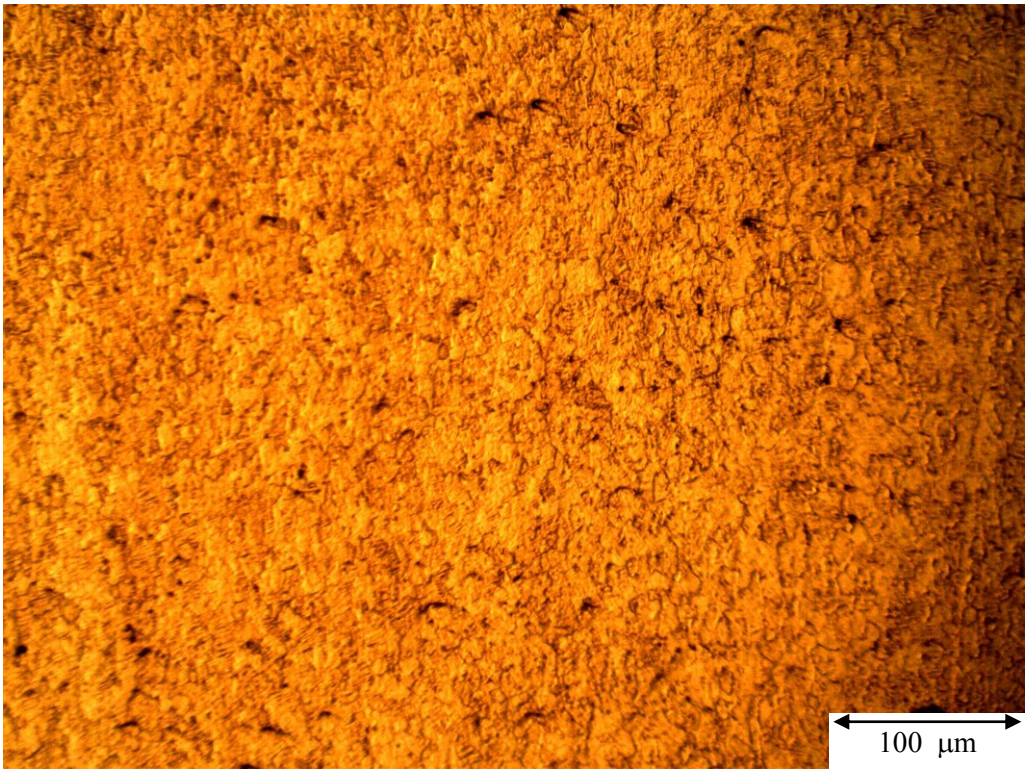

Figure 4.1 Optical micrograph of superelastic TiNi

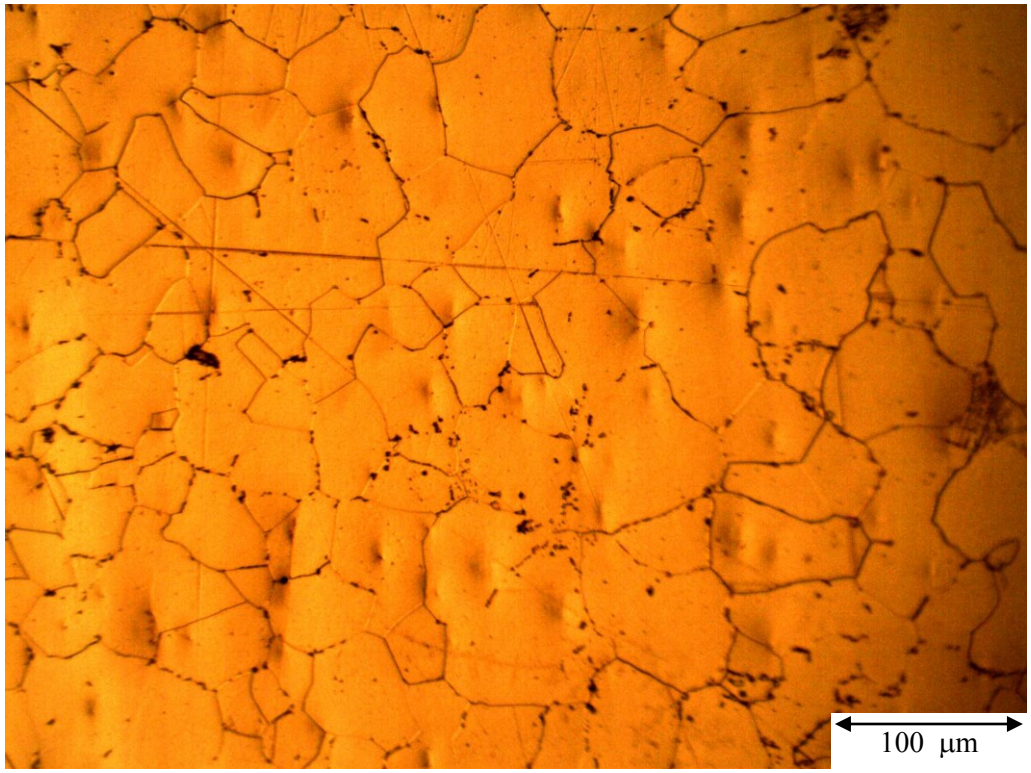

Figure 4.2 Optical micrograph of aged 60NiTi

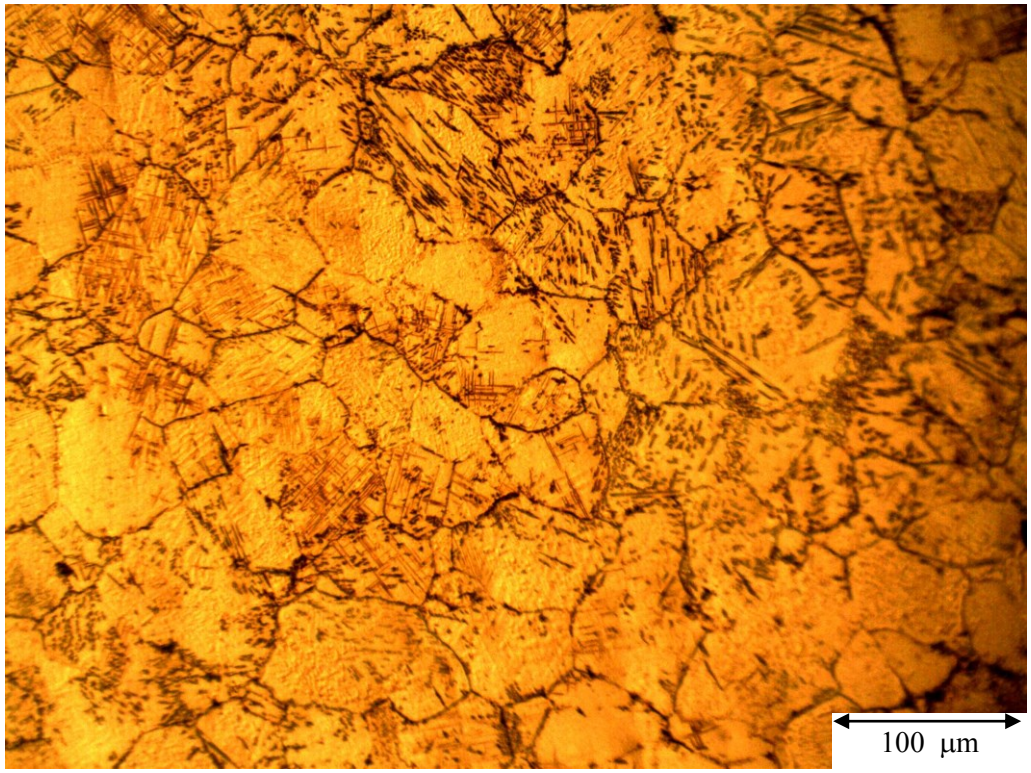

Figure 4.3 Optical micrograph of annealed 60NiTi

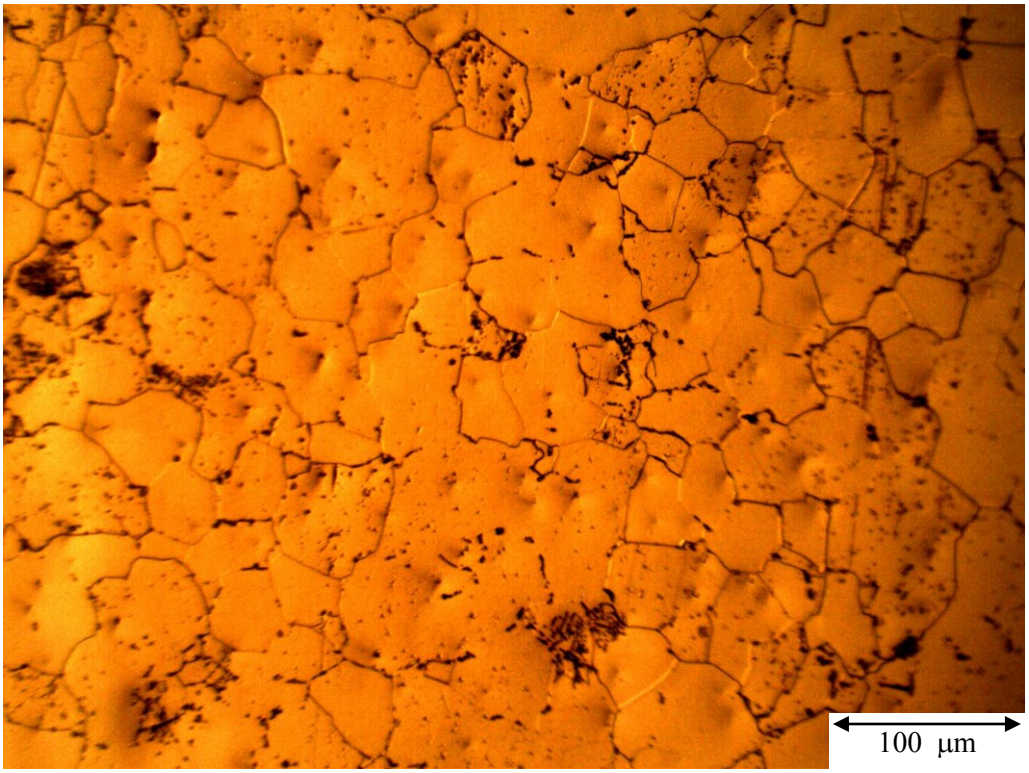

Figure 4.4 Optical micrograph of solution treated 60NiTi

60NiTi microstructure can be very complex depending on the thermal treatment (Otsuka & Ren, 2005). Depending upon aging temperature and time, metastable intermetallic phases (precipitates) such as Ti_2Ni, $TiNi_3$, Ti_2Ni_3 and Ti_3Ni_4 may form. Ti_3Ni_4 is the stable phase at lower aging temperature (680^o C) and shorter time which changes to Ti_2Ni_3 upon increasing aging temperature (750^o C) and extended time. $TiNi_3$ equilibrium phase, on the other hand, appears at higher aging temperature (800^o C) and longer aging time. Whether the precipitates are observed or not by optical metallography would depend on their size and coherency.

Crystal structure and phases of equiatomic TiNi, aged 60NiTi, annealed 60NiTi and solution treated 60NiTi were determined from x-ray diffraction patterns. The strongest peaks in all alloys are austenite peaks which indicate that all alloys are austenitic at room temperature, hence, exhibiting superelastic behavior. And the diffraction patterns reveal cubic (austenite) structure. The XRD patterns for the superelastic TiNi, aged 60NiTi, annealed 60NiTi and solution treated 60NiTi, are shown in Figures 4.5-4.8.

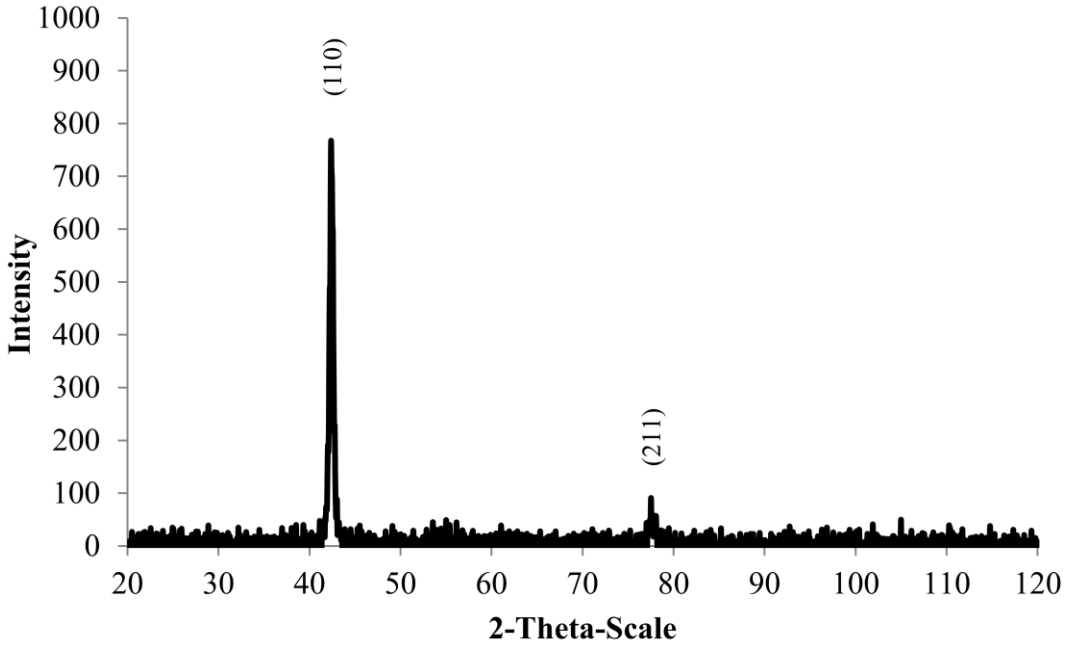

Figure 4.5 Equiatomic TiNi XRD pattern

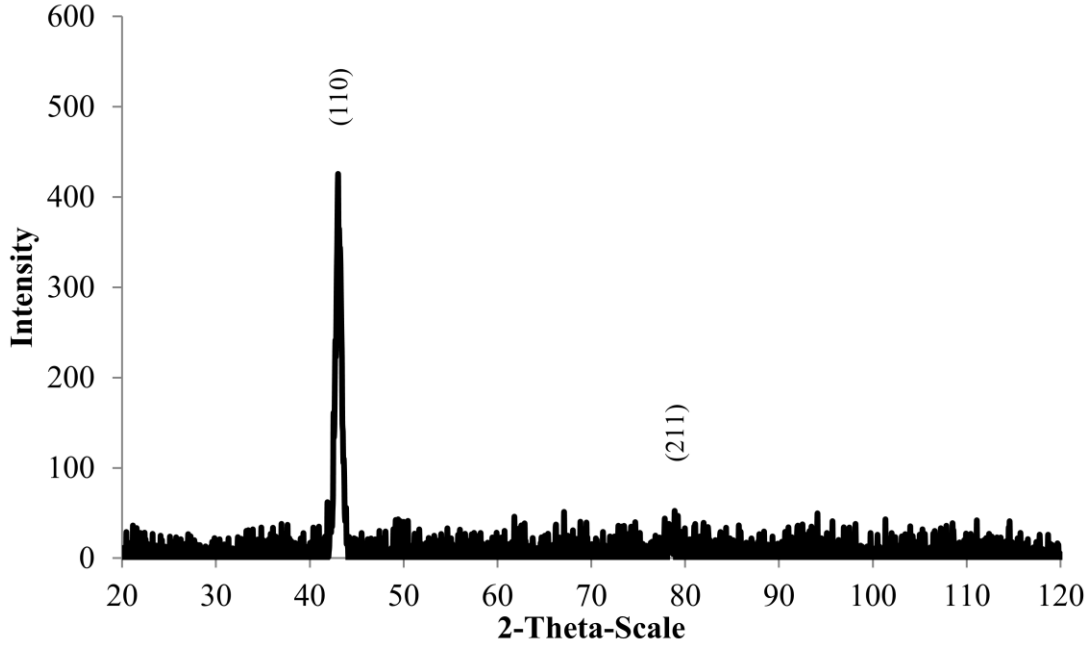

Figure 4.6 Aged 60NiTi XRD pattern

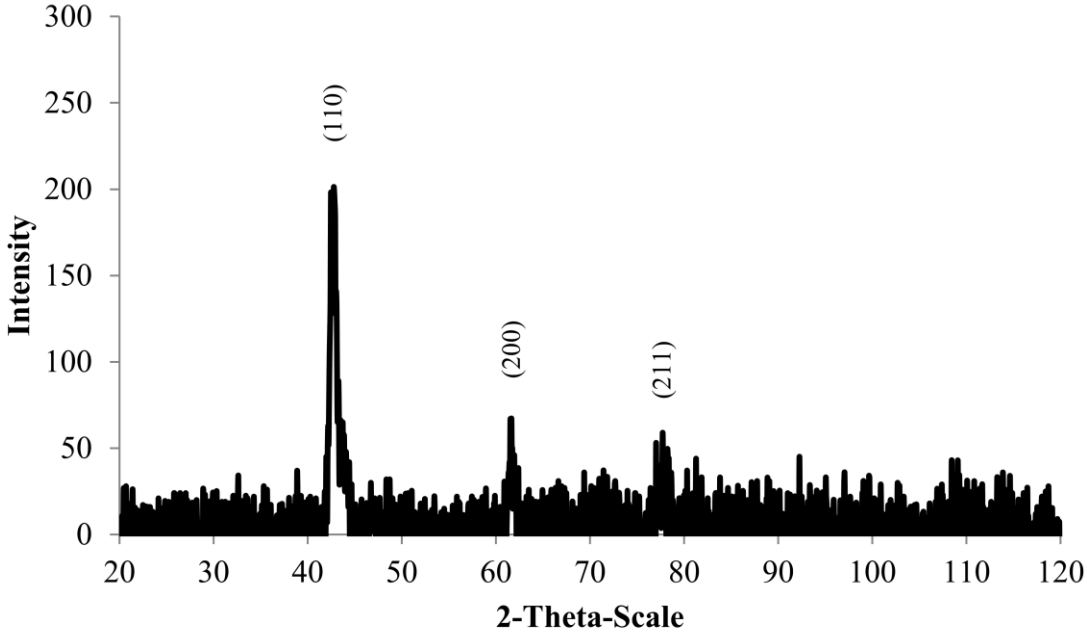

Figure 4.7 Annealed 60NiTi XRD pattern

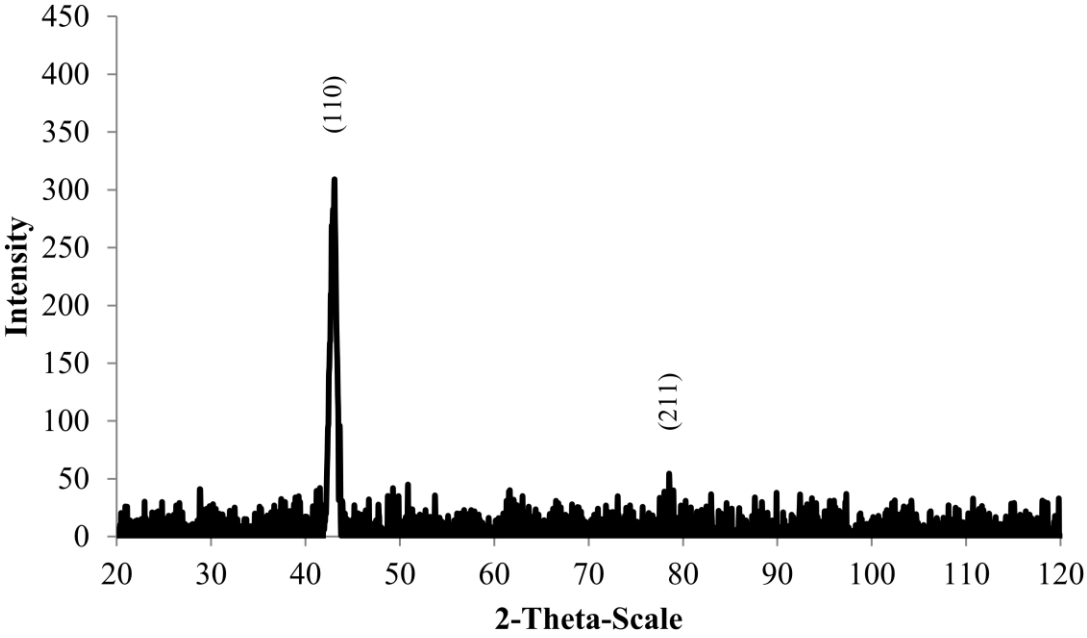

Figure 4.8 Solution treated 60NiTi XRD pattern

4.2 Indentation Tests

4.2.1 Nanoindentation Tests using Berkovich Indenter

To evaluate the effect of loading rate on the deformation characteristics of superelastic TiNi, nanoindentation tests were performed on polished surfaces employing increments of loading rates (300 to 48000mN/min) and maximum loads (40mN to 450mN). Similar experiments were perfomed on the polished surfaces of 60NiTi (aged, annealed and solution treated) under 300 to 18000mN/min loading rates and maximum loads ranging from 40 to 450mN. Each indentation test involves 12 separate indentations on different locations on the specimen surface to compensate for any variations in surface characteristics such as, surface defects, surface pores, grain orientations, grain boundaries, etc. Further, each testing condition was repeated twice on two identical samples. Indentation tests showed excellent repeatability of not more than 5% variation. Loading-unloading (load versus depth) curves were generated as a function of maximum load and loading rate at room temperature. A representative force-displacement (penetration depth of indenter) curves showing loading-unloading generated under 3000mN/min loading rate and different maximum loads using Berkovich indenter are given in Figure 4.9 (a)-(d). The curves in Figure 4.9 reveal typical load versus displacement patterns. The flat part of the curve at the max load and at the bottom part of the unloading curve are allowed to compensate for creep and thermal drift effects. All the curves generated using different maximum loads overlap as expected. The curves show high recoverable deformation and relatively small permanent deformation upon unloading. An average of over 60% recovery is observed as a result of elastic and superelastic behavior of the alloys. It is also evident that even the indentation tests performed under the lowest load of 40mN have shown residual plastic deformation which is expected for sharp indenters. The curves show the variation in hysteresis size as a function of maximum load, i.e. increases with maximum load.

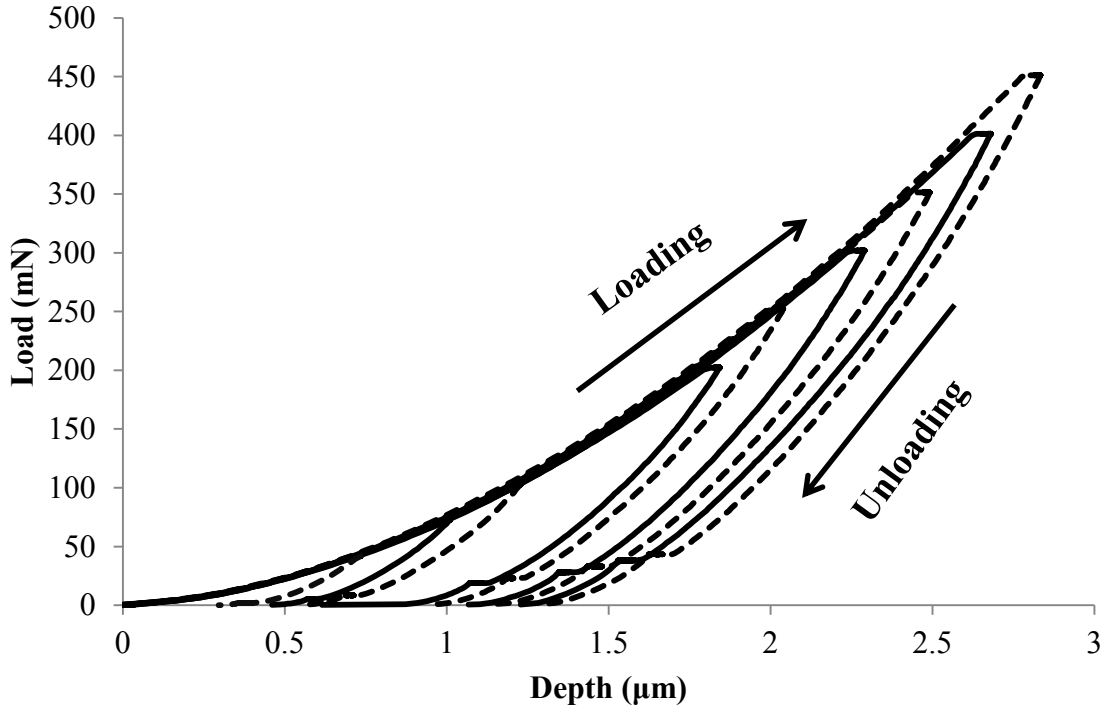
Load (mN)
Depth (µm)
Loading
Unloading
0
50
100
150
200
250
300
350
400
450
500
0
0.5
1
1.5
2
2.5
3

(a)

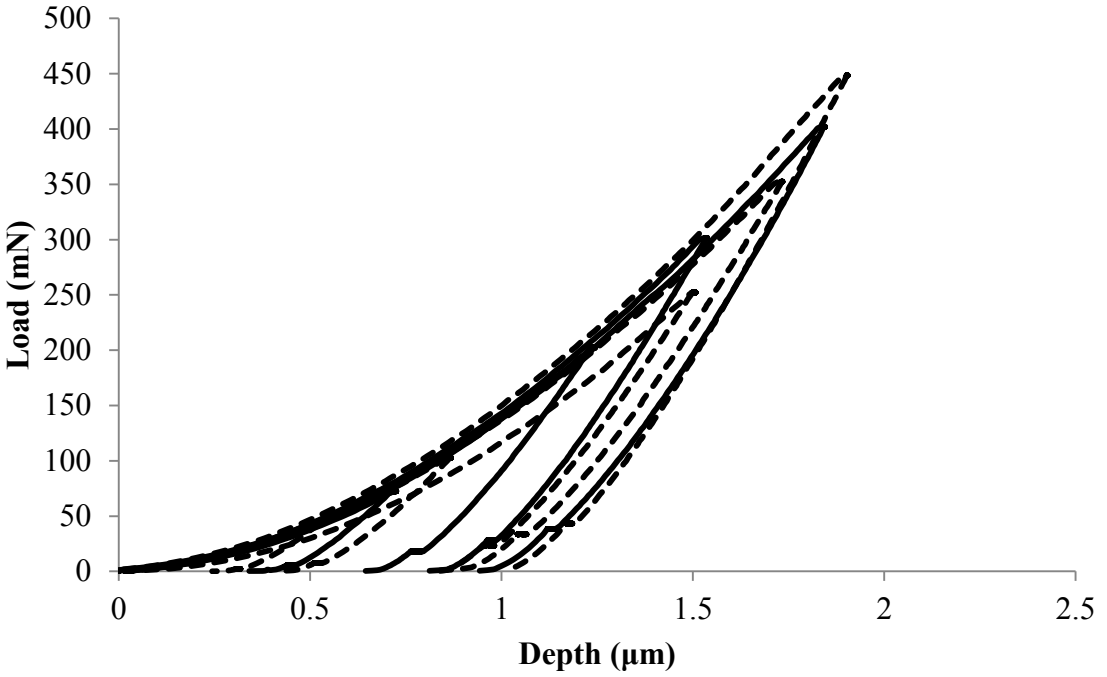
Load (mN)
Depth (µm)
0
50
100
150
200
250
300
350
400
450
500
0
0.5
1
1.5
2
2.5

(b)

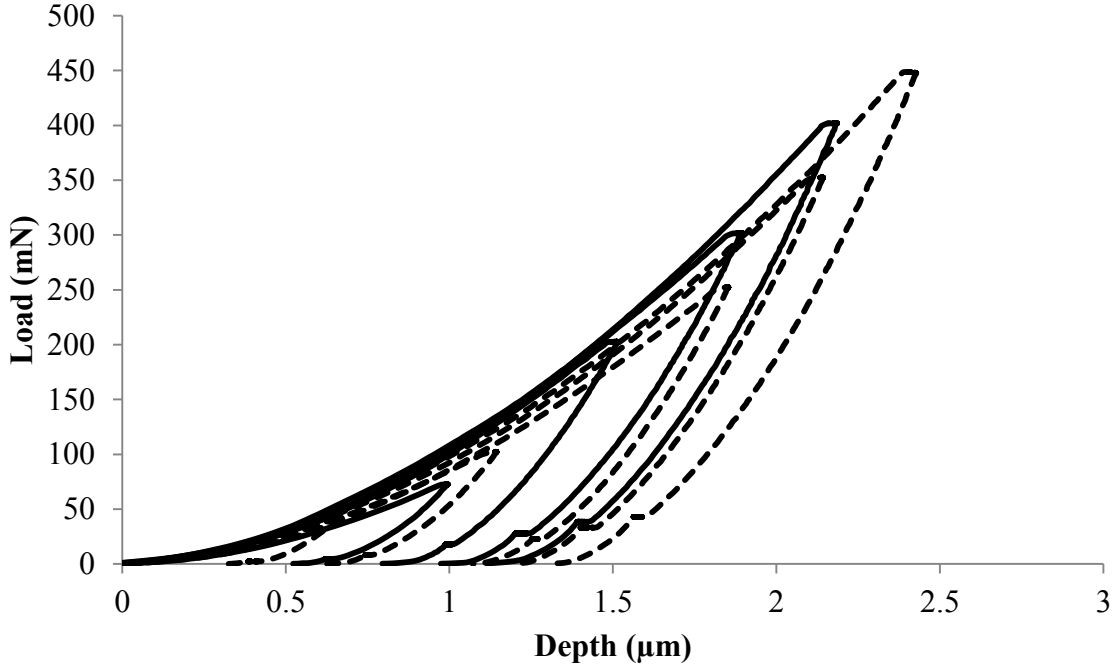

(c)

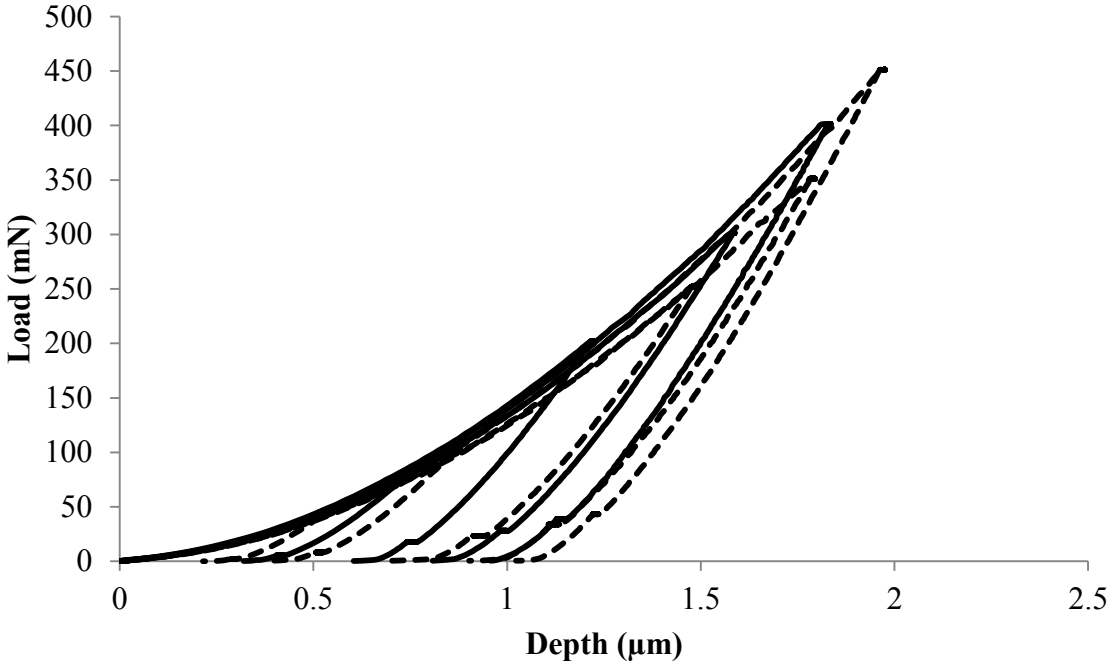

(d)

Figure 4.9 Indentation curves performed using 3000mN/min loading rate with varying maximum loads: (a) equiatomic TiNi, (b) aged 60NiTi, (c) annealed 60NiTi, (d) solution treated 60NiTi

A representative equiatomic TiNi loading and unloading cycles generated under maximum load of 300mN with loading rates ranging from 300 to 48000mN/min are shown in Figure 4.10(a). Also, representative 60NiTi (aged, annealed and solution treated) force-displacement curves generated under maximum load of 300mN with varying loading rates from 300 to 18000mN/min are shown in Figure 4.10(b)-(d). These curves allow the evaluation of loading rate dependency of superelasticity. All curves in Figure 4.10 reveal typical load-displacement patterns. The loading rate does not seem to have a significant effect on the trend and the shape of load versus depth curves except for some experimental scatter in over two orders of magnitude variation in the loading rate. Furthermore, hysteresis size is essentially unaffected to any significant extent.

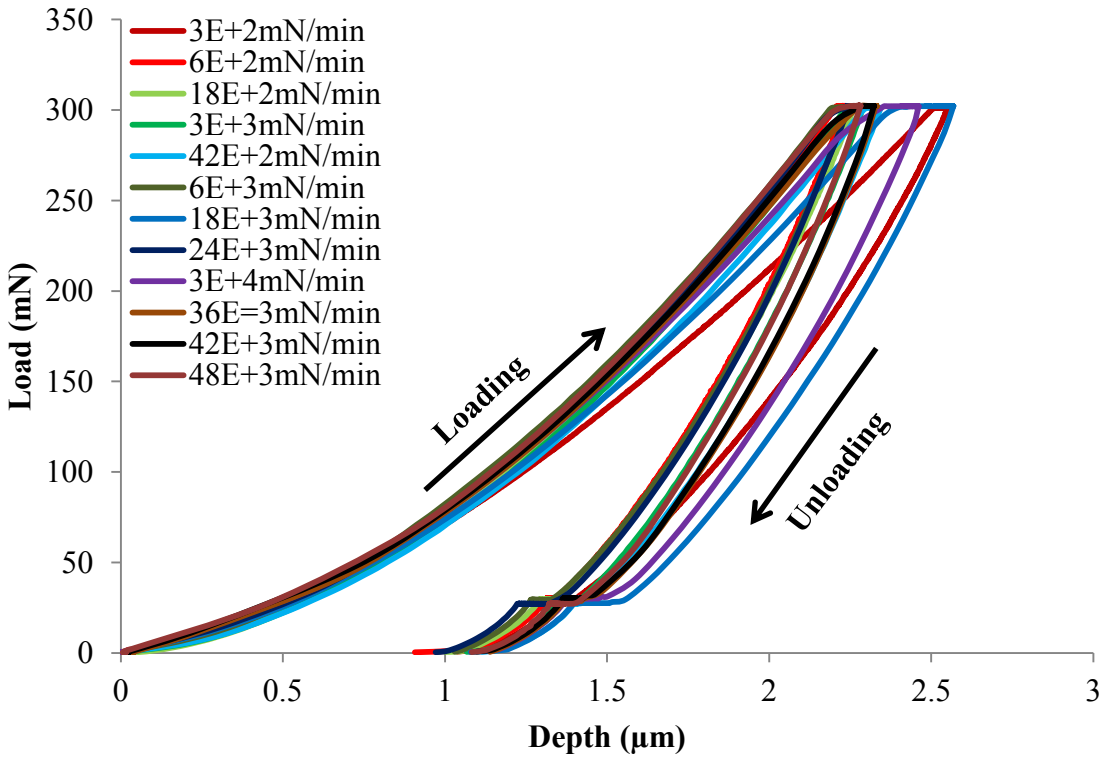

(a)

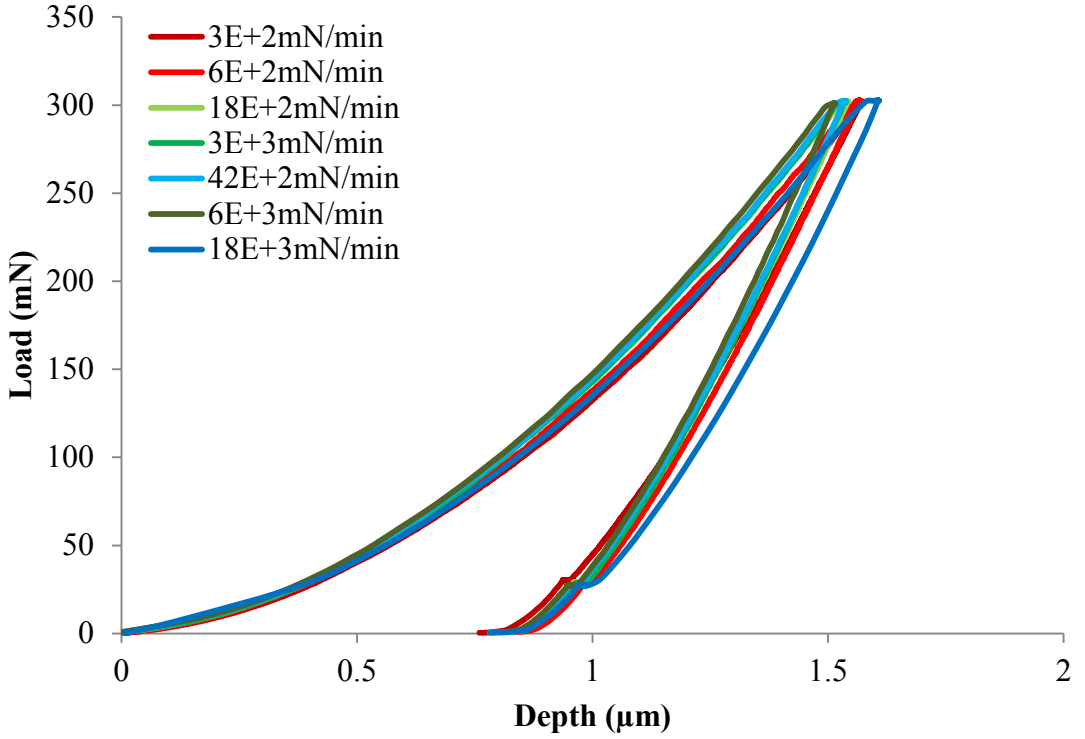
3E+2mN/min
6E+2mN/min
18E+2mN/min
3E+3mN/min
42E+2mN/min
6E+3mN/min
18E+3mN/min
Load (mN)
Depth (µm)
0
50
100
150
200
250
300
350
0
0.5
1
1.5
2

(b)

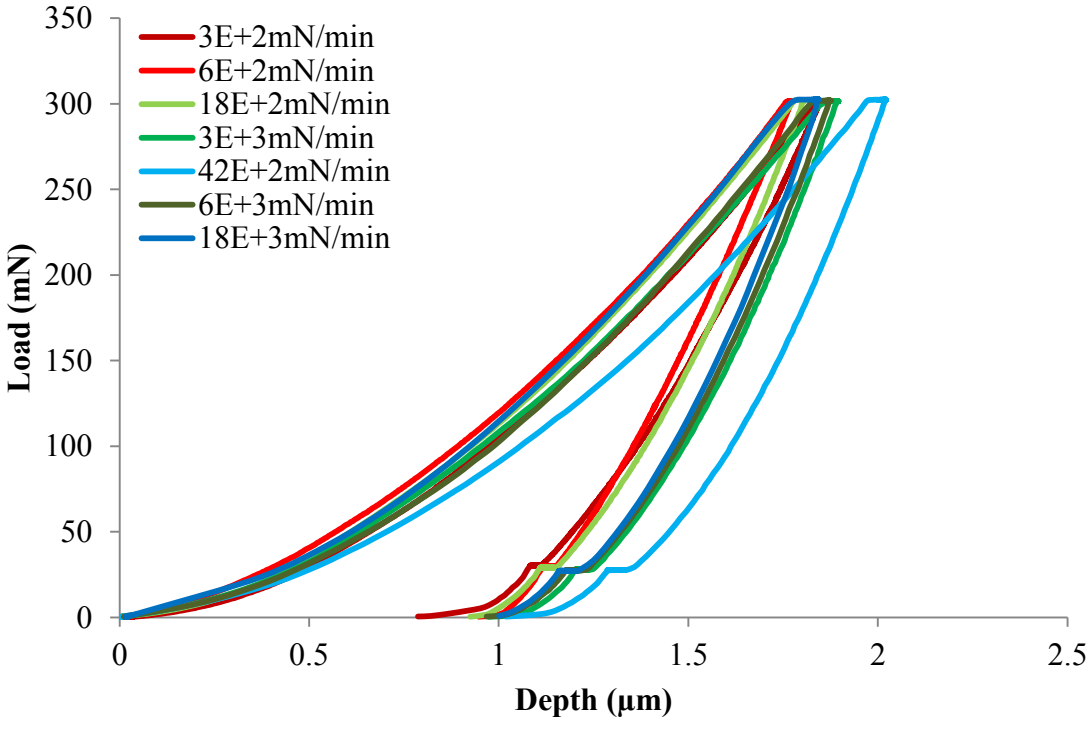
3E+2mN/min
6E+2mN/min
18E+2mN/min
3E+3mN/min
42E+2mN/min
6E+3mN/min
18E+3mN/min
Load (mN)
Depth (µm)
0
50
100
150
200
250
300
350
0
0.5
1
1.5
2
2.5

(c)

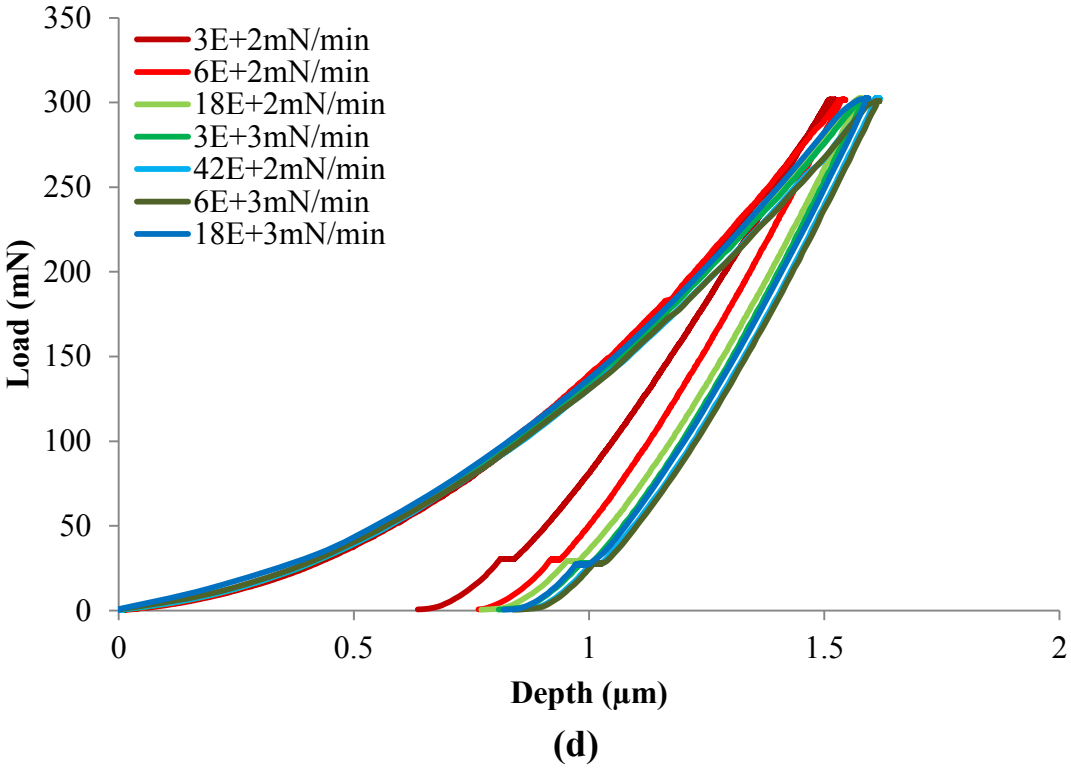

Figure 4.10 Indentation curves performed using 300mN maximum load with varying loading rates: (a) equiatomic TiNi, (b) aged 60NiTi, (c) annealed 60NiTi, (d) solution treated 60NiTi

Maximum load and maximum depth of all data were plotted (Figure 4.11) to assess the effect of loading rate on the deformation characteristics of superelastic TiNi and 60NiTi (aged, annealed and solution treated). According to Figure 4.11, the maximum depth of penetration seems to increase linearly with load for all loading rates. Data generated using different loading rates overlap with some scatter at high maximum loads. This behavior indicates that the superelastic behavior of TiNi and 60NiTi, under the indentation conditions used in the present work is independent of loading rate. To further confirm this behavior, an elastic recovery ratio was calculated for all loading-unloading curves. The elastic recovery ratio is calculated as the total area under the unloading curve over the total area under the loading curve. The average elastic recovery ratio is plotted as a function of loading rate, as shown in Figure 4.12. The recovery ratio indicates the extent of elastic recovery during deformation. The error bars indicate the scatter of the elastic recovery ratio calculated for various maximum loads at different loading rates. The elastic recovery ratio represents a better technique in assessing the effect of loading

rate on the superelastic behavior of the alloys, as this method takes the whole loading-unloading curve into consideration, as opposed to Figure 4.11 where only the maximum load and maximum depth were considered. The average elastic recovery ratio for the equiatomic superelastic TiNi obtained from nanoindentation is about 0.53. Here, elastic recovery ratio is over 7 times that of AISI 304 stainless steel (0.07) (Farhat & Zhang, 2010), although the hardness of both materials are similar. The high elastic recovery ratio of TiNi constitutes a high dent resistance compared to conventional materials. That is, the superelastic TiNi has the capacity to accommodate high denting loads without permanently deforming. The average elastic recovery ratios for 60NiTi (aged, annealed, and solution treated) are about 0.53, 0.46 and 0.53, respectively. A closer examination of Figure 4.12 revels that the elastic recovery ratios are high at low loading rates and drop to steady-state, as the loading rate increases. An approximate 10-15% drop is observed in the elastic recovery ratios. This indictes a mild drop in superelasticity as the loading rate is increased. This behavior might be attributed to retardation of the stress-induced martensitic transformation, i.e., the retardation of twin boundary mobility upon loading at high loading rates. Therefore, more plastic deformation takes place under the indenter tip, which leads to less recovery upon unloading. The slight dependency of superelasticity on loading rate (Figure 4.12) is not clearly evident from Figures 4.10 and 4.11, as the elastic recovery ratio represents a better measure of the amount of elastic recovery.

According to Figure 4.12(b) annealed 60NiTi has lower elastic recovery ratio compared to aged and solution treated 60NiTi. The lower elastic recovery of the annealed 60NiTi is attributed to its higher E/H ratio (Table 4.1) Table 4.1 summarizes the mechanical properties of equiatomic TiNi, 60NiTi (aged, annealed and solution treated) and steel. The elastic recovery ratio given in Table 4.1 is the average value calculated for all the loading rates. It is interesting to note that the average elastic recovery for the equiatomic TiNi and 60NiTi under different treatments are similar (except for annealed 60NiTi). Aged and solution treated 60NiTi exhibit a hardness values of about three times that of equiatomic TiNi, while their E/H values are lower than that of equiatomic TiNi. It can be concluded that aged and solution treated 60NiTi show enhanced superelastic behavior and superior hardness over equiatomic TiNi.

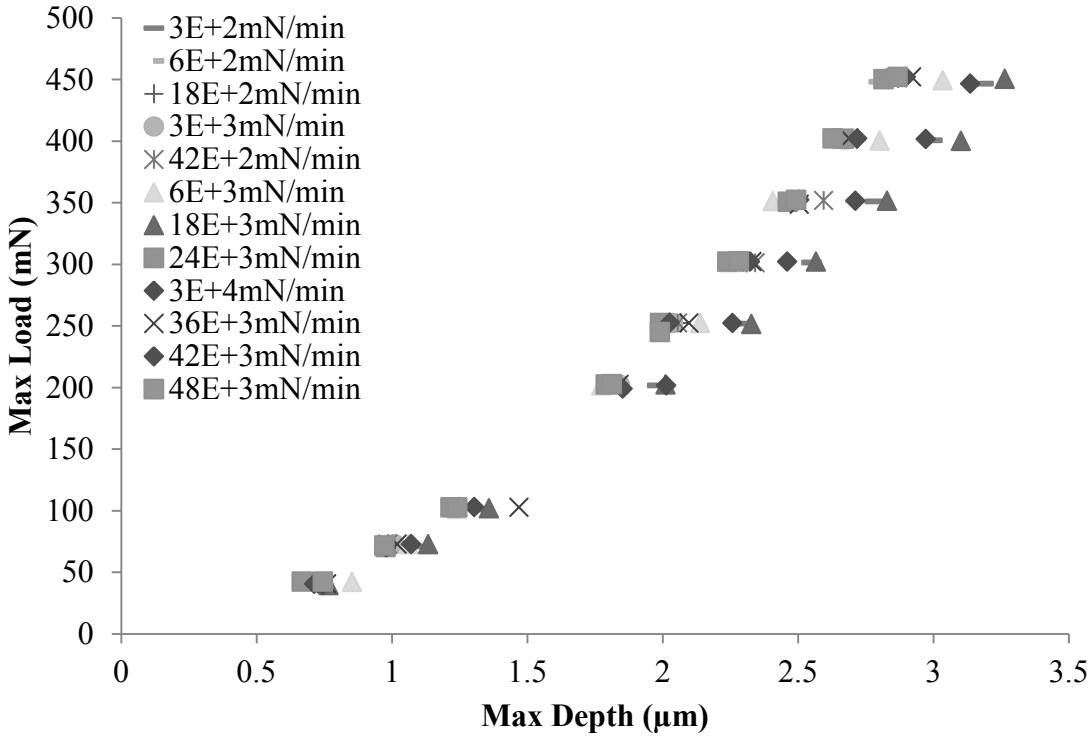
3E+2mN/min
6E+2mN/min
18E+2mN/min
3E+3mN/min
42E+2mN/min
6E+3mN/min
18E+3mN/min
24E+3mN/min
3E+4mN/min
36E+3mN/min
42E+3mN/min
48E+3mN/min
Max Load (mN)
Max Depth (µm)
0
50
100
150
200
250
300
350
400
450
500
0
0.5
1
1.5
2
2.5
3
3.5

(a)

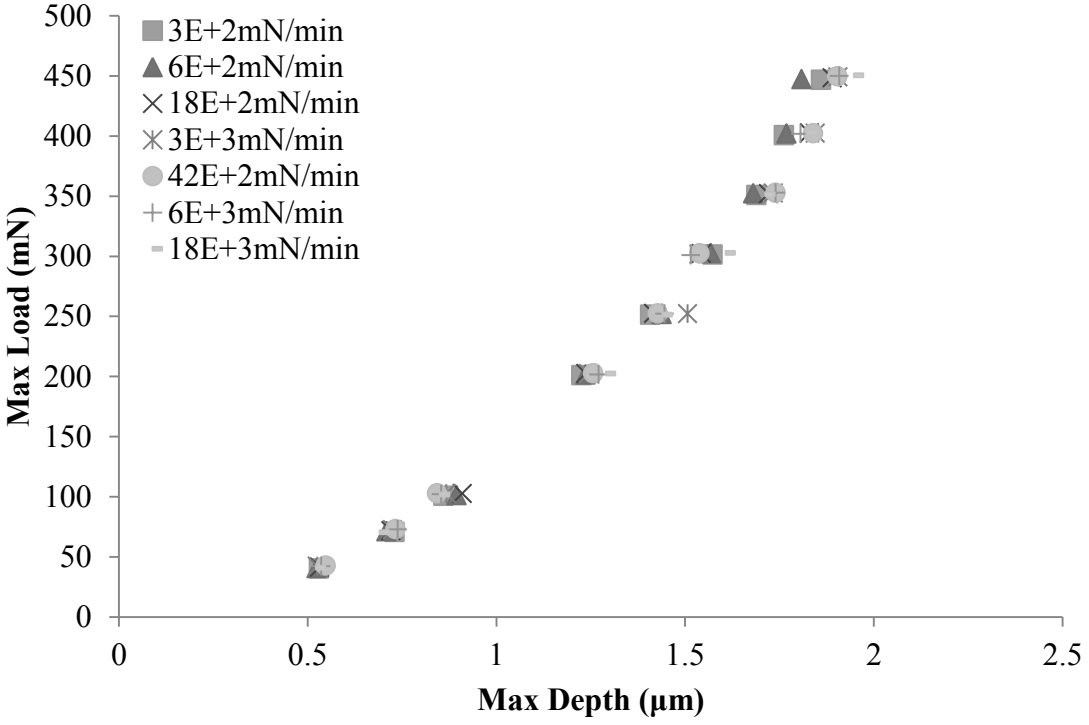
3E+2mN/min
6E+2mN/min
18E+2mN/min
3E+3mN/min
42E+2mN/min
6E+3mN/min
18E+3mN/min
Max Load (mN)
Max Depth (µm)
0
50
100
150
200
250
300
350
400
450
500
0
0.5
1
1.5
2
2.5

(b)

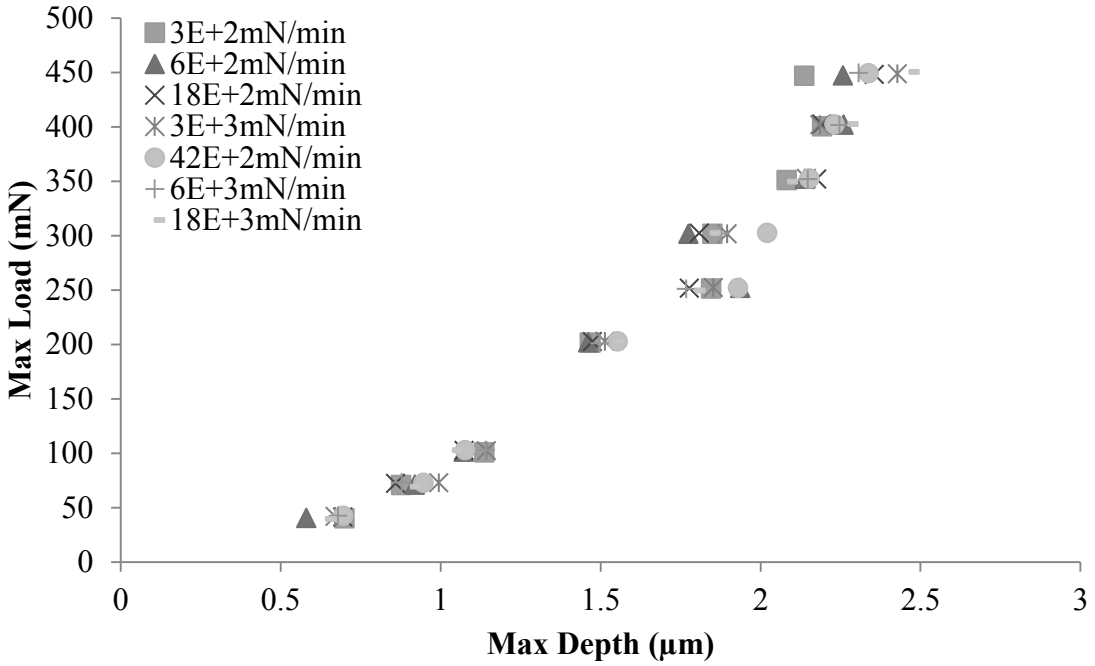

(c)

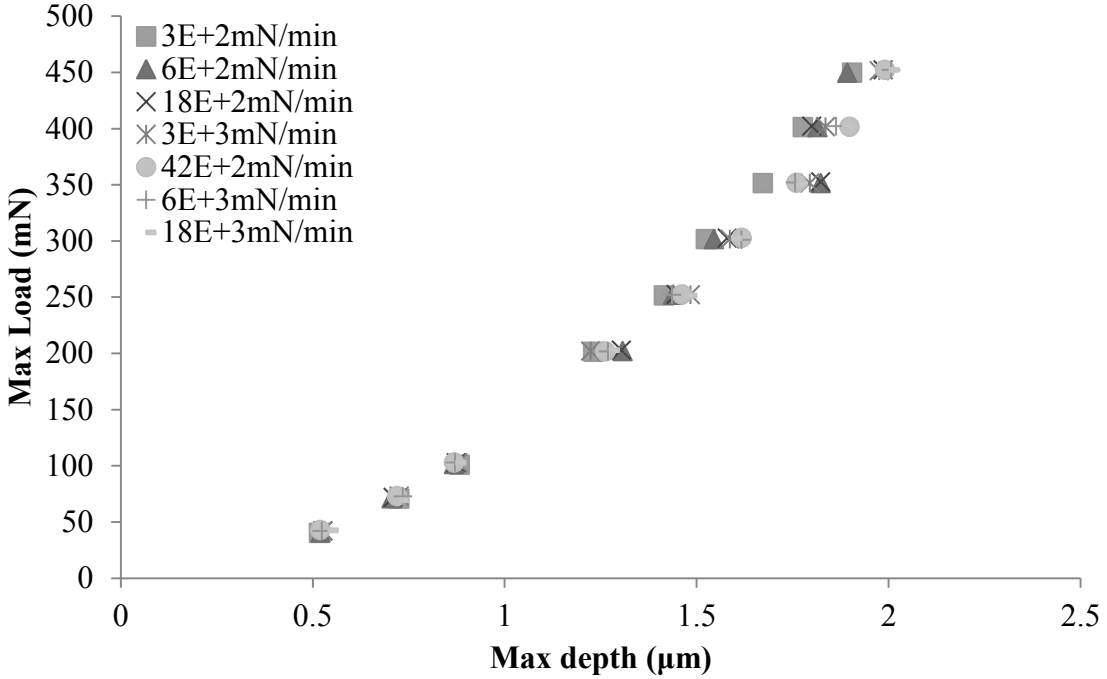

(d)

Figure 4.11 Max depth versus max load as a function of various loading rates: (a) equiatomic TiNi, (b) aged 60NiTi, (c) annealed 60NiTi, (d) solution treated 60NiTi

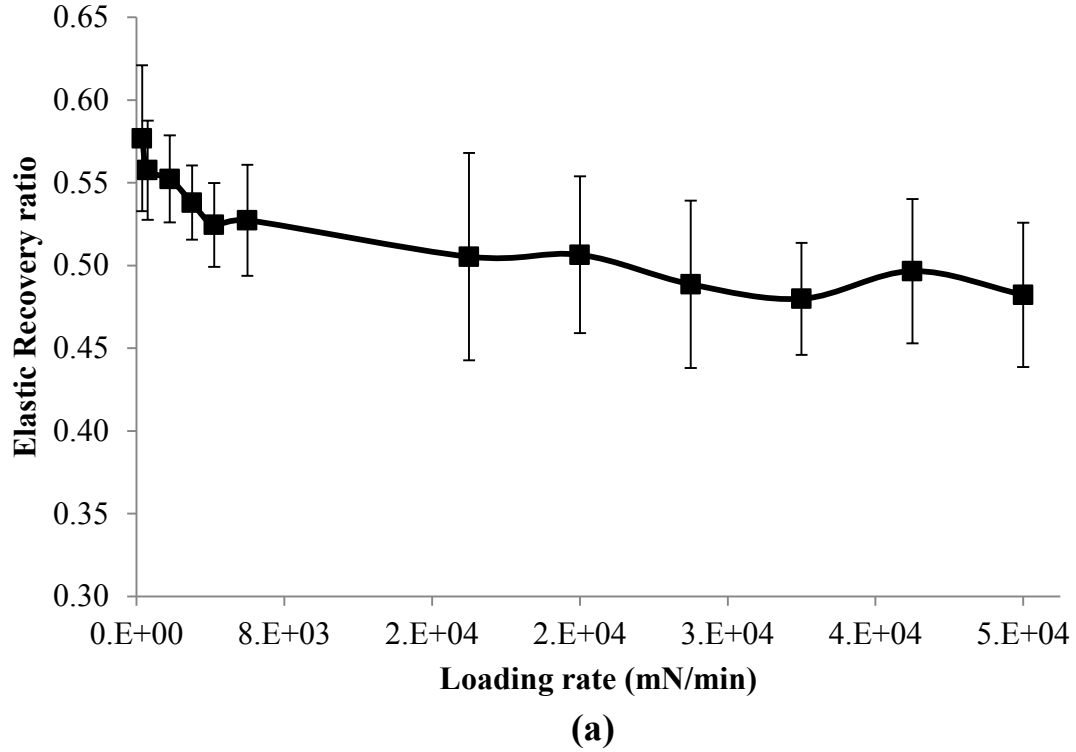

(a)

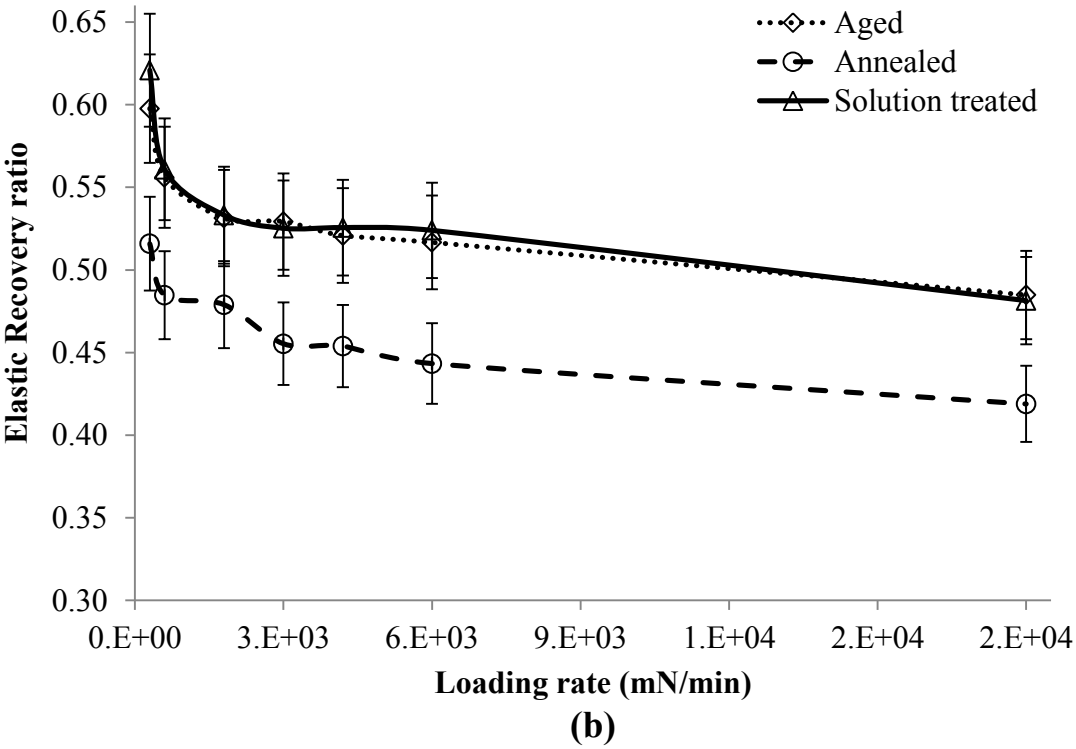

(b)

Figure 4.12 Elastic recovery ratio as a function of loading rate: (a) equiatomic TiNi, (b) 60NiTi (aged, annealed and solution treated)

Table 4.1 Mechanical properties of equiatomic TiNi, 60NiTi (aged, annealed and solution treated) and AISI 304 stainless steel

Properties	Hardness (H) (GPa)	Young's Modulus (E) (GPa)	Elastic Recovery Ratio	E/H
Equiatomic TiNi	3.2	49.8	0.53	15
60NiTi (aged)	9.7	121.6	0.53	12
60NiTi (annealed)	5.3	92.7	0.46	17
60NiTi (solution treated)	9.3	113.3	0.53	12
AISI 304* stainless steel	2.7	229	0.07	85

* Farhat, Z., & Zhang, C. (2010).

The average hardness and the average Young's modulus values are plotted as a function of loading rate, as shown in Figures 4.13 and 4.14, respectively. The error bars indicate the scatter in average hardness and Young's modulus data calculated for various maximum loads at different loading rates. As the loading rate is increased, there is no significant change in the hardenss and Young's modulus. According to Figures 4.13(b) and 4.14(b), annealed 60NiTi showed lower hardness and Young's modulus compared to aged and solution treated 60NiTi.

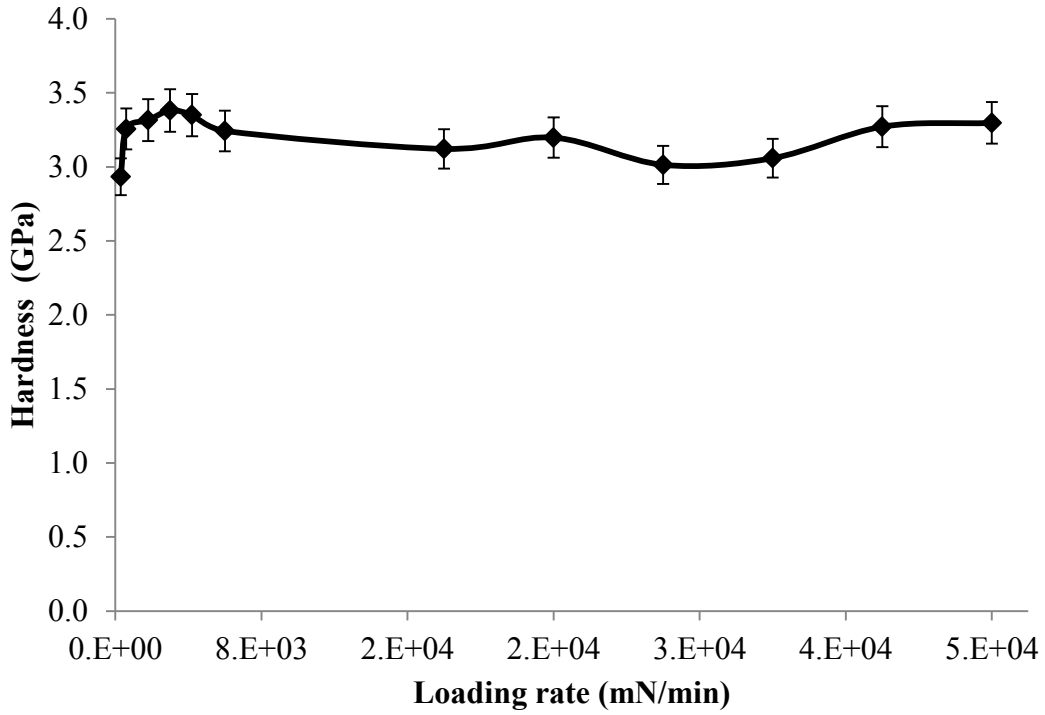

(a)

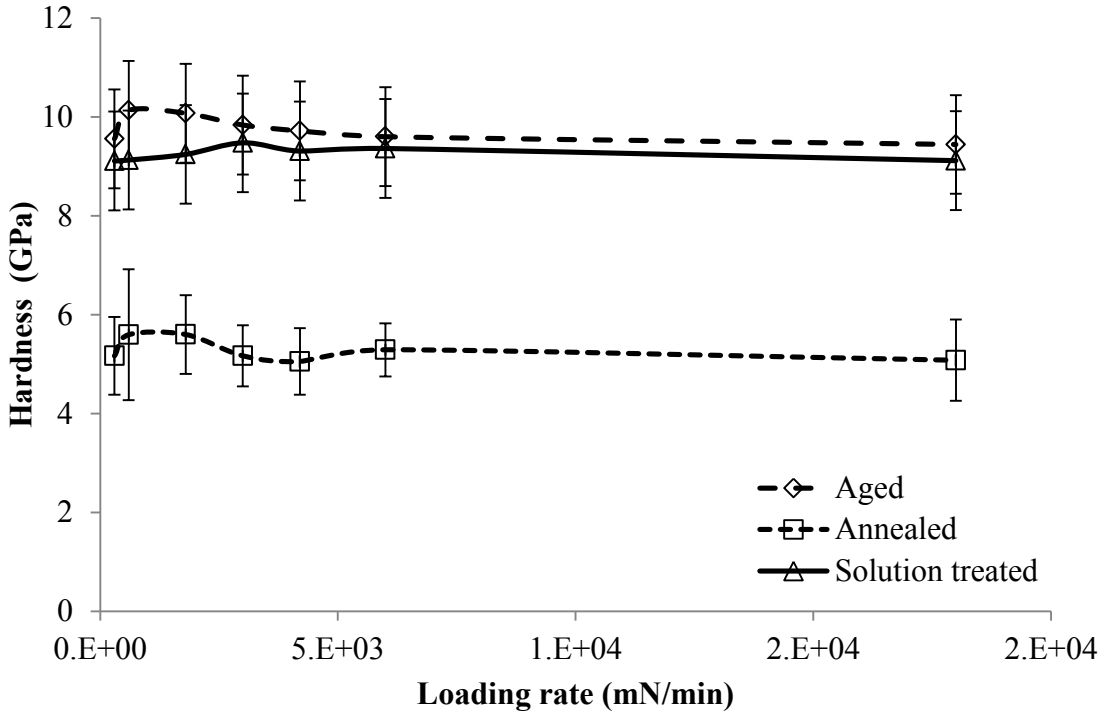

(b)

Figure 4.13 Hardness as a function of loading rate: (a) equiatomic TiNi, (b) 60NiTi (aged, annealed and solution treated)

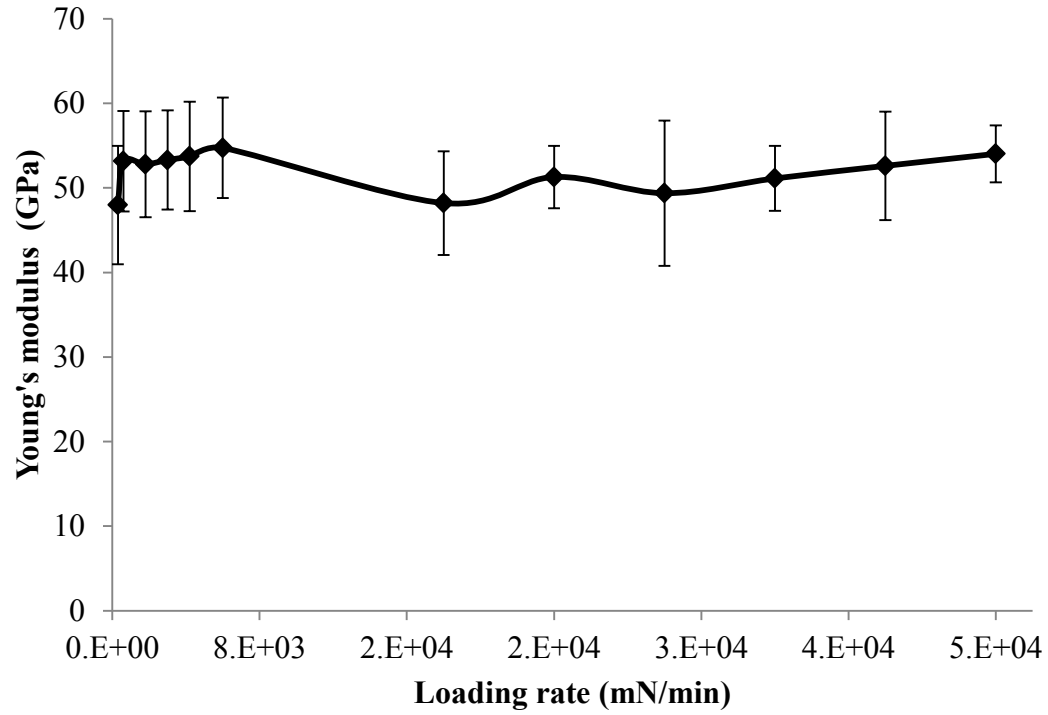

(a)

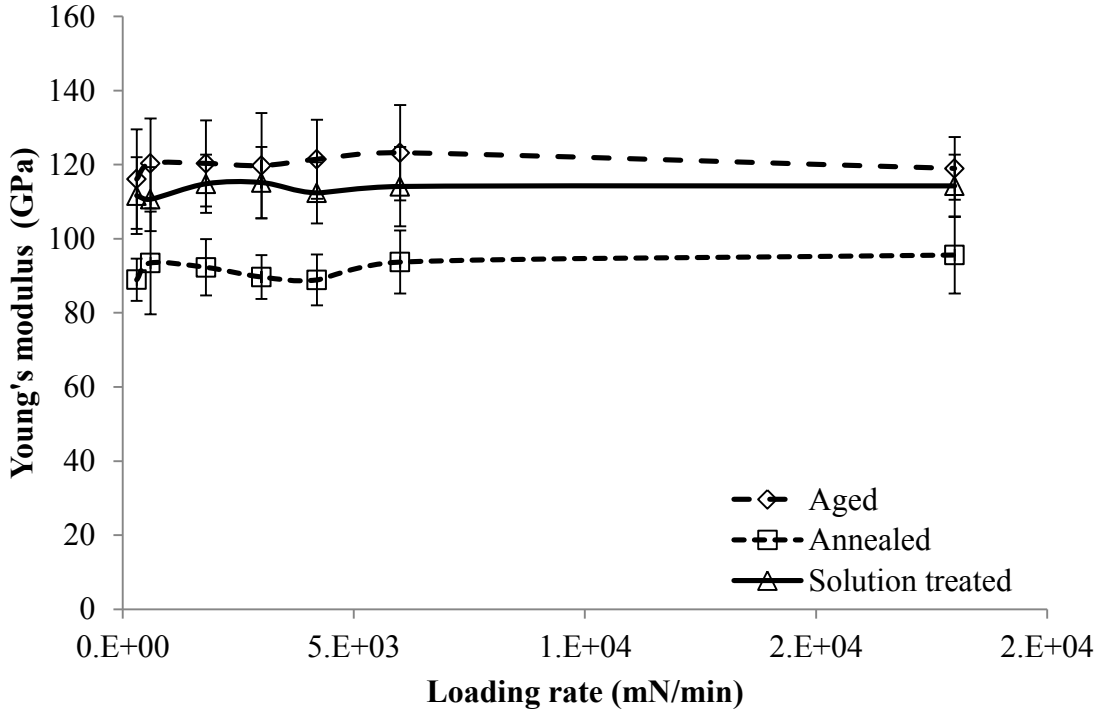

(b)

Figure 4.14 Young's modulus as a function of loading rate: (a) equiatomic TiNi, (b) 60NiTi (aged, annealed and solution treated)

4.2.2 Indentation using Spherical and Sharp Indenters

Superelastic behavior of TiNi is further investigated under high normal loads and high loading rates using spherical and sharp indenters. Indentation test conditions for superelastic TiNi with spherical and sharp indenters are given in Table 3.4. Identical experiments were performed on AISI 304 steel for comparison. Loading and unloading curves (load vs. depth) were plotted at various loading rates. Each test was repeated two times to ensure accuracy and reproducibility of results.

Load-depth curves as a function of loading rate under 700N maximum load, generated using a spherical indenter are shown in Figure 4.15. The curves in Figure 4.15 represent typical load versus displacement patterns. It is clear from the figure that most deformations have recovered during unloading as a result of superelastic behavior. And, the change in loading rate does not seem to have significant effect on the trend and shape of load versus depth curves. These tests seem to exhibit more scatter compared to those generated using Berkovich indenter.

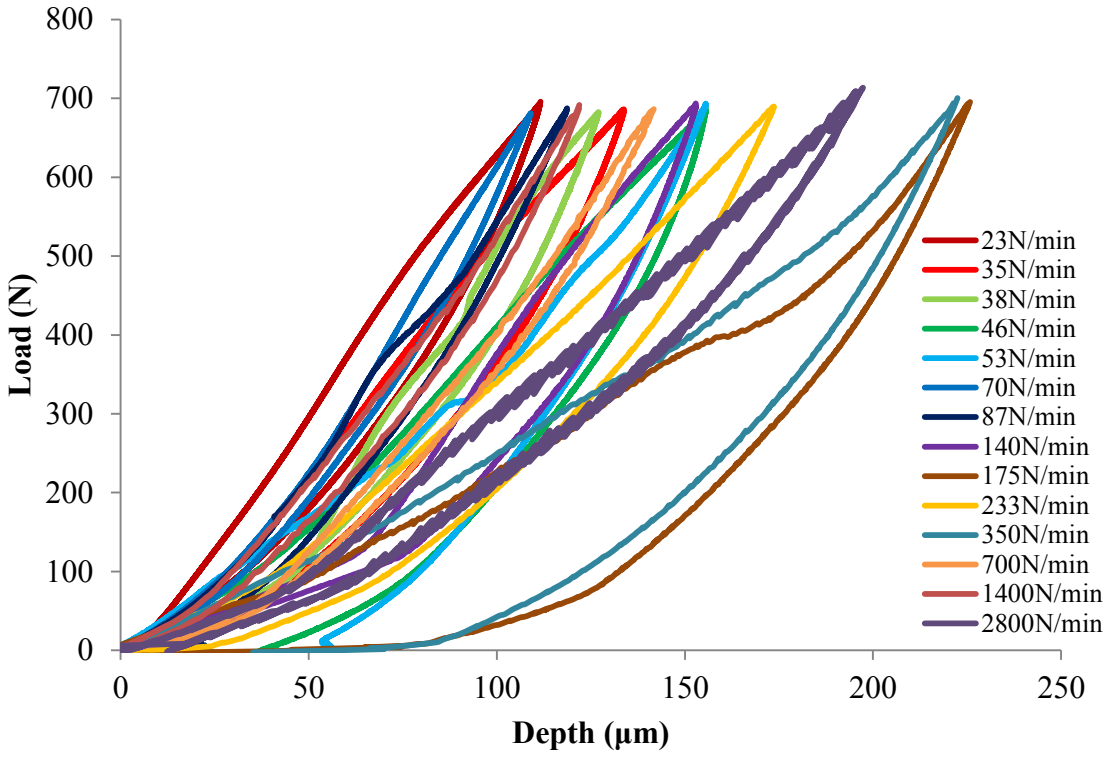

Figure 4.15 Loading-unloading curves of superelastic TiNi using spherical indenter under various loading rates

Furthermore, loading-unloading curves generated using a sharp indenter as a function of loading rate are given in Figures 4.16. The curves show typical load versus depth patterns. It is also evident from Figure 4.16, that indentation performed using the sharp indenter show residual strain as a result of plastic deformation post unloading. In contrast, strains generated using the spherical indenter were recovered after unloading to higher extent (Figure 4.15).

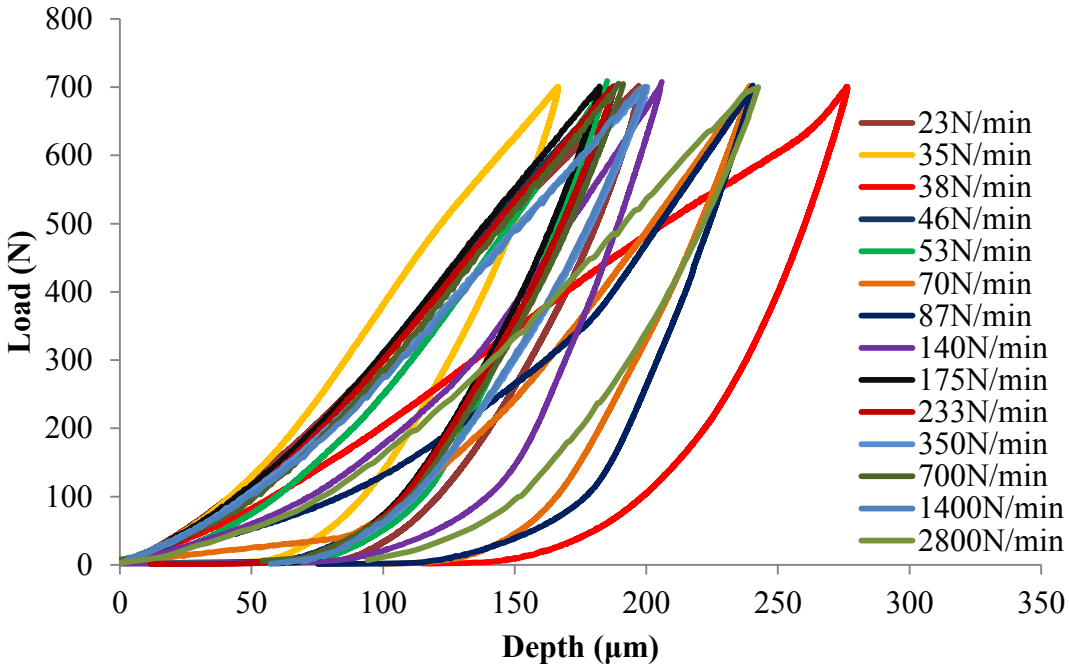

Figure 4.16 Loading-unloading curves of superelastic TiNi using sharp indenter under various loading rates

On the other hand, the deformation behavior of AISI 304 stainless steel is found to be different from superelastic TiNi. Loading-unloading curves under spherical indenter are shown in Figures 4.17, while the curves under sharp indenter are shown in Figure 4.18. The curves generated using spherical indenter show small recoverable deformation as compared to sharp indenter. An average recovery of about 20% is observed for AISI 304 stainless steel as compared to 70% recovery for superelastic TiNi.

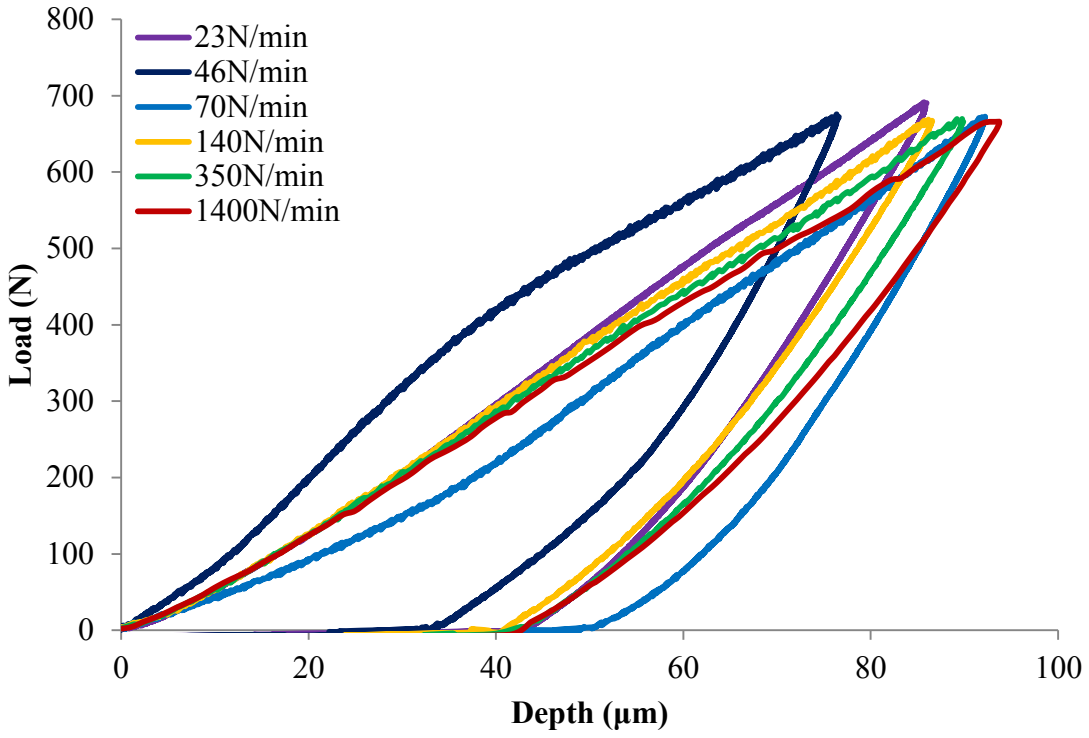

Figure 4.17 Loading-unloading curves of 304 stainless steel using spherical indenter under various loading rates

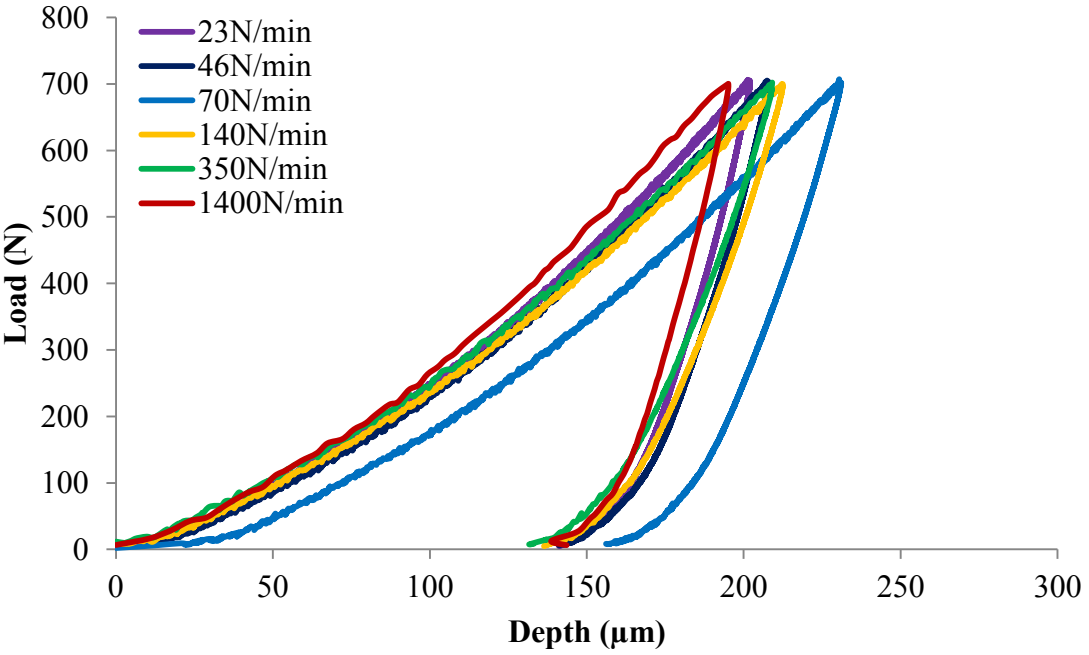

Figure 4.18 Loading-unloading curves of 304 stainless steel using sharp indenter under various loading rates

The elastic recovery ratio calculated from force-displacement curves and plotted as a function of loading rates is given in Figure 4.19. The average elastic recovery ratios for superelastic TiNi using spherical and sharp indenters are 0.73 and 0.51, respectively. On the other hand, the average elastic recovery ratios for AISI 304 steel using spherical and sharp indenters are 0.28 and 0.23, respectively. The error bars indicate the scatter of the elastic recovery ratios calculated for various loading rates. Indentation using a spherical indenter exhibits higher elastic recovery ratio than the sharp indenter, which is attributed to large unrecoverable plastic deformation at the tip of the sharp indenter. It is interesting to note that elastic recovery ratios computed using Berkovich indenter and the sharp pyramidal diamond indenter (under wide range of loading rates) are similar, i.e., 0.53 using Berkovich and 0.51 using pyramidal indenter. The average elastic recovery ratio for superelastic TiNi is higher than that of AISI 304 stainless steel, which has similar hardness. This behavior is to be expected as the AISI 304 stainless steel undergoes a non-recoverable plastic deformation while superelastic TiNi undergoes recoverable deformation. The present experimental results show that superelastic TiNi has superior recovery during indentation loading conditions and can accommodate high localized compressive loads without permanently deforming.

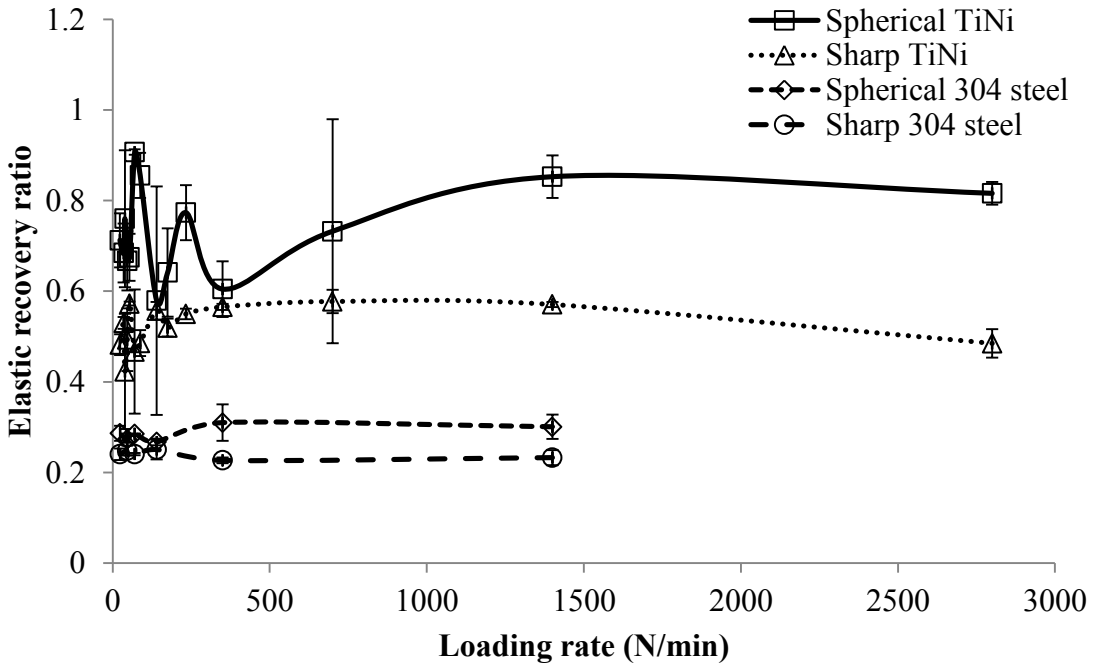

Figure 4.19 Elastic recovery ratio as a funstion of loading rate using spherical and sharp indenters

4.2.3 Prediction of Indentation Behavior of Superelastic TiNi

During indentation loading of superelastic TiNi, it initially undergoes pure elastic deformation of the austenite phase. In this stage the contact mechanics and stress distribution under the indenter follow Hertzian type contact. This behaviour is similar to that of ductile single phase materials with no phase transformation. However, when the load applied to the indenter reaches some critical value, a transformation from austenite to martensite and detwinning of martensite take place. The transformation involves a drop in the elastic modulus, which in turn, affects the stress distribution below the indenter. Upon further loading, martensite deforms elastically and alters the elastic modulus of the system, which again modifies subsurface stresses. As the load increases further, the stress level reaches the yield stress of martensite, upon which plastic deformation takes effect. It should be emphasized that the volume and distribution of austenite and martensite, and subsequently the elastic moduli under the indenter, change with applied load in accordance with the stress distribution beneath the surface. Due to the evolution of regions of all austenite, all martensite and regions where both austenite and martensite exist (where the transformation takes place), it is difficult to determine the size and exact location of these regions. Furthermore, given that both deformation and transformation occur simultaneously in different regions under the indenter and as each region has different elastic modulus, it is difficult to predict the overall deformation from current single phase indentation models (Amini, Yan, & Sun, 2011).

In indentation experiments, the elastic modulus and hardness of the materials are normally determined from the upper 25% of the unloading curve. Therefore, based on the above argument, the elastic modulus of superelastic material determined from indentation tests employing Oliver and Pharr (Oliver & Pharr, 1992) method takes into account only the interaction between deformation and phase transformation in the upper 25% of the unloading curve. This is because the elastic modulus of TiNi determined from indentation is a function of load (i.e., and depth). At every load value in the load versus depth curve obtained from indentation experiments, the elastic modulus is controlled by the individual elastic deformation contributions from austenite, martensite and elasticity that accompanies transformation and detwinning of martensite.

In order to enhance our understanding of the indentation behaviour of superelastic TiNi, contact area, mean contact pressure, max subsurface shear stress and depth are calculated using an effective modulus that varies with load. For simplicity, Hertzian contact analysis is employed (assuming a rigid spherical indenter). In the present analysis, an effective elastic modulus is defined as follows:

$$E^*_{eff} = E^*_1\left(\frac{\epsilon_1}{\epsilon_t}\right) + E^*_2\left(\frac{\epsilon_2}{\epsilon_t}\right) + E^*_3\left(\frac{\epsilon_3}{\epsilon_t}\right) \qquad \text{Equation 4.1}$$

where,

$$\frac{1}{E^*} = \frac{(1-\nu^2_{TiNi})}{E_i} + \frac{(1-\nu^2_{indenter})}{E_{indenter}} \qquad \text{Equation 4.2}$$

The parameters in Equation 4.1 are determined from the stress-strain diagram for superelastic TiNi given in Figure 4.20. E_i's and ϵ_i's are the slopes of the lines and their corresponding strains associated with regions 1, 2 and 3 in the diagram and ϵ_t is the total strain. Table 4.2 gives the parameters used in Equation 4.1. The effective modulus (E_{eff}^*) is the weighted average of contributions from the initial elastic austenite region (E_1), the superelastic (plateau) region (E_2), and the elastic martensite region (E_3), respectively. ϵ_2, ϵ_3 and ϵ_t are stress dependent and are calculated as follows:

region 1, $0 \le \sigma < \sigma_{fs}, \epsilon_t = \epsilon_1$ Equation 4.3(a)

region 2, $\sigma_{fs} \le \sigma \le \sigma_{ff},\ \epsilon_t = \epsilon_1 + \epsilon_2,\ where\ \epsilon_2 = \left(\frac{\sigma-\sigma_{fs}}{E_2}\right)$ Equation 4.3(b)

region 3, $\sigma_{ff} < \sigma < \sigma_y,\ \epsilon_t = \epsilon_1 + \epsilon_2 + \epsilon_3,\ where\ \epsilon_3 = \left(\frac{\sigma-\sigma_{ff}}{E_3}\right)$ Equation 4.3(c)

where, σ_{fs} and σ_{ff} are the forward start and finish transition stresses and σ_y is the yield strength of martensite (see Figure 4.20). The effective elastic modulus (E^*_{eff}) represents an average value for the system. In other words, it is assumed that the elastic modulus at any point below the surface is constant for a given load and indenter depth and is equal to E_{eff}^*.

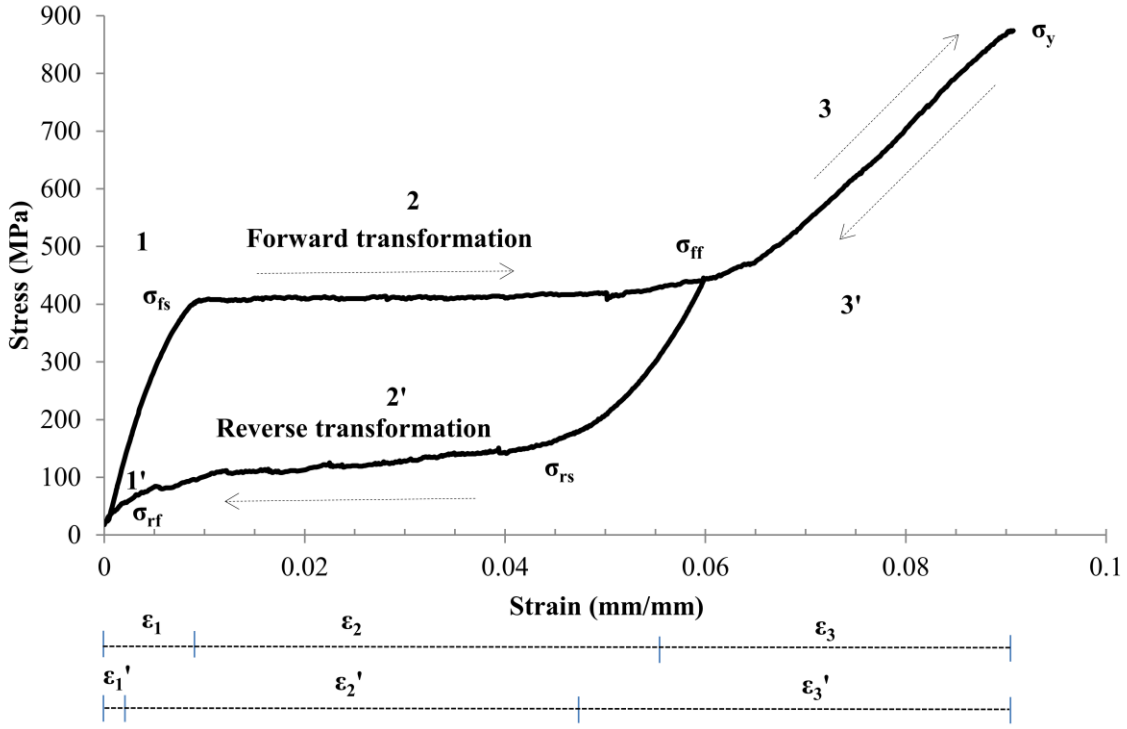

Figure 4.20 Room temperature stress-strain curve for superelastic TiNi

Table 4.2 Parameters for Equation 4.1

	E_1 (MPa)	E_2 (MPa)	E_3 (MPa)	σ_{fs} (MPa)	σ_{ff} (MPa)	σ_{rs} (MPa)	σ_{rf} (MPa)	F_{fs} (N)	F_{ff} (N)	F_{rs} (N)	F_{rf} (N)
Loading	44000	330	18000	410	426	-	-	9	205	-	-
Unloading	44000	2000	18000	-	-	180	60	-	-	63	0.7

Note: *ε_1 is 9 x 10^{-3} for loading and 2 x 10^{-3} for unloading, ε_2 and ε_3 are calculated at increment of 50MPa from stress-strain diagram (region 2 and 3 in Figure 4.20).*

During unloading, the reverse process takes place, i.e., elastic recovery of martensite, martensite to austenite transformation and elastic recovery of austenite. All these mechanisms, simultaneously, occur at different depths under the indenter. Similarly, the effective elastic modulus for the unloading cycle can be calculated using Equation 4.1. Here, regions 1, 2 and 3 are replaced by regions 1', 2', and 3' and are associated with the unloading path in Figure 4.20. ϵ_1, ϵ_2 and ϵ_3 are replaced by ϵ_1', ϵ_2' and ϵ_3', respectively. ϵ_t is calculated from Equation 4.3 by substituting σ_{fs} and σ_{ff} with σ_{rs} and σ_{rf}, where σ_{rs} and σ_{rf} are the reverse transformation start and finish stresses. Parameters used for the calculations of E_{eff}^* for the unloading path are given in Table 4.2.

Now, in order to determine the indentation load corresponding to a given stress (σ) in Figure 4.20, the following equation is used (Fischer-Cripps A. C., 2007),

$$F = (\pi\sigma)^3 \left(\frac{3R}{4E^*}\right)^2 \qquad \text{Equation 4.4}$$

where, R is the indenter radius. The load corresponding to any σ can be determined from Equation 4.4 by substituting E_{eff}^* for E^*. The dependence of the effective elastic modulus (E_{eff}^*) of superelastic TiNi on indentation load is shown in Figure 4.21. The loading curve in the figure shows that the value of E_{eff}^* is constant in the load range $0 \leq F < F_{fs}$, where F_{fs} is the load at which the forward austenite to martensite transformation starts (see insert in Figure 4.21). In this range, the value of E_{eff}^* is the elastic modulus of austenite which correspond to the first term in Equation 4.1. In the load range $F_{fs} \leq F \leq F_{ff}$ (forward finish transition load) the effective elastic modulus drops sharply due to the austenite to martensite transformation and detwinning of martensite that is accompanied by large strain. The value of E_{eff}^* in this range is calculated from the first and second terms in Equation 4.1. Here, the contribution from both austenite elasticity and strain associated with transformation are combined, as both process take place simultaneously at different depths in the specimen. With increasing load, E_{eff}^* continues to drop as the contribution of the superelastic transformation increases. When the load is raised above F_{ff}, martensite undergoes elastic deformation up to its yield load. The effective elastic modulus in this load range is determined by adding the contributions associated with austenite, austenite to martensite transformation, and elastic deformation of martensite (Equation 4.1). The reason for adding all three contributions in this load range is that all effects are taking place simultaneously at different depths under the indenter. In this region, the value of E_{eff}^* rises gradually with load, as the contribution of the elastic deformation of martensite increases (see insert in Figure 4.21).

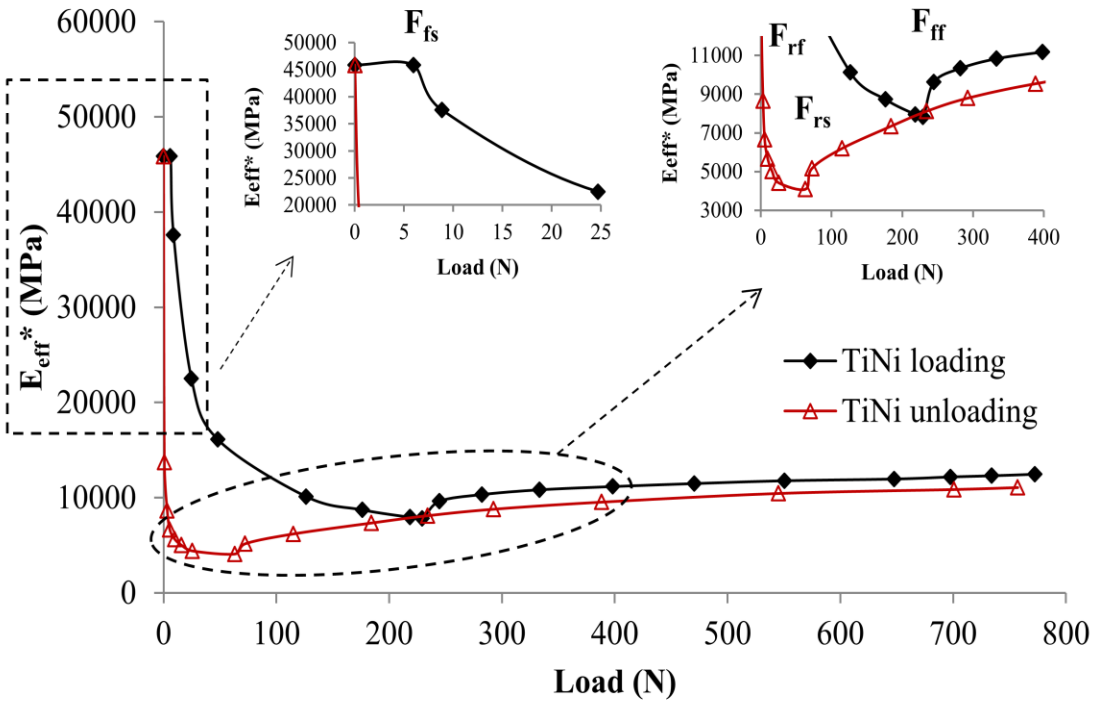

Figure 4.21 Effective elastic modulus of superelastic TiNi as a function of indentation load

Upon unloading, the contribution of the elastic recovery of martensite is dominant and decreases slowly as the load is reduced down to F_{rs}, which is the start of the reverse transformation from martensite to austenite. Reducing the load below F_{rs} reduces the effective elastic modulus as a result of the reverse transformation. When the transformation is complete at F_{rf}, only austenite elastic recovery takes place and E_{eff}^* rises sharply. It should be emphasized, here, that similar to the loading cycle, during unloading, in region where $F > F_{rs}$, elastic recovery of martensite, reverse transformation and recovery of austenite all occur simultaneously at different depths and their individual contributions vary with load. For the load range $F_{rf} \leq F \leq F_{rs}$, recovery is due only to the reverse transformation and elasticity of austenite. While, for $F < F_{rf}$, only austenite contributes to elastic recovery. As expected, the values of F_{rs} and F_{rf} for the unloading curve are lower than F_{ff} and F_{fs} of the loading curve, respectively.

Employing the Hertzian theory, the contact radius (a) can be determined from (Fischer-Cripps A. C., 2007):

$$a^3 = \frac{3FR}{4E^*} \qquad \text{Equation 4.5}$$

where, F is the applied indentation load and R is the effective radius, which is related to the radius of the individual components by,

$$\frac{1}{R} = \frac{1}{R_{indenter}} + \frac{1}{R_{specimen}} \qquad \text{Equation 4.6}$$

In this study, specimens are flat, which makes $R_{specimen} = \infty$ and $R = R_{indenter}$. The intensity of the contact field can be determined from the mean contact pressure (P_m),

$$P_m = \frac{F}{\pi a^2} \qquad \text{Equation 4.7}$$

While, the maximum shear stress (τ_m), located along the contact axis at a depth of 0.5a below the surface, can be calculated from,

$$\tau_m \approx 0.48 P_m \qquad \text{Equation 4.8}$$

Table 4.3 summarizes the data for the tungsten carbide (WC) ball, superelastic TiNi, and AISI 304 stainless steel (Farhat & Zhang, 2010) used in the Hertzian analysis.

Table 4.3 Data for Hertzian analysis

	Elastic Modulus, E (GPa)	Poisson's Ratio, ν	Radius, R (mm)	Yield Stress (MPa)
TiNi	(Table 4.2)	0.33	-	872
AISI 304 stainless steel	229	0.30	-	900
WC ball	600	0.26	3.18	-

The variation of maximum shear stress and its depth beneath the surface of TiNi and AISI 304 steel are given in Figure 4.22(a,b). It is apparent from the figure that the superelastic TiNi behaves in a manner that is different from conventional elastic materials. The loading curve in Figure 4.22(a) shows that TiNi maximum shear stress increases rapidly with applied load. This rapid rise in τ_m is associated with the pure

austenite phase. τ_m continues to rise upto the austenite to martensite transformation load (F_{fs}). At transformation load the maximum shear stress remains steady with increasing applied load as a result of the martensite transformation and detwinning of martensite. This plateau at τ_m is accompanied by drop in the effective elastic modulus (E_{eff}^*) up to the load corresponding to the end of the transformation (F_{ff}) (Figure 4.21). This behaviour can be explained as follows. When the transition load (F_{fs}) is reached the volume of material where the transformation occurs expands rapidly as a result of superelastic behaviour, analogous to the rapid increase in strain when the transition stress is reached in uniaxial tensile loading. That is, the contact area increases at a rate that gives no significant increase in τ_m. Above the load where martensite transformation and detwinning occurs (F_{ff}), martensite starts to deform elastically and continues to deform until it reaches the yield load of martensite. In this load range, the value of τ_m increases gradually with load. The unloading curve in Figure 4.22(a) show a drop in maximum shear stress as the load drops down to F_{rs}, where the reverse transformation begins. Below this load the maximum shear stress drops at a lower rate down to F_{rf}, below which only austenite exists and rapid drop in maximum shear stress occurs. In general, the depth where maximum shear exists increases with load (Figure 4.22(b)). However, a drop in depth of maximum shear occurs as the load is raised above F_{ff} and martensite begins to deform elastically. The unloading curve show similar trend, i.e., a drop in depth of maximum shear stress with load down to F_{rs}, where slight rise in depth as the reverse transformation begins, followed by rapid drop in depth of τ_m as the contribution of austenite increases.

The general trend of AISI 304 follows an expected pattern for conventional elastic material, where the max shear stress and its depth increase with applied load. The steel shows a very rapid increase and high max shear stress compared to TiNi, although both TiNi and 304 stainless steel have similar hardness, as evident from the insert in Figure 4.22(a). The variation is attributed to lower effective elastic modulus associated with TiNi as a result of superelastic effect. The depth of the max shear stress is much higher in TiNi compared to AISI 304 stainless steel (see insert in Figure 4.22(b)).

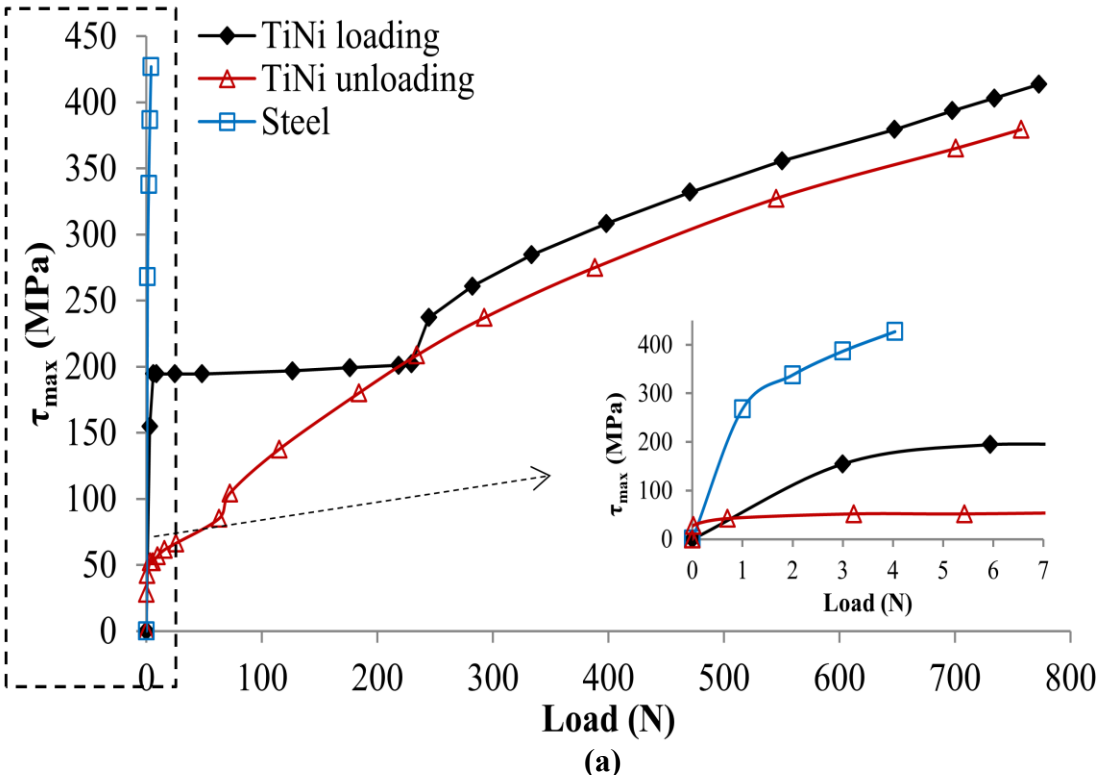

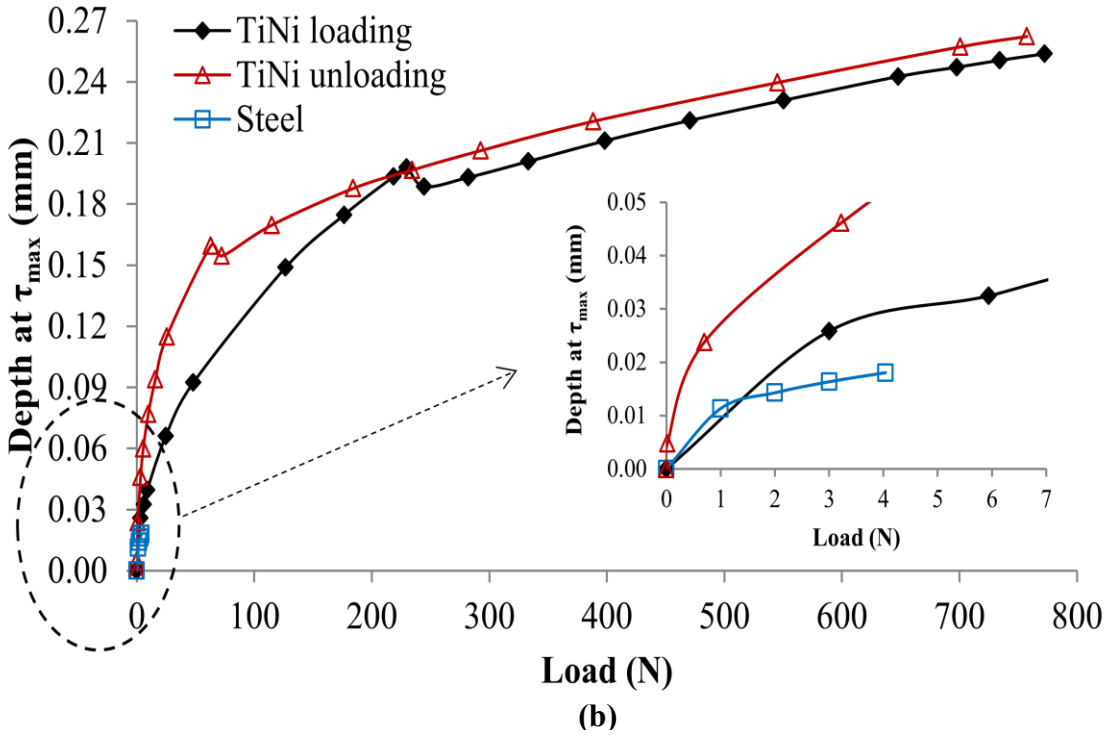

Figure 4.22 (a) Maximum shear stress as a function of applied indentation load, (b) Depth at maximum shear stress as a function of applied indentation load

The mean contact pressure (P_m) and contact area as functions of applied indentation load are plotted in Figure 4.23(a,b). It is evident from the figure that the mean contact pressure increase sharply at low loads (in the austenite range) until a plateau is reached, where austenite to martensite transformation takes effect. This plateau is accompanied by sharp increase in contact area as a result of a drop in the effective elastic modulus associated with the transformation. In this region, as the load is increased the contact area is increased accordingly to maintain constant mean pressure. As this takes place, the transformation zone under the indenter increases. Post transformation the contact area initially drops slightly as martensite begins to contribute to the effective elastic modulus of the system. This behavior is followed by gradual increase in contact area and mean contact pressure with applied load as the contribution of the elastic deformation of martensite to the effective elastic modulus rises. The plots for the steel follow the expected increase in the mean pressure with load and small rise in contact area (see inserts in Figure 4.23(a,b)). It is noted that plastic deformation in AISI 304 stainless steel starts at about 4N load, which corresponds to a mean pressure of about 900 MPa (i.e. yield strength in tension). Here, plastic deformation is initiated 18 μm below the surface as the maximum shear stress reaches about 450 MPa. On the other hand, superelastic TiNi begin to deform plastically when the indentation load reaches 770 N, which corresponds to a mean pressure of about 872 MPa (i.e. yield strength of martensite). Plastic deformation in superelastic TiNi starts at maximum shear stress of 435 MPa at 250 μm below the surface. This argument reflects the large size of the transformation zone for TiNi. That is, the transformation begins when the maximum shear stress reaches about 200 MPa at a load of about 6 N and depth of about 30 μm below the surface. And as the load is increased the transformation zone extends to about 250 μm below the surface at the onset of martensite yielding at 872 MPa. While, the depth of the plastic zone at the onset of yielding for 304 steel is only 18 μm. The large size of the transformation zone for superelastic TiNi explains the large elastic recovery observed in indentation tests.

Based on the above analysis, the superior dent resistance of superelastic TiNi over steel, which has similar hardness, is evident. The load (applied through a given spherical indenter) that induces plastic deformation in superelastic TiNi is over two orders of magnitude higher than that of AISI 304 steel.

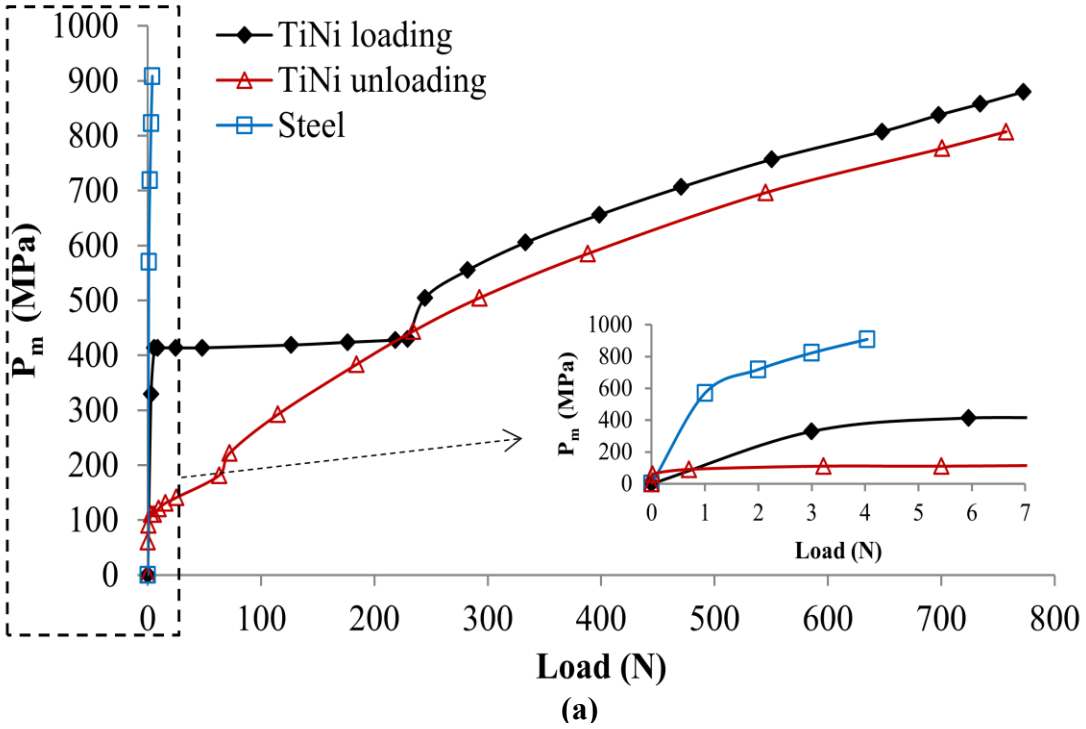

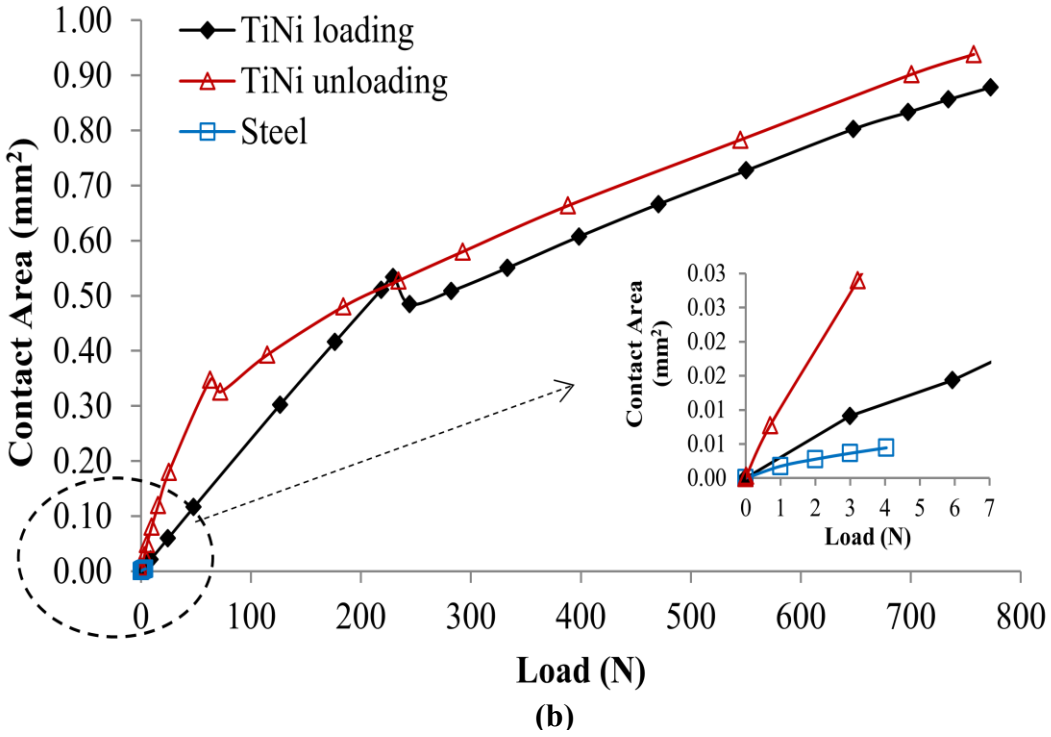

Figure 4.23 (a) Mean contact pressure as a funtion of applied indentation load, (b) Contact area versus load

Furthermore, the residual indentation of superelastic TiNi and AISI 304 stainless steel were examined using SEM and optical profiler. Figure 4.24(a,b) shows SEM images of indentations performed using about 600 N load for AISI 304 steel and superelastic TiNi using 3.18 mm spherical indenter. It is apparent that TiNi residual impression is significantly unnoticeable compared to that for steel. This behaviour is attributed to higher contact area, lower mean pressure and larger recovery associated with superelastic TiNi as compared to AISI 304 steel. Optical profiler scan post indentation also reveals the superior depth recovery for superelastic TiNi (Figure 4.25 (a,b)). It is interesting to note that although the applied load is below the martensite yield load for TiNi, the profile scan shows residual depth of about 5 μm (Figure 4.26). This behavior might be due to the fact that the material surrounding indentation is constrained, which hinders full reversible transformation and recovery.

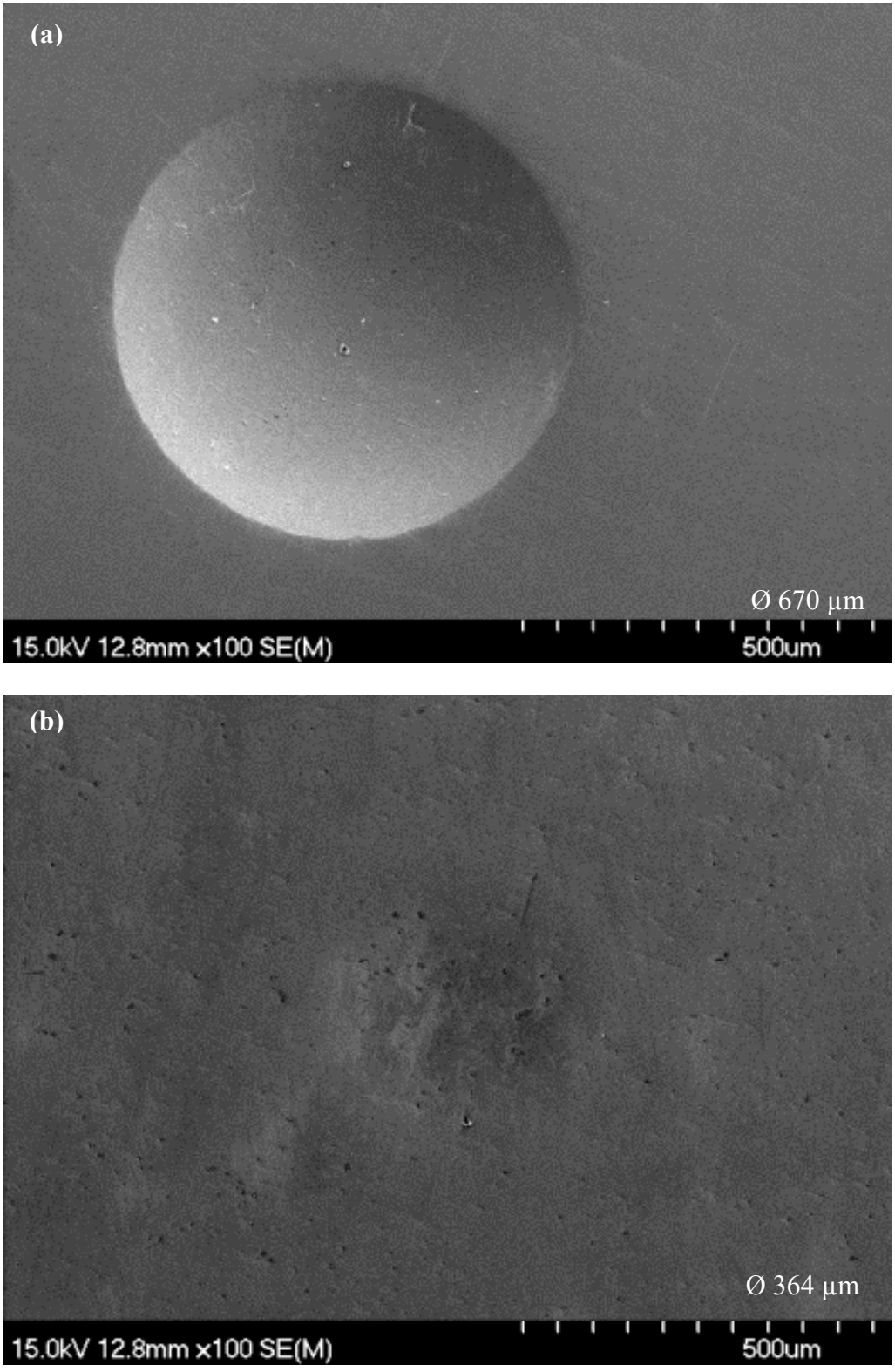

Figure 4.24 SEM micrograph of indentations performed using 600 N load for: (a) AISI 304 steel, and (b) superelastic TiNi

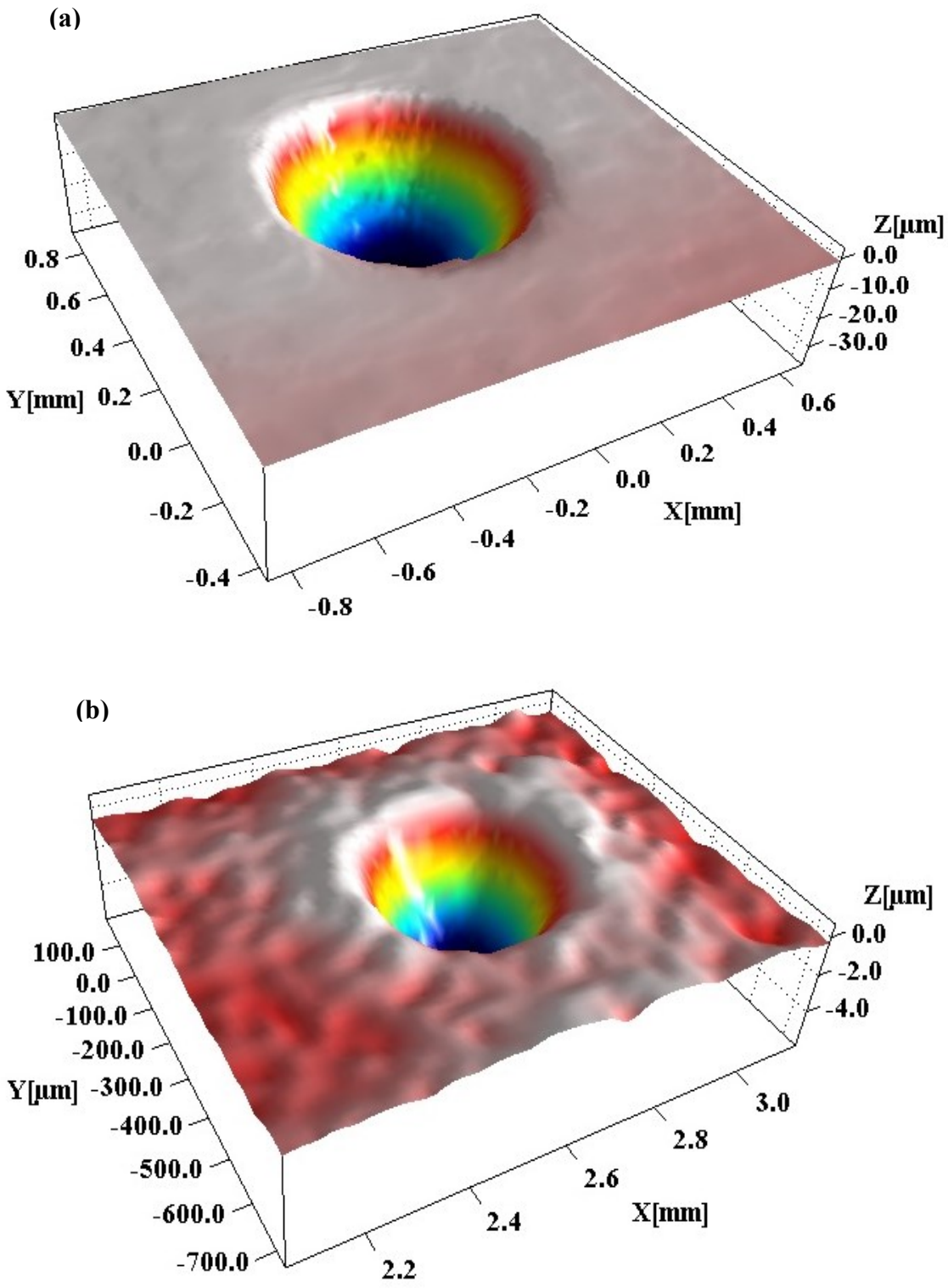

Figure 4.25 Optical profiler image of indentations performed using 600 N load for: (a) AISI 304 steel, and (b) superelastic TiNi

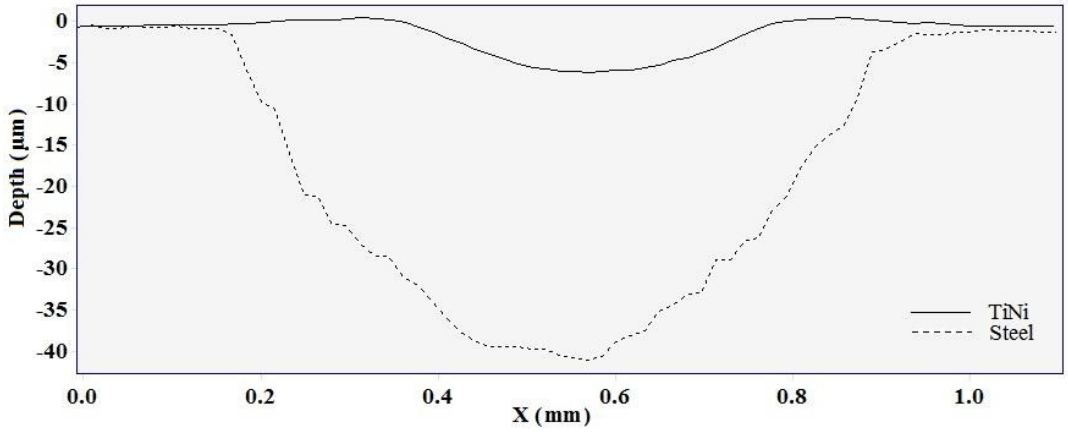

Figure 4.26 Steel and TiNi indentation depth under 600 N load and spherical indenter (section is through the middle of indentation in Figure 4.25)

Next, the effect of the effective elastic modulus on the load versus depth curve of superelastic TiNi is examined and the predicted curve is validated against experimental data. According to Hertzian contact theory, the load-depth relationship for spherical indenter is given by (Fischer-Cripps A. C., 2007),

$$F = \frac{4}{3} E^* R^{\frac{1}{2}} h^{\frac{3}{2}} \qquad \text{Equation 4.9}$$

where, h is the depth of indentation. In this study, the E^* is substituted with the effective modulus of elasticity developed above and given by Equation 4.1. Figure 4.27(a) gives the loading cycle of the predicted and experimental load-depth curves. The predicted curve is in good agreement with the experimentally obtained curve, in particular, in the load range upto 250 N. In this load range, the depth of penetration increase with applied load upto the end of the austenite to martensite transformation load (F_{ff}) of about 229 N. Elastic deformation of austenite, followed by martensitic transformation accompanied by large increase in depth (due to drop in E_{eff}^*) dominate this load range. As the load is raised over F_{ff}, a drop in depth occurs as evident from the insert in Figure 4.27(a). Here, the drop in depth is attributed to the onset of elastic deformation of martensite and the associated increase in E_{eff}^*. Raising the load further increases the contribution of martensite elastic deformation to the overall E_{eff}^* and depth continues to increase accordingly. It is interesting to note that the experimental loading curve also shows a drop in depth around F_{ff}, in good agreement with the predicted results. Both F_{ff} and its corresponding depth agree well with the experimental values. However, the drop in depth

in the experimental results is less pronounced than the predicted one and could be missed if the test is not done carefully, i.e., the transition from one region to the other in experimental load-depth data is gradual and sometimes difficult to observe. Past F_{ff} the depth continue to increase and deviation from the experimental curve increases with load. At the maximum load, the difference is about 30%, which represent the maximum possible error. This deviation might be due to the added elastic deformation from detwinning of less favorably oriented martensite grains at loads past F_{ff}. This behavior can result in higher depth than predicted results.

In the unloading cycle of the load-depth curve (Figure 4.27(b)), the reverse process occurs. Here, an increase in the depth is evident as the load (F_{rs}) enters the reverse transformation region and the elastic deformation of martensite ends. As seen in the insert in Figure 4.27(b), there is a good agreement between the predicted and the experimental reverse transition load (F_{rs}) and corresponding depth.

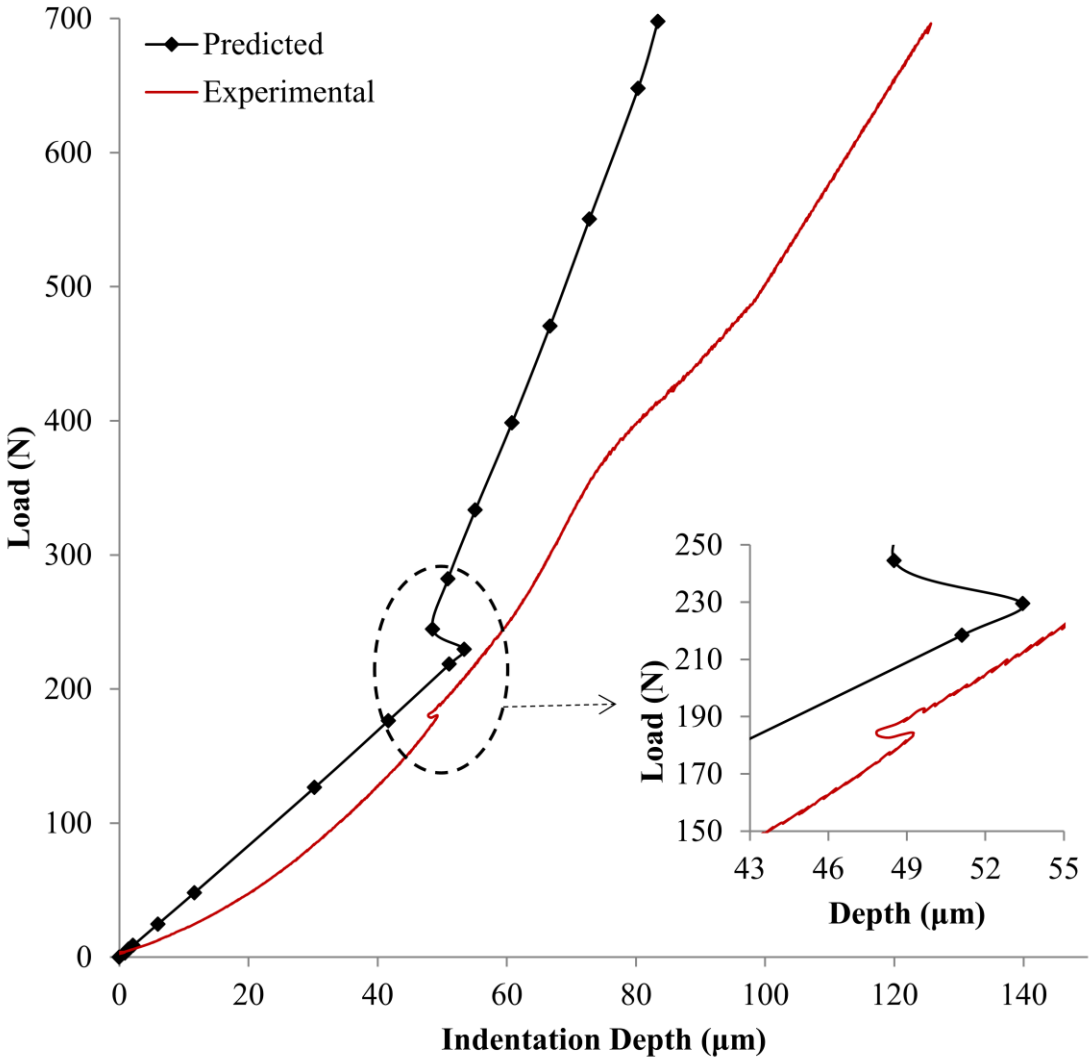
Predicted
Experimental
Load (N)
Indentation Depth (µm)
Depth (µm)
700
600
500
400
300
200
100
0
0
20
40
60
80
100
120
140
250
230
210
190
170
150
43
46
49
52
55

(a)

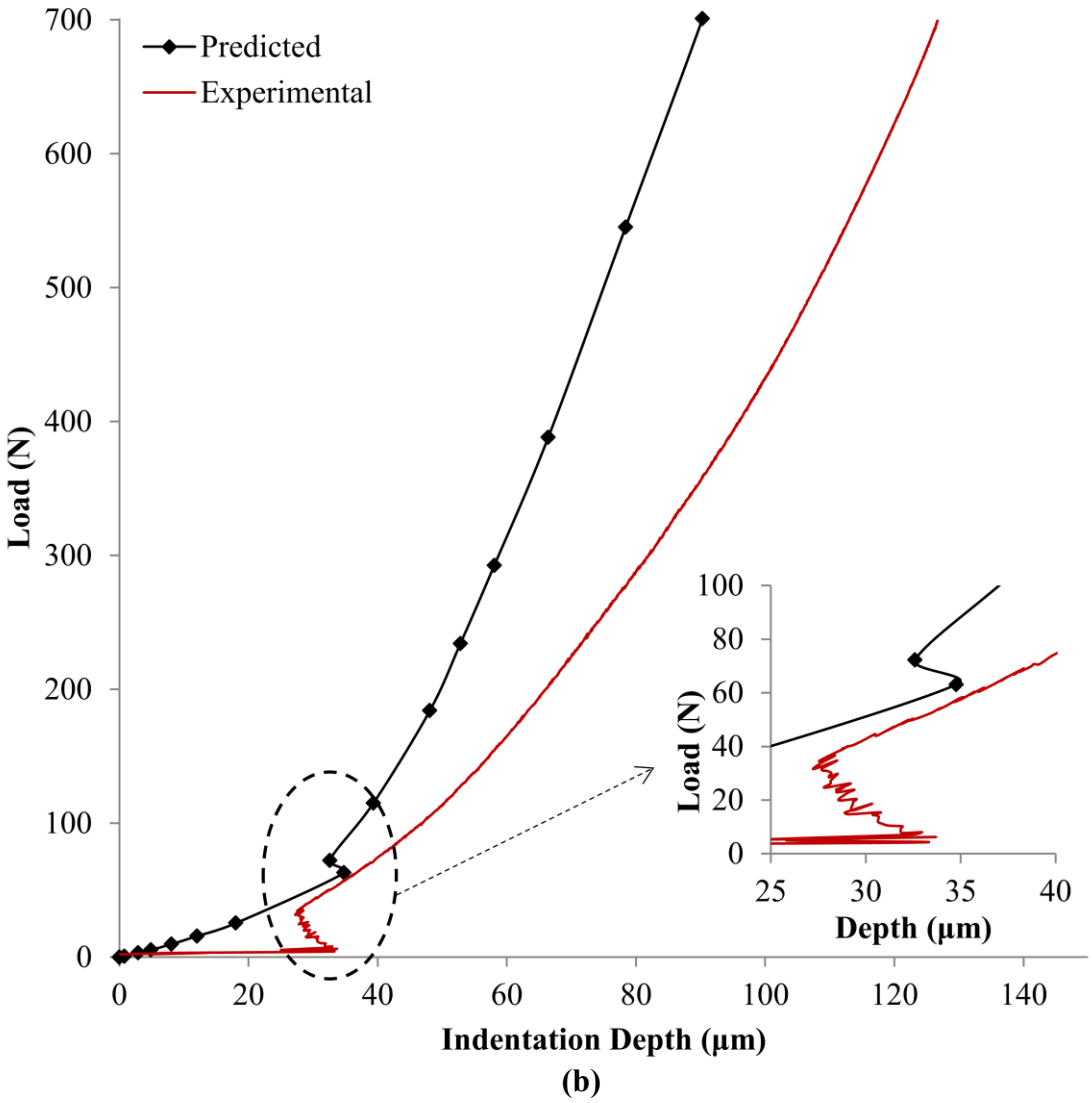

Figure 4.27 Predicted experimental load-depth curves of SE TiNi: (a) loading, (b) unloading

In summary, it is believed, in the present study, that deformation during indentation of superelastic TiNi occurs as follows. Upon loading the austenite phase deforms elastically as any single phase elastic material and the effective modulus in this region is basically that of the austenite phase (1st term in Equation 4.1). Once the transformation load is reached, the austenite to martensite and detwinning of martensite takes place accompanied by large deformation. The transformation begins below the surface at depth where maximum shear stress exists and is surrounded by austenite phase. Since both austenite and austenite-to-martensite take place in this load range, both effects contribute to the effective modulus of elasticity (the first and second terms in Equation 4.1). As the

load increases, the formed martensite deforms elastically. Here, austenite, austenite to martensite transformation and martensite contribute to the overall deformation as all three deformation zones exist below the indenter. That is, martensite is surrounded by a transformation zone, which is, in turn, is surrounded by the austenite phase in accordance with Hertzian shear stress distribution. As the load is increased further, the contribution of martensite elastic deformation increases. Similarly, in the unloading cycle the reverse process occurs but, as expected, the reverse transition loads (F_{rs} and F_{rf}) are lower than those of the loading cycle (F_{fs} and F_{ff}).

From the above discussion, it can be concluded that based on the present work, the elastic modulus obtained from load-depth indentation experiments and calculated using conventional method employed for single-phase materials (such as, Oliver and Pharr method) is not accurate as the effective elastic modulus is a function of indentation depth. Since the experimental elastic modulus is calculated from the upper 25% (Oliver and Pharr) of the unloading curve, it only describes the material at the depth where the slope is taken. Figure 4.28 gives the relationship between E_{eff}^{*} and depth of indentation to further elucidate this argument.

Figure 4.28 clearly illustrates how the effective elastic modulus varies with penetration depth. For low loads (below about 6 N) the effective elastic modulus is that of the austenite phase (see insert in Figure 4.28). As loading continues above the transition load, the effective elastic modulus drops sharply to a steady state value down to a load where phase transition ends and martensite elastic modulus begins to take effect. At this load the depth drops (as given in the insert), while E_{eff}^{*} continues to rise gradually as the load increases. The unloading curve shows a similar trend as the elastic and superelastic deformation reverse. As expected, the unloading path is different from the loading path due to the hysteresis associated with superelastic behaviour. It is clear from Figure 4.28 that the elastic modulus depends on the maximum depth of indentation. For example, if the depth of indentation in an indentation test is below about 2 μm (Figure 4.28 insert) then the measured elastic modulus would be that of austenite only.

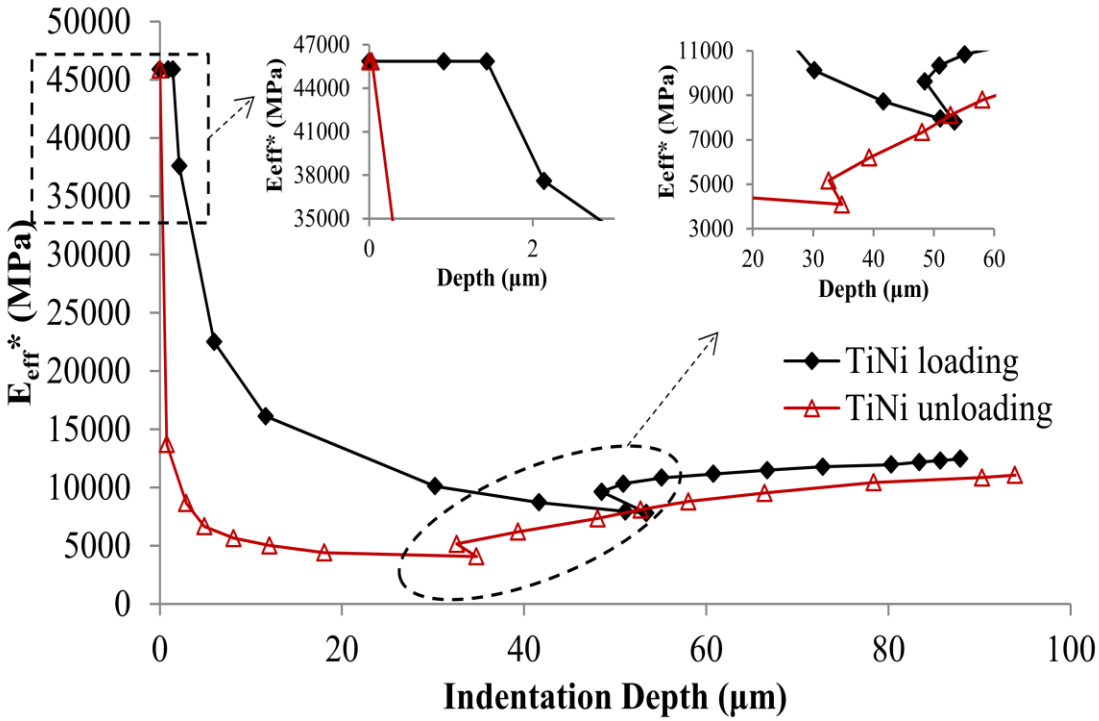

Figure 4.28 Effective elastic modulus as a function of indentation depth

To illustrate how the elastic modulus obtained using the Oliver and Pharr method changes with applied load experimentally, a set of nanoindentation experiments were performed on superelastic TiNi using a Berkovich indenter. Figure 4.29 presents force-displacement (penetration depth of indenter) curves showing the loading-unloading cycles generated under various maximum loads. Here, the figure reveals typical load versus displacement patterns, i.e. a rise in indentation depth with increasing normal load. The curves show high recoverable deformation and relatively small permanent deformation upon unloading. An average of over 60% recovery is observed as a result of elastic and superelastic behavior of TiNi. It is also evident that even the indentation test performed under the lowest load of 40mN shows residual plastic deformation which is expected for sharp indenters. The curves exhibit various hysteresis sizes that increase with maximum load. The elastic modulus is calculated from load-depth curves in Figure 4.29 using the Oliver and Pharr method and plotted as a function of maximum applied load (and corresponding maximum depth). It is clear from Figure 4.30 that the measured elastic modulus significantly varies with maximum load (and depth). This result is not unexpected in light of the above discussion. At low loads, the effective elastic modulus is high due to the high elastic modulus associated with the austenite phase at shallow depths

(austenite dominance). As the load increases, the value of the effective elastic modulus drops as a result of the rise in the contribution of the austenite to martensite transition deformation to the overall effective elastic modulus (martensite dominance). Furthermore, the ratio of the elastic modulus at the two ends of the curve in Figure 4.30 is about 0.61. This ratio compares well to the ratio of elastic modulus of the martensite phase to that of the austenite phase of 0.63 ((Zaki & Moumni, 2007), (Kang, Kan, Qian, & Liu, 2009)). This result confirms the finding in this study, that the effective elastic modulus is indentation depth dependent as depicted in Figure 4.28 (E_{eff} *vs depth). Although Figure 4.30 is generated using sharp indenter (Berkovich), the above argument for spherical indenter is still valid. It can be concluded from this results that the Oliver and Pharr method, which is developed for single phase material without phase transition has limitations when extended to multiphase material with phase transformation as the effective elastic modulus for such material varies with indentation depth. Therefore, the value obtained from Oliver and Pharr method, commonly reported in the literature, represents a composite elastic modulus that is only valid at a particular indentation depth.

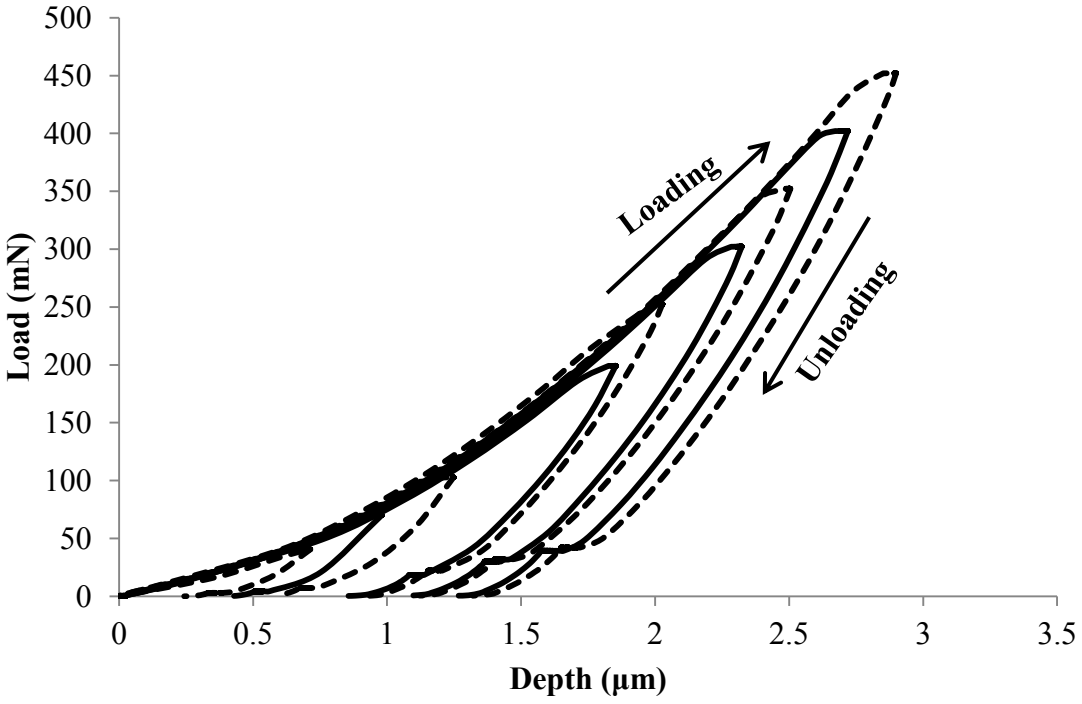

Figure 4.29 Indentation curves performed on superelastic TiNi as a function of maximum loads

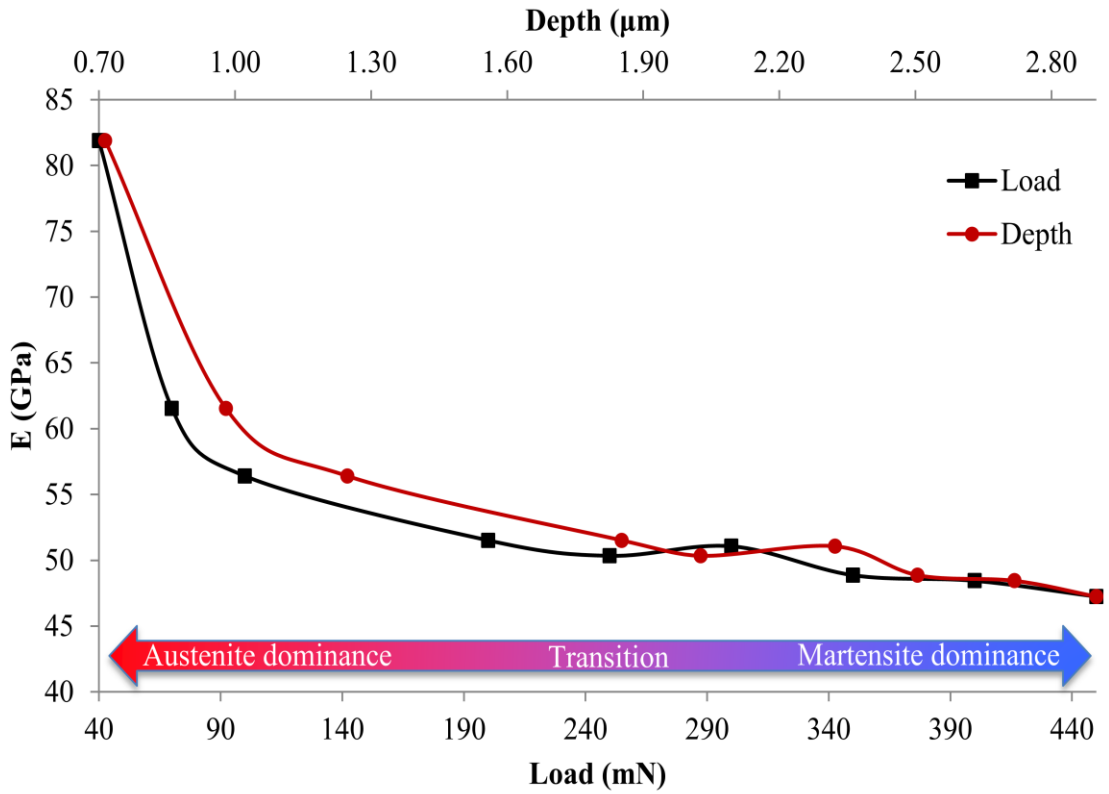

Figure 4.30 Elastic modulus versus normal load

4.3 Tribological Behavior

Reciprocating wear tests were performed under varying normal loads, frequencies and time intervals to understand the wear behavior of equiatomic TiNi and aged, annealed, and solution treated 60NiTi. Morphologies of worn surfaces of superelastic TiNi after wear tests were analyzed using SEM and EDS.

Bodies in contact are controlled by many factors, including, load, sliding speed, surface film, temperature, humidity, hardness and work-hardening. A major factor that can be added to the above list, for superelastic shape memory alloys, is stress-induced martensitic phase transformation. During wear, load and thermal cycling in superelastic shape memory alloys give rise to microstructural changes as a result of martensite twinning, martensite detwinning and austenite-to-martensite and martensite-to-austenite phase transformations. These microstructural changes significantly affect wear and deformation behavior of superelastic TiNi.

The cumulative weight loss versus sliding distance data was plotted and representative curves are shown in Figure 4.31(a-d). Weight loss as a function of sliding distance curves are characterized by two wear regimes. Initially the wear rate, i.e., slope of the curve, is high but after a short sliding distance, the slope decreases to a lower steady state value. The initial high wear rate region is believed to be due to a "break-in" period. This break-in region corresponds to a similar rise in the coefficient of friction, as will be seen in Figure 4.35. The figure also shows that the weight loss increases with the increase in applied normal load for a constant reciprocating frequency of 10 Hz. This behavior is also evident from the incremental weight loss versus sliding distance curves in Figure 4.32(a-d). Here, weight loss was measured at equal sliding distance intervals. These curves are characterized by rapid increase in weight loss up to a sliding distance of 200 m, believed to be due to break-in. The high incremental weight loss is followed by a drop to a steady state value. During this period, hard asperities of the WC ball plough through the softer TiNi surface and gradually remove TiNi asperities by polishing action accompanied by a drop in incremental weight loss. Under the applied loads employed in this work, as soon as the WC counterface ball comes in contact with the TiNi surface and sliding begins, it deforms the specimen surface and alters its roughness. This behavior is reflected by the initial high wear rate and high coefficient of friction associated with a "break-in" period. Surface roughness was measured and the average surface roughness of polished surface of equiatomicTiNi pre-testing was found to be 75 nm, while surface roughness of TiNi after only 2 wear cycles was 3184 nm. Topographical and microstructural evolution during the break-in period leads to a transition from severe to mild wear, where more stable intimate contact between surfaces exists.

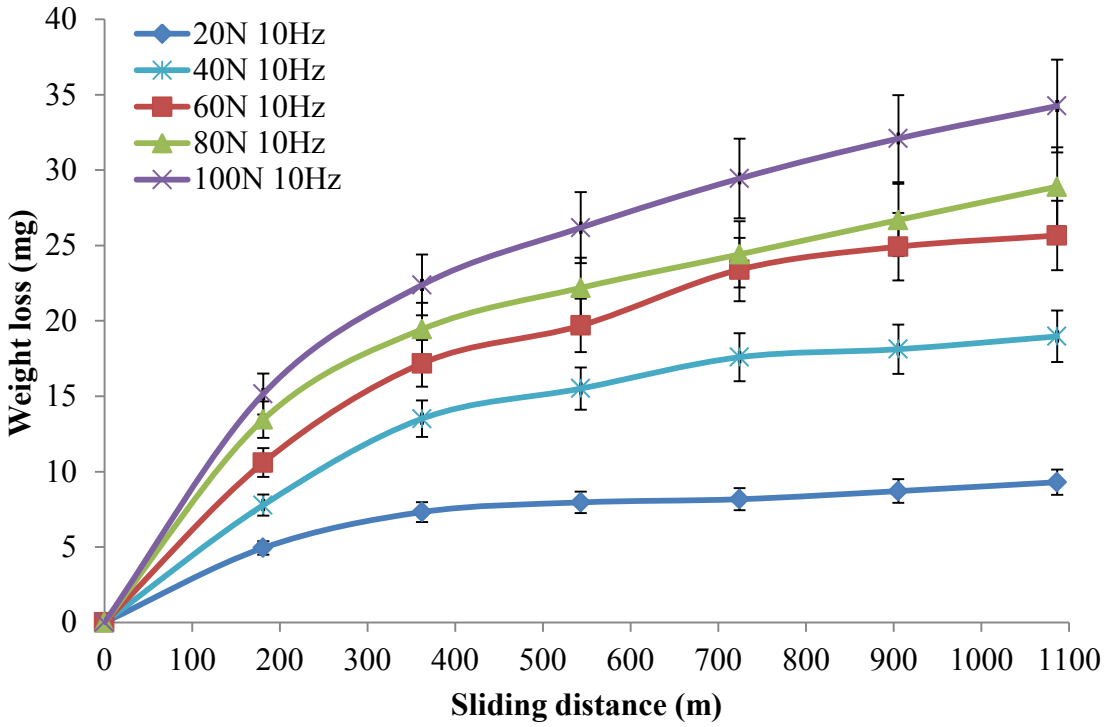
20N 10Hz
40N 10Hz
60N 10Hz
80N 10Hz
100N 10Hz
Weight loss (mg)
Sliding distance (m)
0
5
10
15
20
25
30
35
40
0
100
200
300
400
500
600
700
800
900
1000
1100

(a)

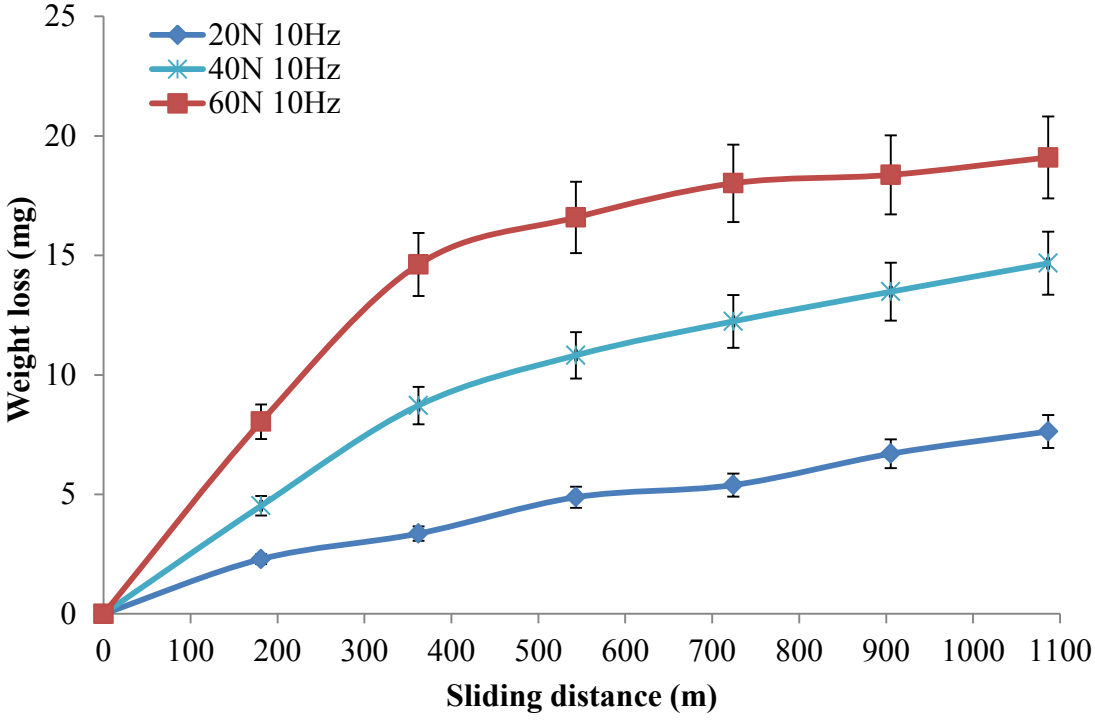
20N 10Hz
40N 10Hz
60N 10Hz
Weight loss (mg)
Sliding distance (m)
0
5
10
15
20
25
0
100
200
300
400
500
600
700
800
900
1000
1100

(b)

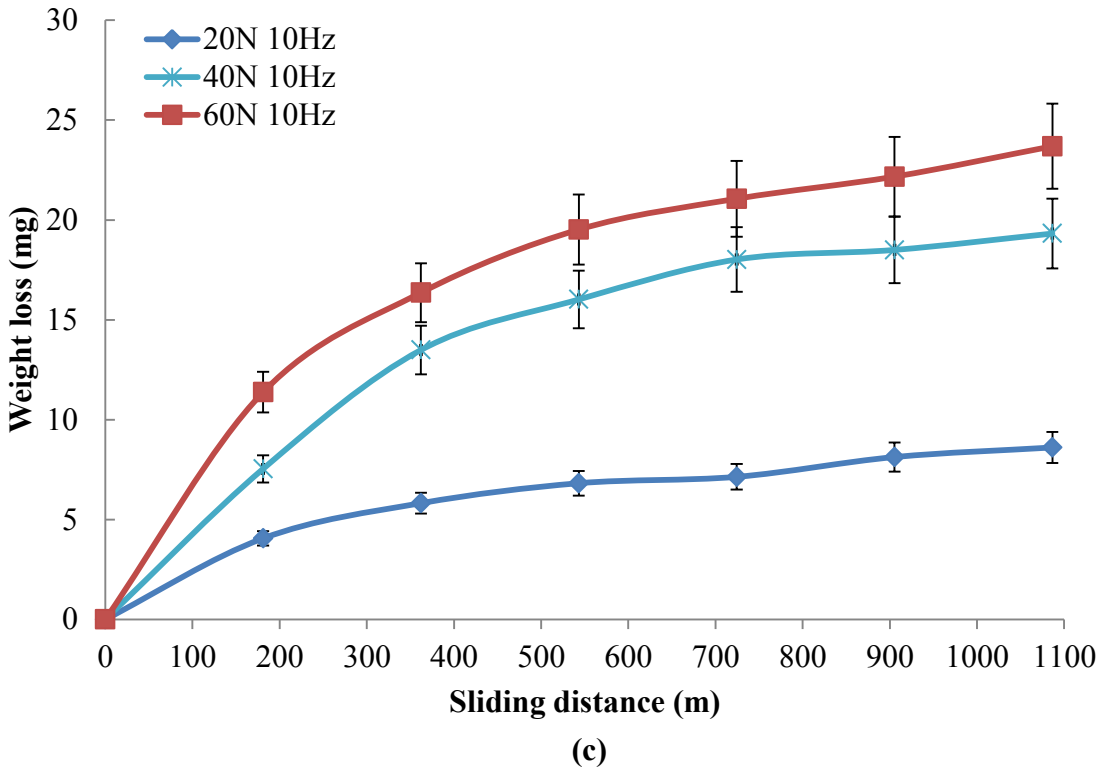

(c)

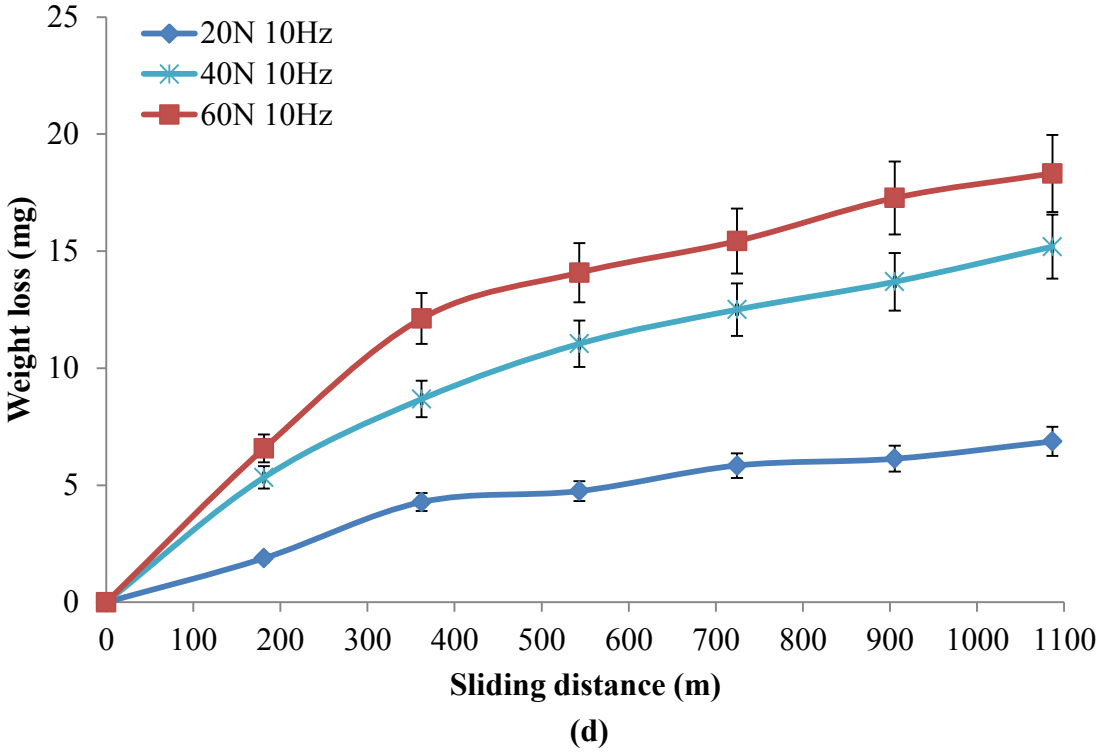

(d)

Figure 4.31 Cumulative weight loss versus sliding distance for different loads: (a) equiatomic TiNi, (b) aged 60NiTi, (c) annealed 60NiTi, (d) solution treated 60NiTi

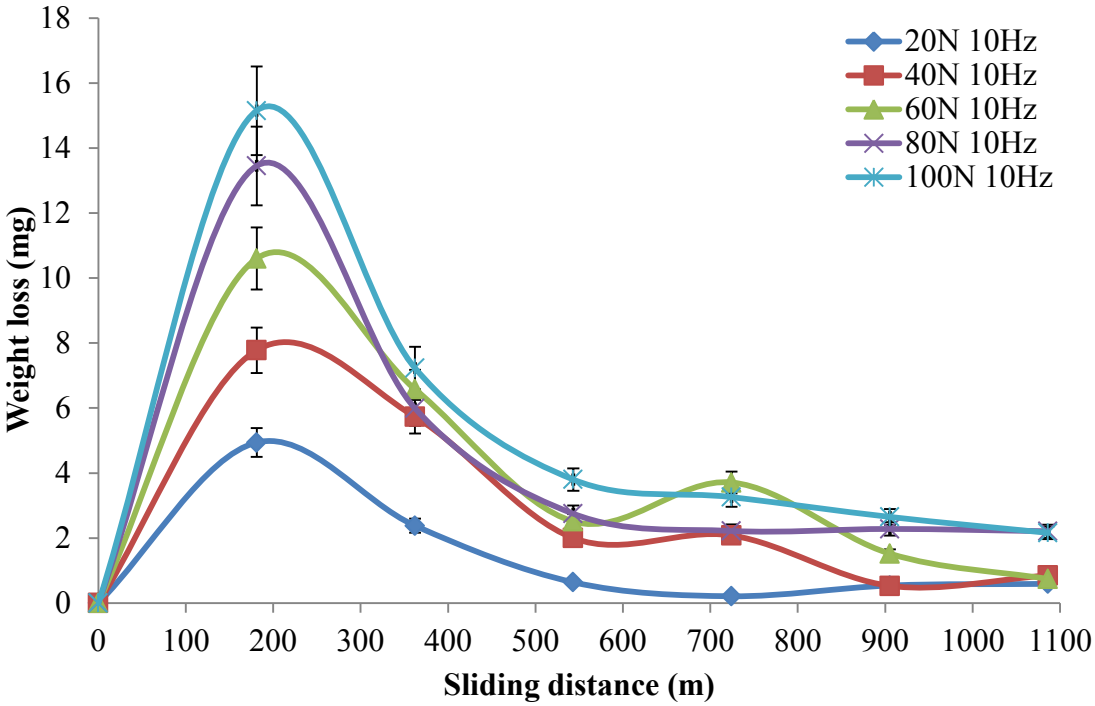
Weight loss (mg)
Sliding distance (m)
20N 10Hz
40N 10Hz
60N 10Hz
80N 10Hz
100N 10Hz
0
2
4
6
8
10
12
14
16
18
0
100
200
300
400
500
600
700
800
900
1000
1100

(a)

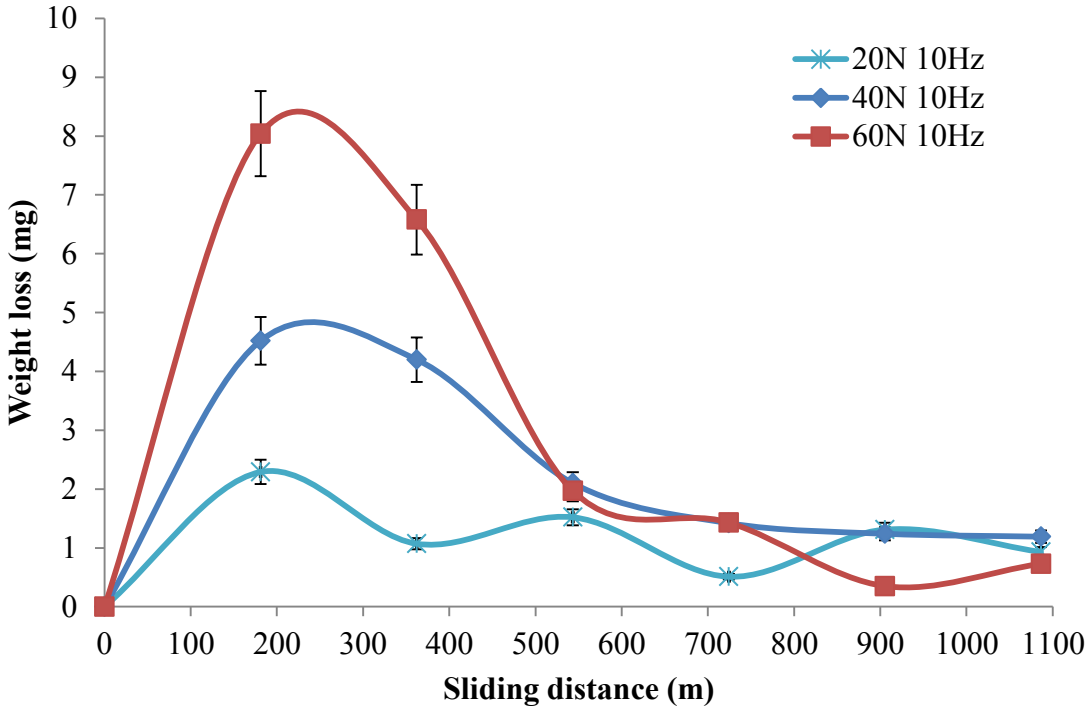
Weight loss (mg)
Sliding distance (m)
20N 10Hz
40N 10Hz
60N 10Hz
0
1
2
3
4
5
6
7
8
9
10
0
100
200
300
400
500
600
700
800
900
1000
1100

(b)

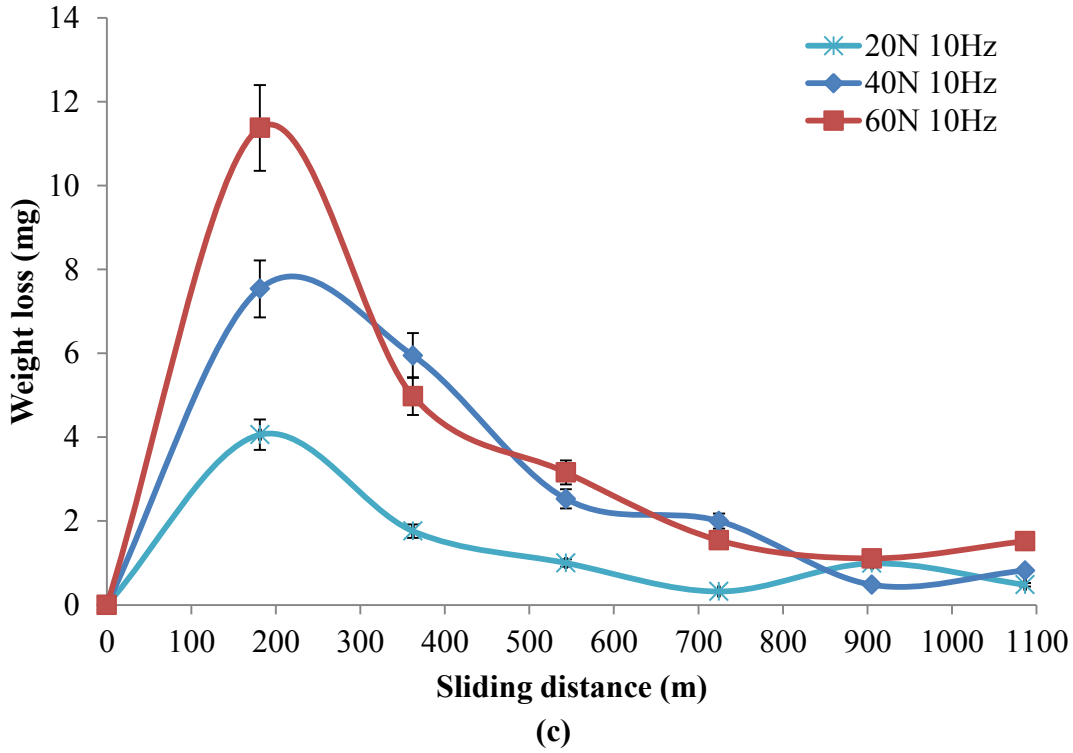

(c)

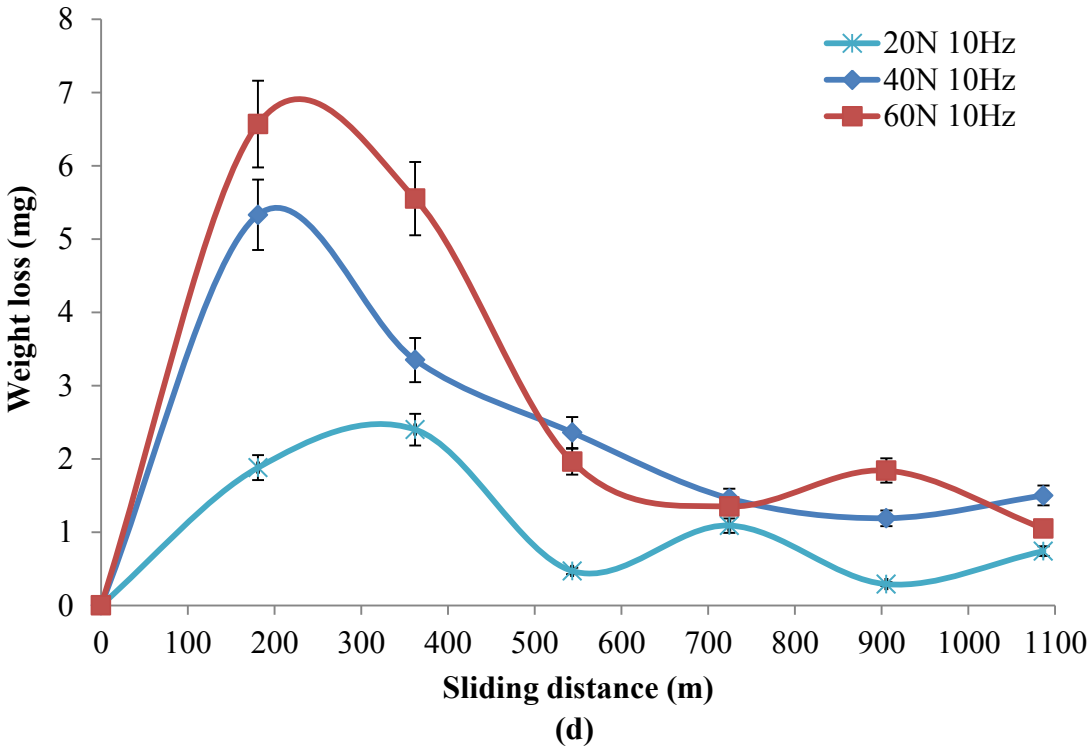

(d)

Figure 4.32 Incremental weight loss versus sliding distance for different loads: (a) equiatomic TiNi, (b) aged 60NiTi, (c) annealed 60NiTi, (d) solution treated 60NiTi

4.3.1 Effect of Normal Load and Frequency

As shown in Figure 4.31(a-d), the weight loss increases with the increase in applied normal load for a constant reciprocating frequency of 10 Hz for superelastic equiatomic TiNi, aged 60NiTi, annealed 60NiTi and solution treated 60NiTi. This behavior is attributed to the fact that higher applied normal loads promote higher levels of deformation leading to higher material removal rate. Similar behavior was observed with reciprocating frequencies of 5, 15 and 20 Hz. This increase in weight loss with the increase in applied load is also clear from incremental weight loss versus sliding distance curves as shown in Figure 4.32(a-d).

Steady state wear rates were calculated from the corresponding slope of the steady-state region in the weight loss versus sliding distance curves (Figure 4.31(a-d)). The variation of wear rate as a function of normal load and frequency is given in Figure 4.33(a-d). Each data point in Figure 4.33 represents the steady-state wear rate for a given frequency and normal load. The figures show that the normal load and frequency have significant influence on wear resistance. It is suspected that the wear rate in Figure 4.33 is controlled by several effects operating simultaneously. The first effect is due to softening of the alloys at high frequency as a result of heating, and ultimately leading to higher wear rate. The second effect is due to rise in the austenite-to-martensite transition stress with temperature (Otsuka & Shimizu, 1986), which leads to increased wear resistance. The last effect is believed to be due to strain rate (frequency) response. This effect leads to a drop in wear rate with frequency, analogous to what has been established, in a previous work (Farhat, Jarjoura, & Shahirnia, 2013) that deformation resistance increases with strain rate for TiNi. The above mentioned effects operate simultaneously and produce the observed wear rate. A drop in wear rate is clearly seen in Figure 4.33 for all normal loads and in the frequency range 5 to 15 Hz, where it is believed that the second and third mechanisms discussed above are dominant. However, when the frequency is raised over 15 Hz, for a normal load up to 60N, the softening effect due to heating seems to be more dominant. This behavior is not observed for normal loads higher than 60N (Figure 4.33(a)). For 80 and 100N normal loads, the wear rate continues to drop, where the hardening effect is more dominant (Figure 4.33(a)). It is suspected that at higher loads of 80 and 100N the extent of martensite stabilization and martensite work hardening

increase. The schematic diagram in Figure 4.34 summarizes regions of dominant effects for TiNi and 60NiTi as a function of normal load and reciprocating frequency.

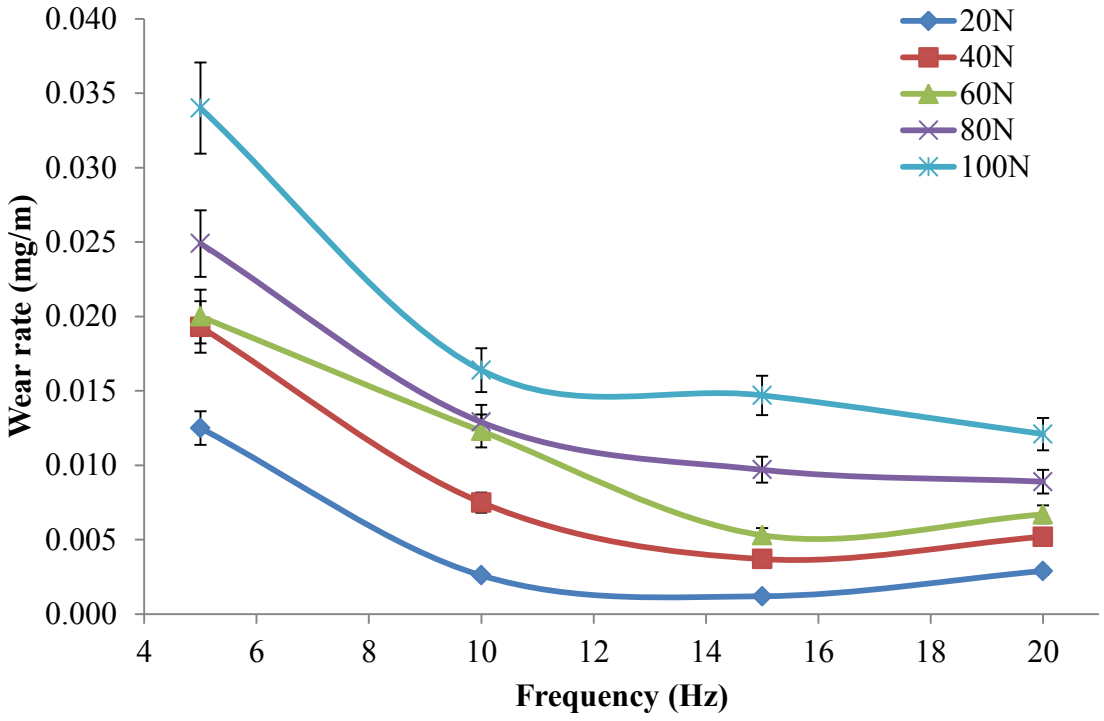

(a)

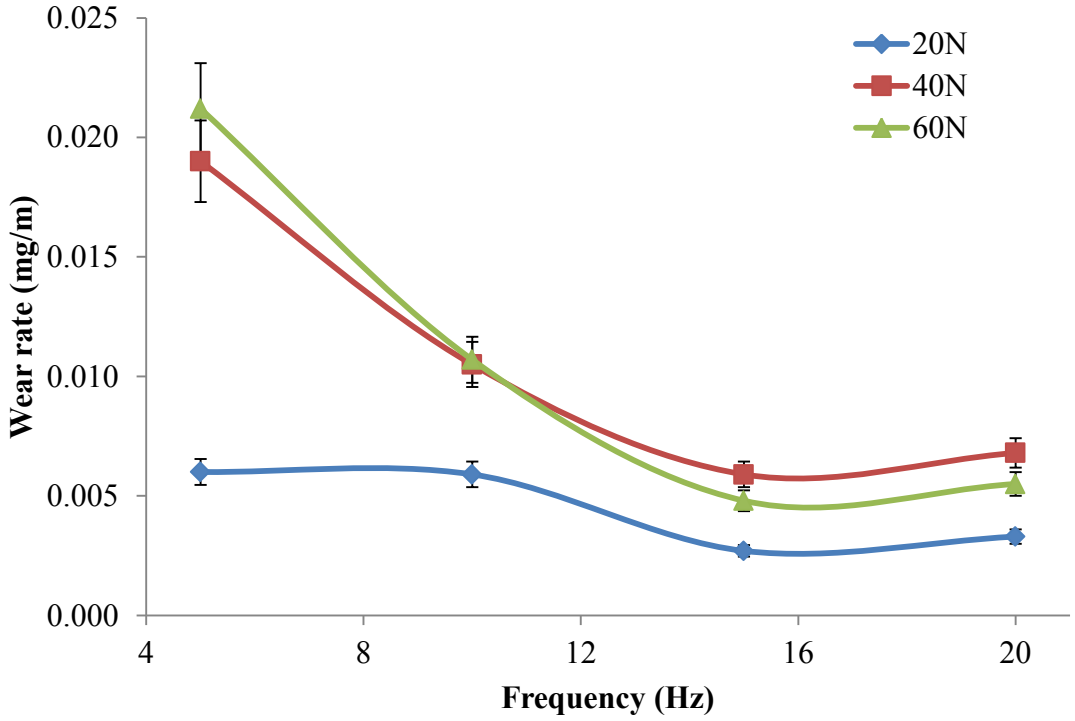

(b)

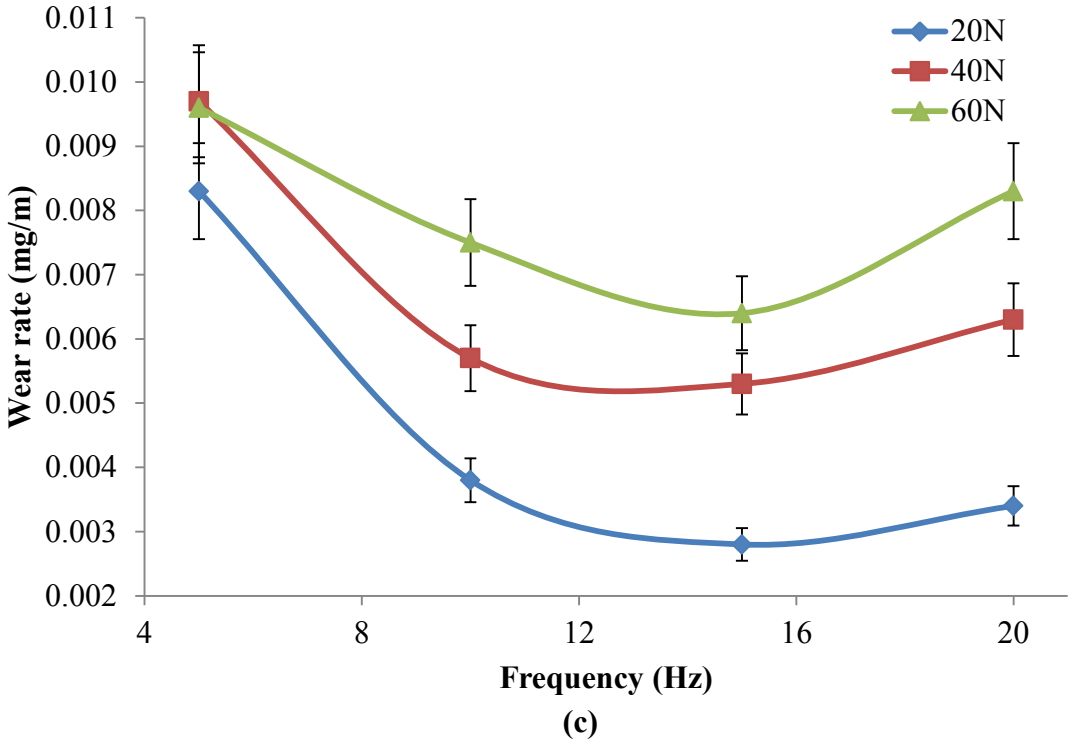

(c)

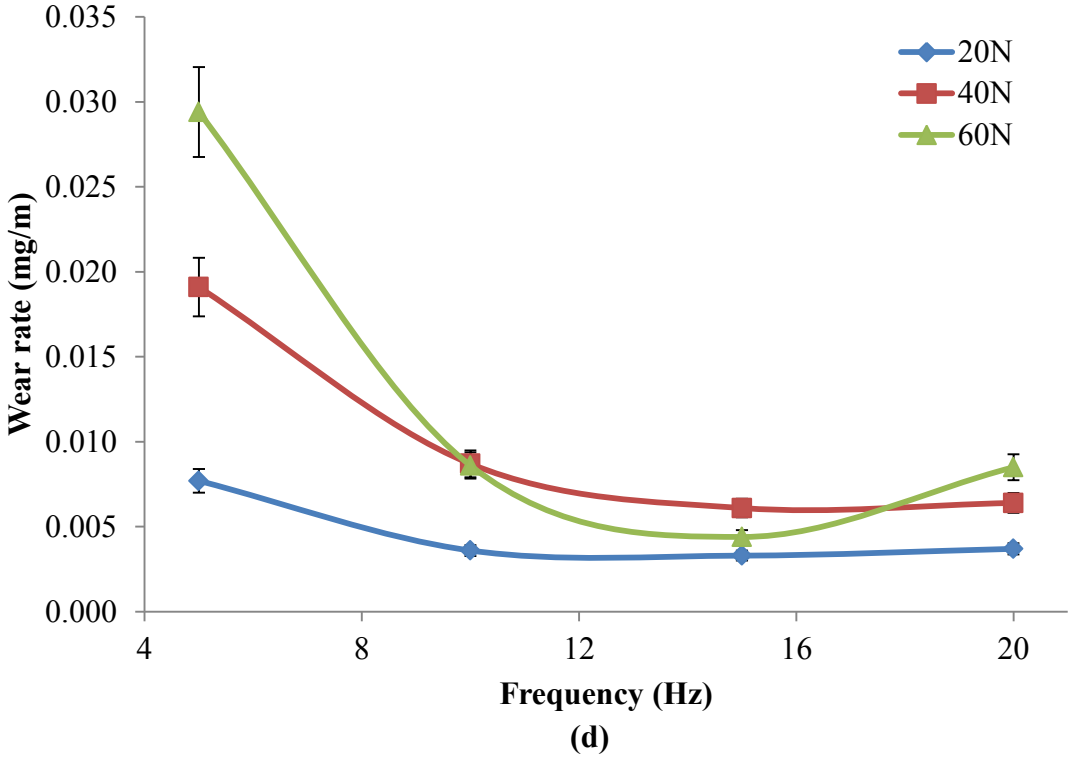

(d)

Figure 4.33 Steady state wear rate as a function of frequency: (a) equiatomic TiNi, (b) aged 60NiTi, (c) annealed 60NiTi, (d) solution treated 60NiTi

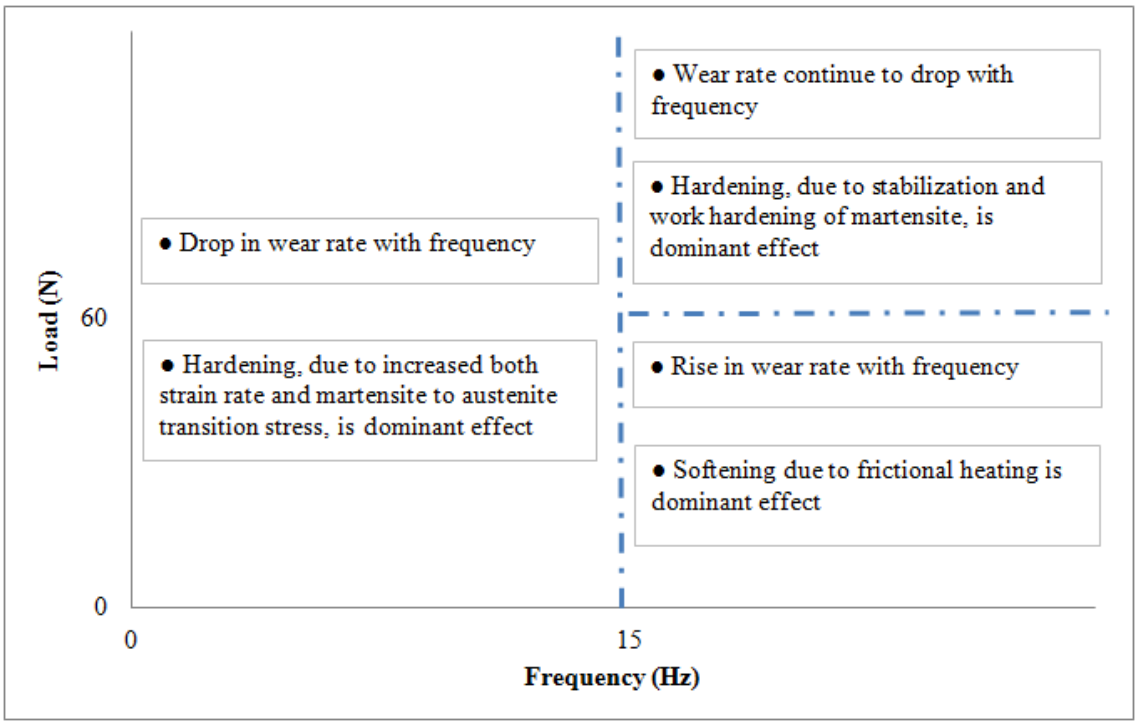

Figure 4.34 Summary of dominating effects as a function of frequency and load during wear of TiNi

4.3.2 Coefficient of Friction

During the reciprocating wear tests, the instantaneous values of calibrated normal force (Fz) and tangential force (Fx) were measured and continuously recorded using a data acquisition system. The acquisition system automatically computes the variation of the coefficient of friction (COF = Fx/Fz) with time. The COF was monitored during the reciprocating wear tests. The COF is plotted as a function of sliding distance for different loads and frequencies. Representative curves of equiatomic TiNi, aged 60NiTi, annealed 60NiTi, and solution treated 60NiTi are shown in Figure 4.35(a-d). The basic shape of the friction curve remains similar under all testing conditions. Each curve is characterized by two friction regimes. Initially, the coefficient of friction increases until it reaches a maximum steady-state value. The COF becomes independent of sliding distance at steady-state. The initial rise in the coefficient of friction is attributed to a "break-in" period which corresponds to similar transition in wear behavior.

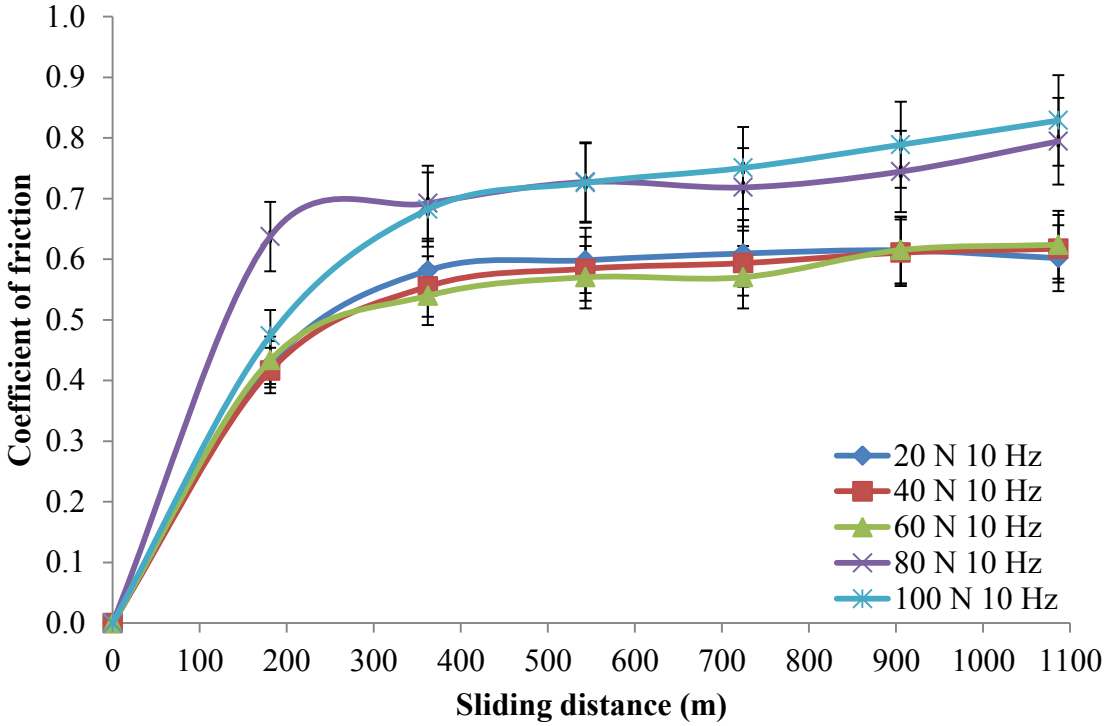
1.0
0.9
0.8
0.7
0.6
0.5
0.4
0.3
0.2
0.1
0.0
Coefficient of friction
0
100
200
300
400
500
600
700
800
900
1000
1100
Sliding distance (m)
20 N 10 Hz
40 N 10 Hz
60 N 10 Hz
80 N 10 Hz
100 N 10 Hz

(a)

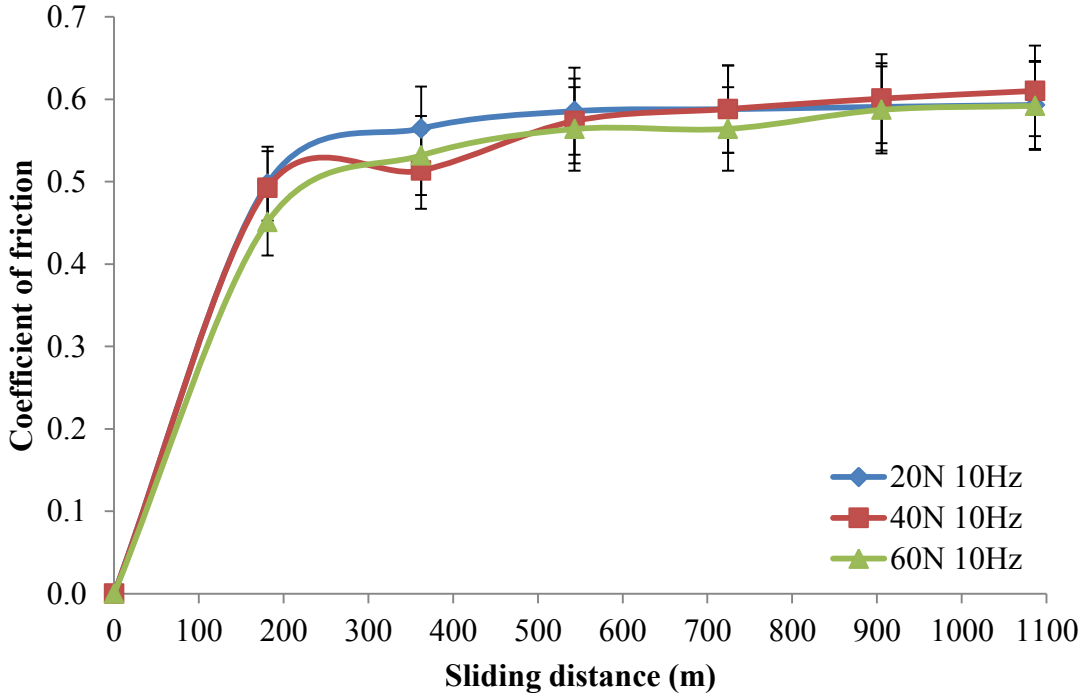
0.7
0.6
0.5
0.4
0.3
0.2
0.1
0.0
Coefficient of friction
0
100
200
300
400
500
600
700
800
900
1000
1100
Sliding distance (m)
20N 10Hz
40N 10Hz
60N 10Hz

(b)

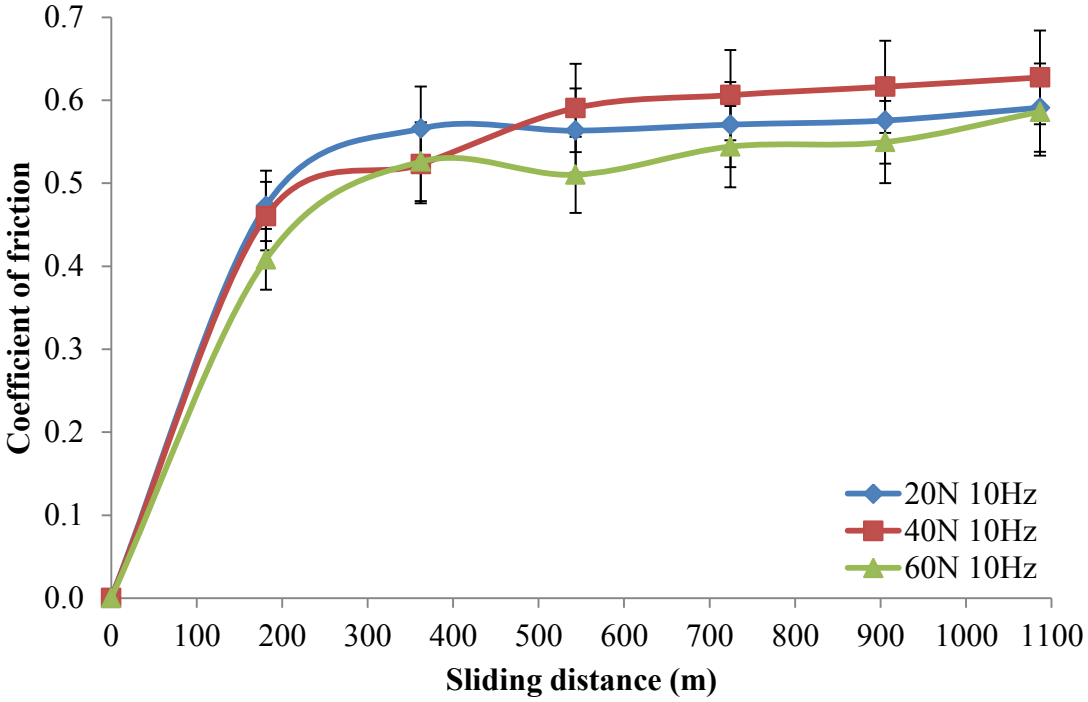

(c)

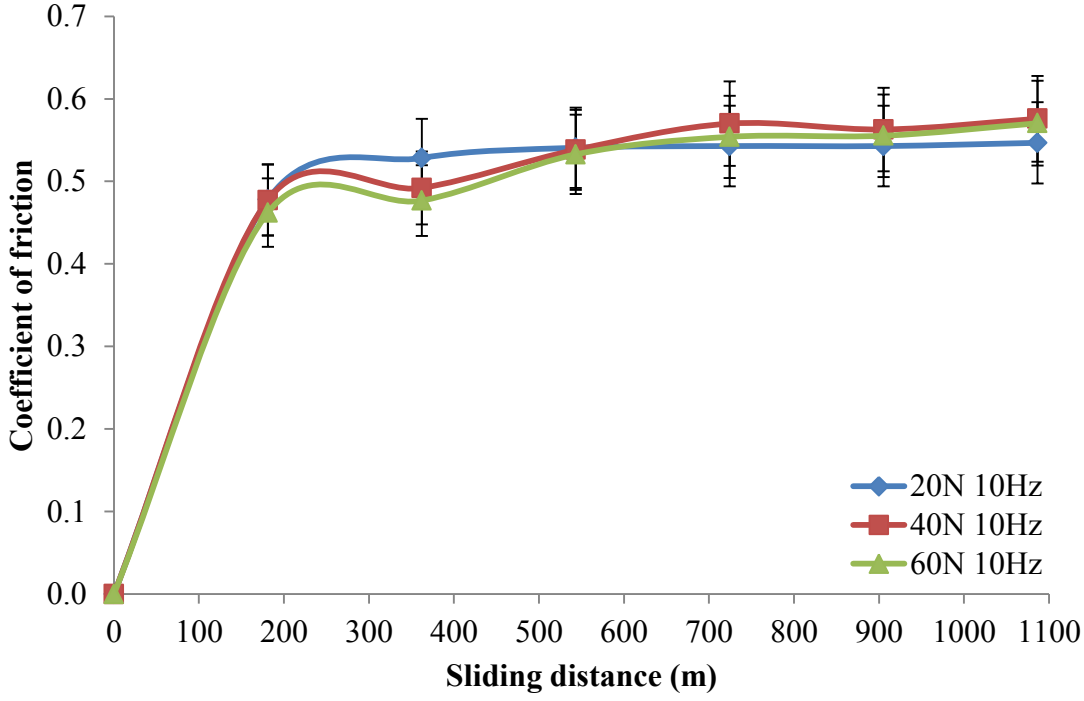

(d)

Figure 4.35 Coefficient of friction versus sliding distance for different loads: (a) equiatomic TiNi, (b) aged 60NiTi, (c) annealed 60NiTi, (d) solution treated 60NiTi

Furthermore, Figure 4.36(a-d) shows the steady-state coefficient of friction as a function of frequency for different normal loads for equiatomic TiNi and 60NiTi (aged, annealed and solution treated). According to this diagram, the COF drops as the reciprocating frequency rises for all the employed normal loads. It is well established that the COF is controlled by both surface and bulk properties in accordance with the general rule (Larsen-Basse, 1992):

$$COF=\tau_s / H_b \qquad \text{Equation 4.10}$$

where, τ_s is surface shear strength and H_b is the bulk hardness. It can be argued that the drop in coefficient of friction with frequency is dominated by surface softening due to heating, which gives rise to a corresponding drop in surface shear strength. Hence, the COF seems to vary only with heating effects.

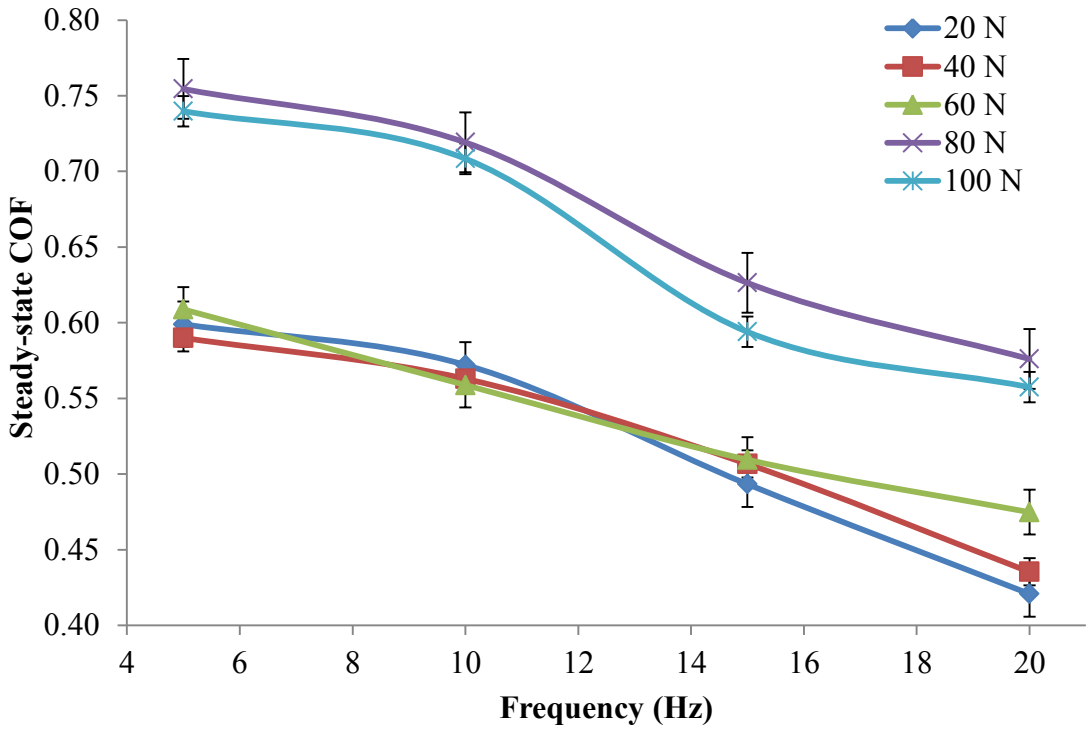

(a)

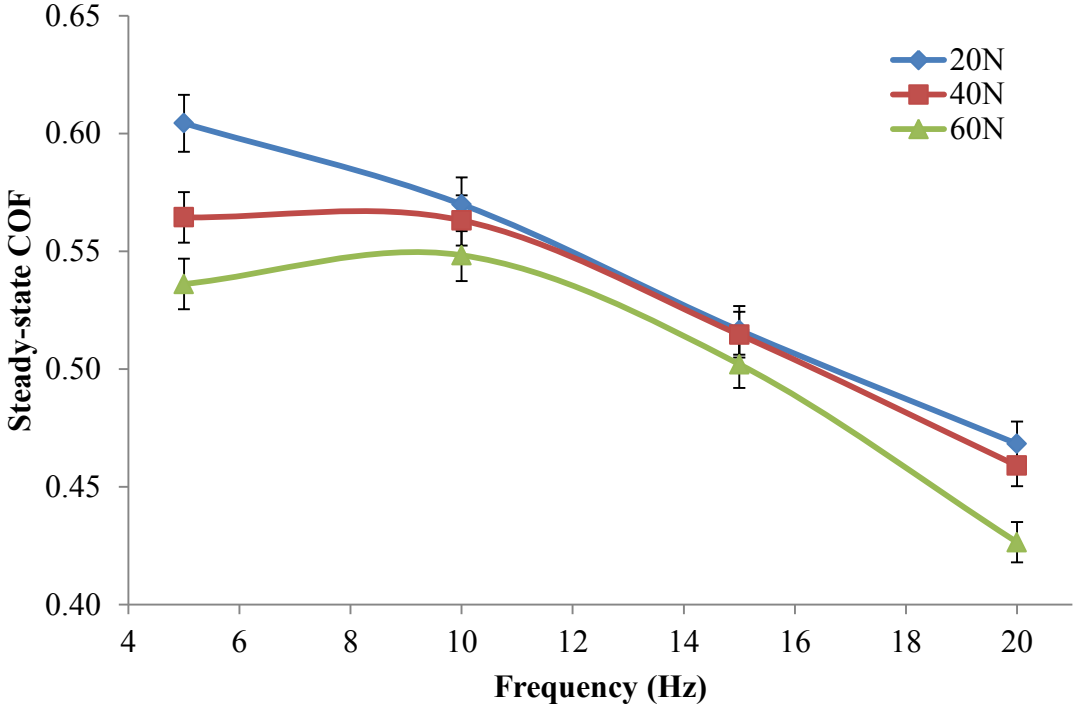
0.65
0.60
0.55
0.50
0.45
0.40
Steady-state COF
4
6
8
10
12
14
16
18
20
Frequency (Hz)
20N
40N
60N

(b)

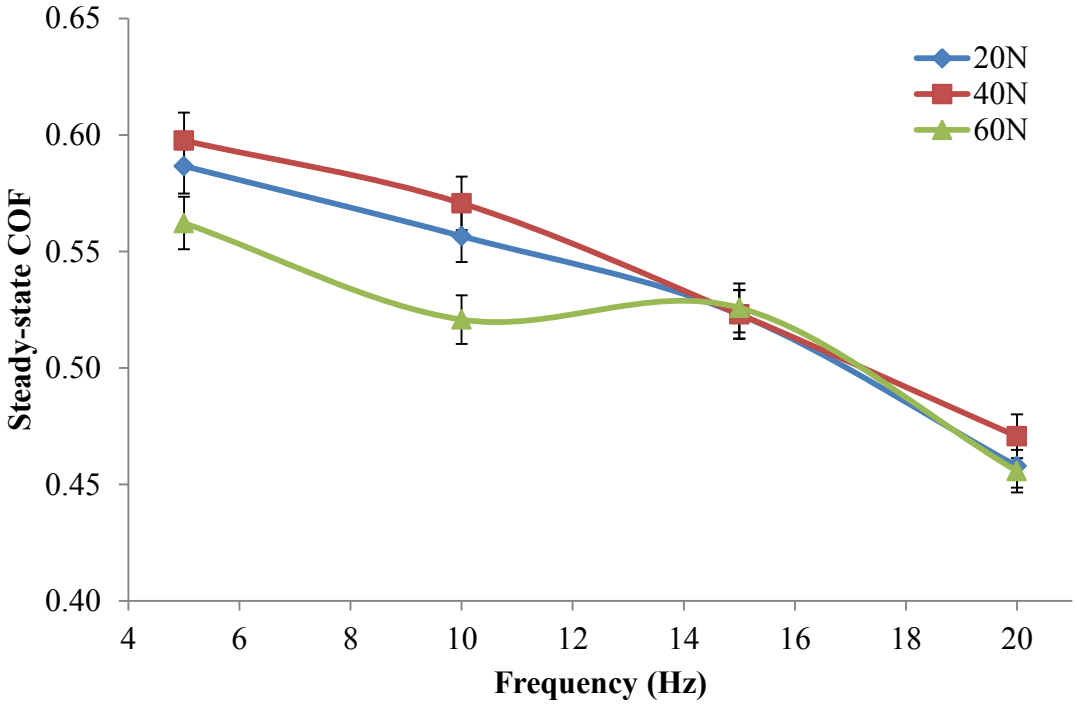
0.65
0.60
0.55
0.50
0.45
0.40
Steady-state COF
4
6
8
10
12
14
16
18
20
Frequency (Hz)
20N
40N
60N

(c)

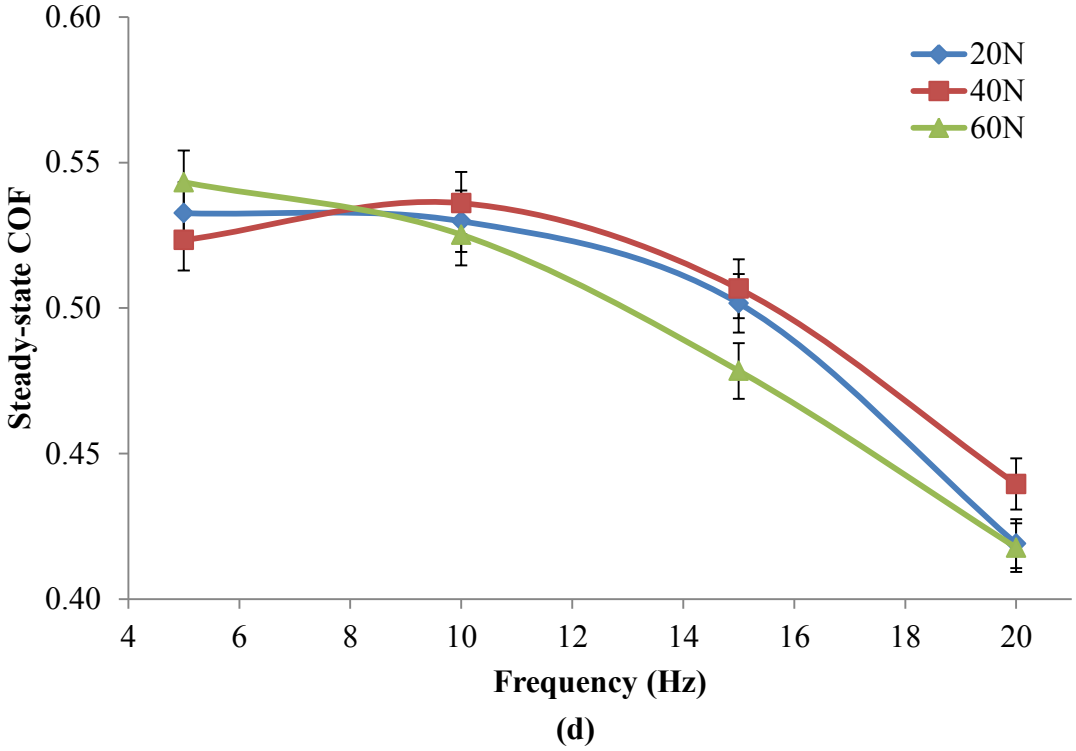

(d)

Figure 4.36 Coefficient of friction versus frequency for different normal loads: (a) equiatomic TiNi, (b) aged 60NiTi, (c) annealed 60NiTi, (d) solution treated 60NiTi

In order to assess the effect of load on COF, the COF is plotted as a function of normal load for different frequencies and is given in Figure 4.37(a-d). It is found that as the normal load is raised, no significant change in the COF is observed up to a normal load of 60N for equiatomic TiNi and 60NiTi (aged, annealed and solution treated) as clearly seen in Figure 4.37(a-d). However, a sharp rise in the steady state COF is detected as the normal load increases from 60 to 80N for equiatomicTiNi and remains essentially constant afterwards. At high loads superelasticity is no longer operative on and near the surface and the increase in the coefficient of friction is attributed to martensite stabilization and work hardening, this gives rise to high surface shear strength. Also, the presence of hard oxides gives rise to higher surface shear strength and limits contact between TiNi and WC ball surface which reduce weight loss, i.e. low wear rate.

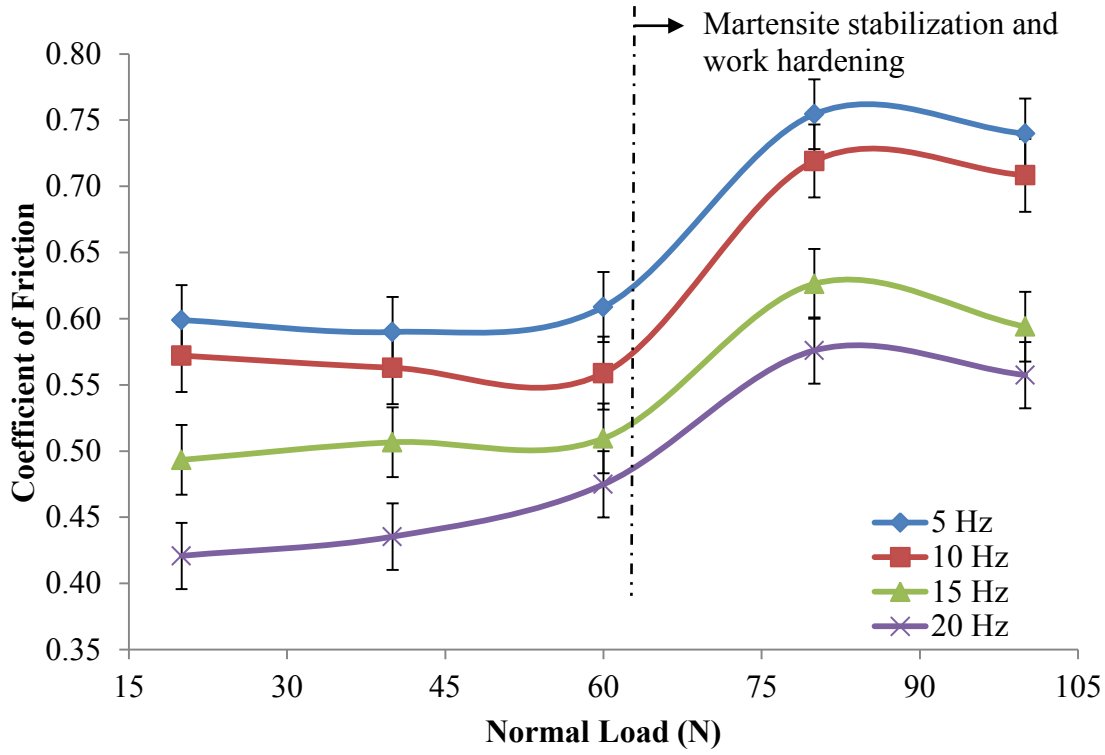
Martensite stabilization and work hardening
Coefficient of Friction
0.80
0.75
0.70
0.65
0.60
0.55
0.50
0.45
0.40
0.35
15
30
45
60
75
90
105
Normal Load (N)
5 Hz
10 Hz
15 Hz
20 Hz

(a)

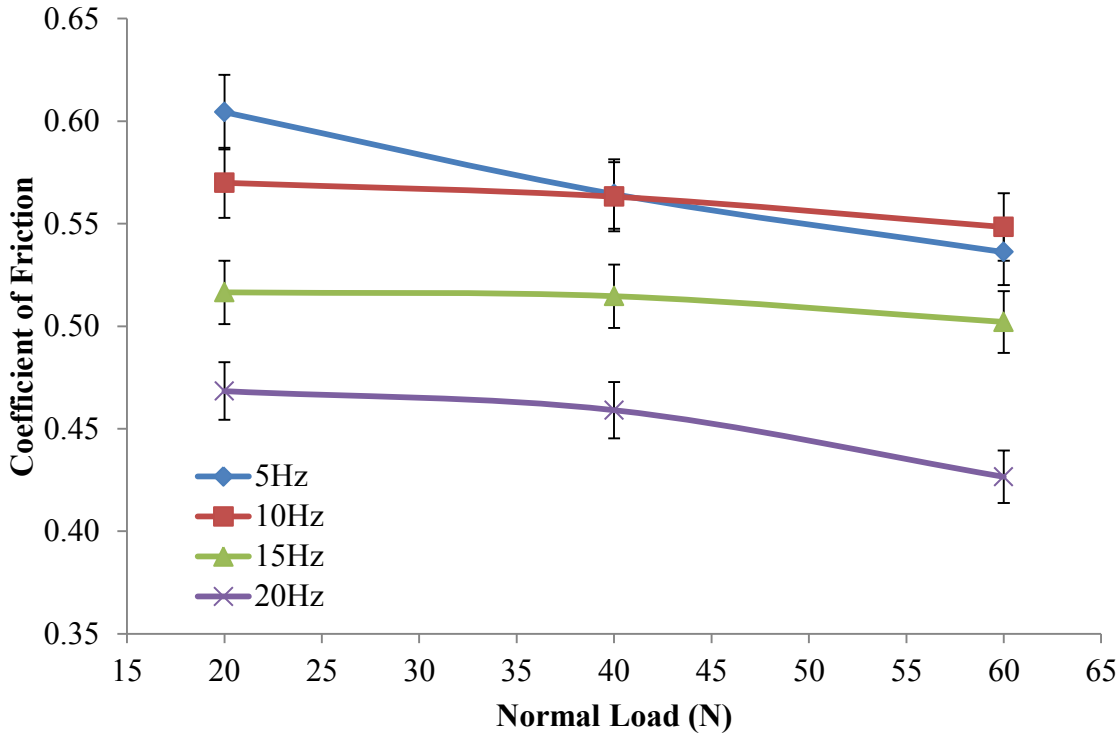
Coefficient of Friction
0.65
0.60
0.55
0.50
0.45
0.40
0.35
15
20
25
30
35
40
45
50
55
60
65
Normal Load (N)
5Hz
10Hz
15Hz
20Hz

(b)

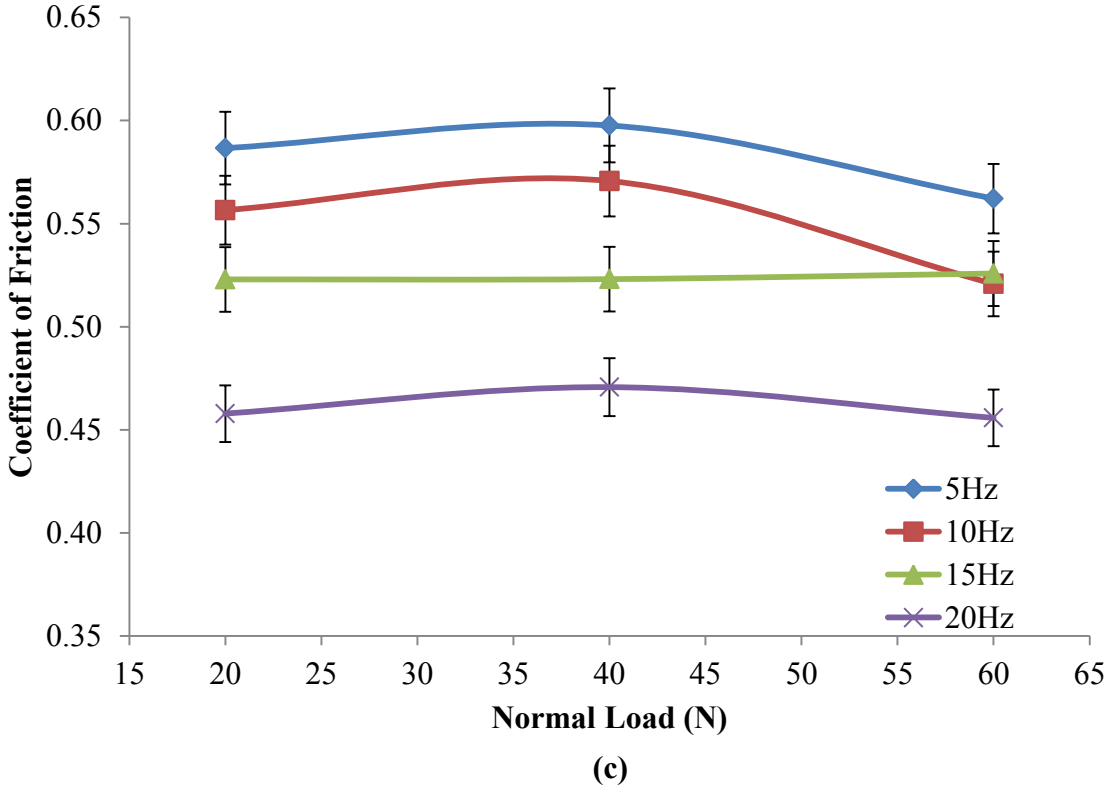

(c)

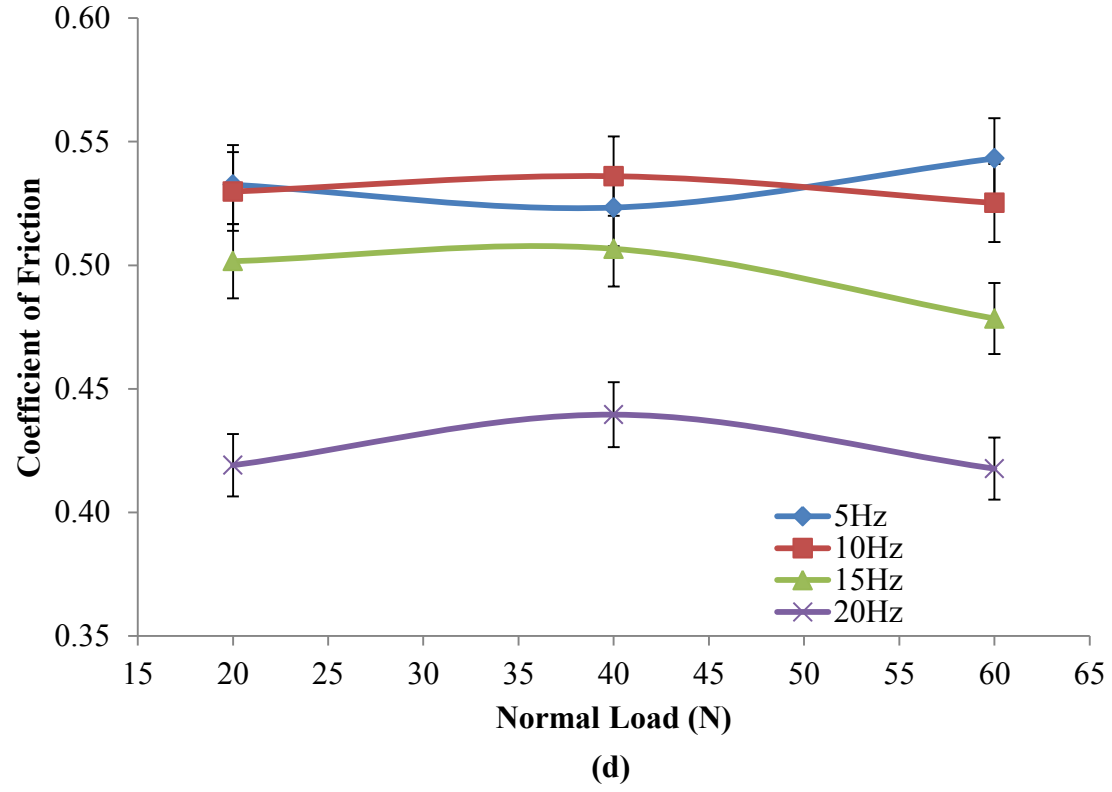

(d)

Figure 4.37 Coefficient of friction versus normal load for different frequencies: (a) equiatomic TiNi, (b) aged 60NiTi, (c) annealed 60NiTi, (d) solution treated 60NiTi

4.3.3 Specific Wear Rate

Wear data for equiatomic TiNi and 60NiTi (aged, annealed and solution treated) can be described by Archards-type law for sliding wear and the specific wear rate can be determined using Archard's equation, given below.

$V = kFs$ Equation 4.11

where, V is wear volume, k is specific wear rate, F is normal load, and s is sliding distance. Wear volume is calculated by dividing the measured weight loss by density of TiNi (6.45 g/cc) and 60NiTi (6.7 g/cc). Table 4.4 summarizes the properties of equiatomic TiNi and 60NiTi (aged, annealed and solution treated). Examination of Table 4.4 show that the coefficients of friction of aged, annealed and solution treated 60NiTi are slightly lower than that of equiatomic TiNi. Wear data given in Table 4.4 show that, based on specific wear rates, aged and solution treated 60NiTi exhibit 40% improvement in wear resistance over equiatomic TiNi. This enhancement in wear resistance is due to the higher hardness of aged and solution treated 60NiTi compared to equiatomic TiNi (see Table 4.1). The specific wear rates for TiNi and 60NiTi reported in Table 4.4 are lower than those reported for many wear resistant materials (Ashby, 2005). Compared to medium carbon steel (10^{-4} mm^3/Nm), stainless steel (10^{-4} mm^3/Nm), high carbon and tool steels (range 10^{-4} mm^3/Nm to 10^{-5} mm^3/Nm) (Ashby, 2005), TiNi and 60NiTi exhibit lower specific wear rate. Moreover, compared to hardened AISI 52100 bearing steel having specific wear rate between $9.6X10^{-5}$ mm^3/Nm and $1.6X\ 10^{-4}$ mm^3/Nm (Sen & Sen, 2009), superelastic TiNi and 60NiTi show lower specific wear rate. Here, AISI 52100 bearing steel data was generated using ball-on-disc test, however, in the absence of data generated using reciprocating sliding wear, it is reasonable to state, based on the available data, that TiNi and 60NiTi exhibit superior wear resistance.

Table 4.4 Summary of properties of equiatomic TiNi and 60NiTi (aged, annealed and solution treated)

Materials	Specific wear rate (mm^3/Nm)	COF
Equiatomic TiNi	$10.86X10^{-5}$	0.53
Aged 60NiTi	$7.02X10^{-5}$	0.50
Annealed 60NiTi	$9.73X10^{-5}$	0.52
Solution treated 60NiTi	$6.66X10^{-5}$	0.49

4.4 Worn Surface Evaluation

TiNi wear tracks were scanned using optical profiler. Figure 4.38(a-b) shows an optical profiler scan of superelastic TiNi wear tracks subjected to 100N load and different frequencies at the end of the wear tests. The wear tracks reveal the increase in width and depth of the wear track with increase in reciporcating frequency (Figure 4.38(b)).

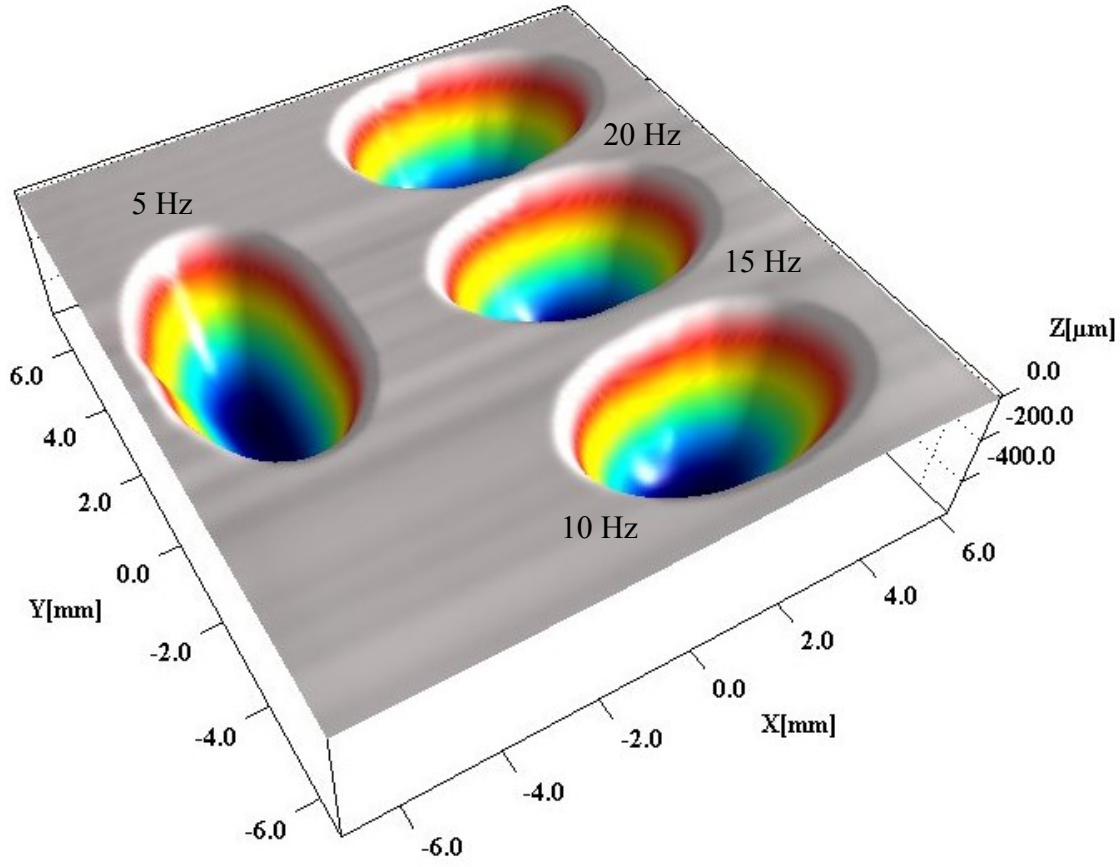

(a)

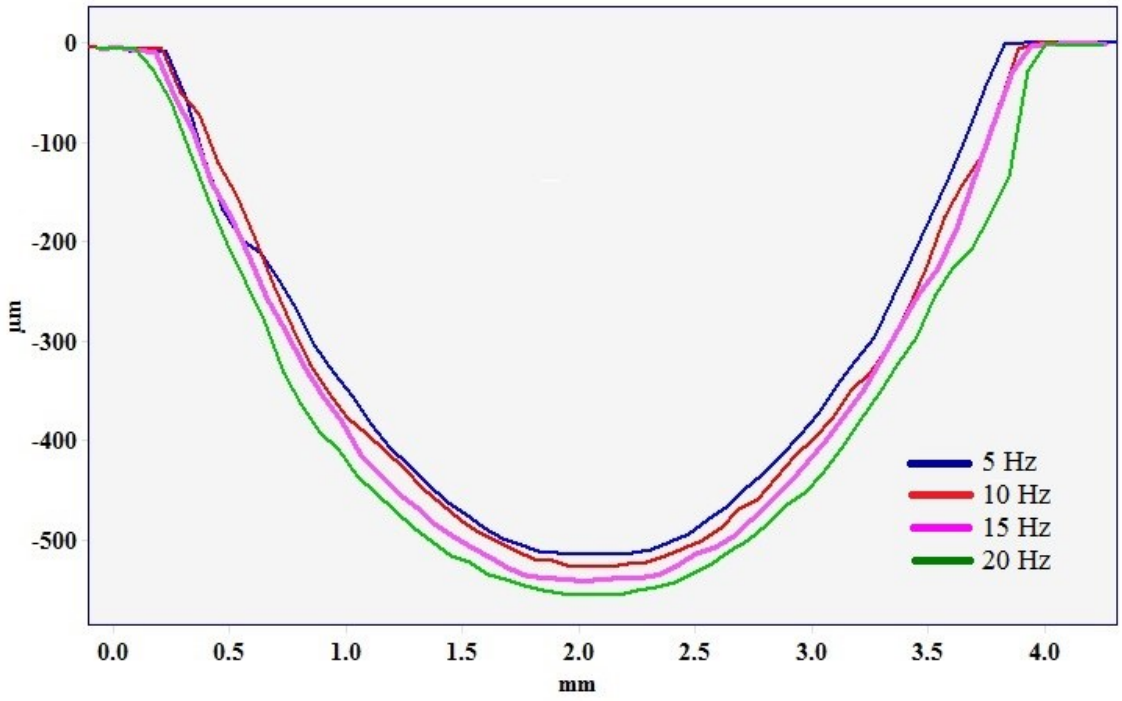

(b)

Figure 4.38 Profiler scan: (a) superelastic TiNi wear tracks under 100N load and different frequencies, (b) wear tracks width and depth profile

Microstructural analysis of wear tracks, wear debris, and tungsten carbide ball surface were investigated using scanning electron microscopy and electron dispersive spectroscopy. Examination of the tungsten carbide ball counter-face surface reveals clear evidence of adhesive wear. Adhesive wear occurs as a result of the formation of asperity junctions (cold weld) between the two surfaces in contact. This is followed by the shearing of the junction leaving material from one surface attached to the other surface. SEM micrograph and EDS results confirm the presence of TiNi layer on the WC ball surface as shown in Figure 4.39. As shown in Figure 4.39(b), there are Ti and Ni peaks appearing together with W, C, and Co.

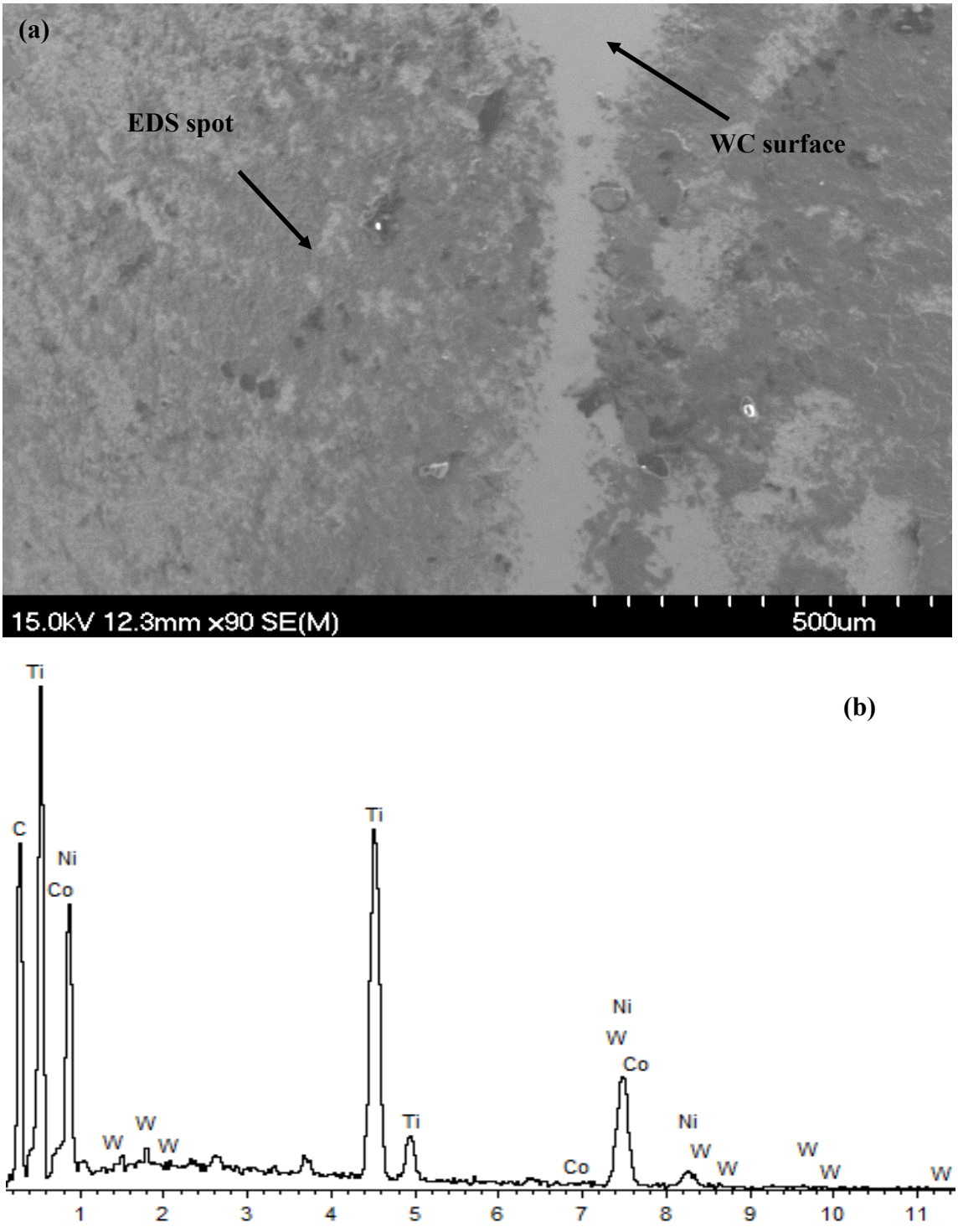

Figure 4.39 (a) SEM micrograph of WC ball showing TiNi transfer layer, (b) EDS analysis of the surface of WC ball

SEM examination of TiNi wear tracks subjected to 100 N load and 5 Hz reveal evidence of plastic flow of material in the sliding direction, deep grooves oriented along sliding direction and oxide formation on wear tracks as shown in Figure 4.40(a). The presence of grooves and ridges on the wear track are evidence of abrasive wear. The grooves are a result of ploughing action by the counter-face and/or loose wear debris as third party abrasion. The ridges that form around the grooves subsequently deform and fracture to generate wear debris. It is found that these series of parallel deep grooves are more prominent at high normal load i.e. 80N and 100N. This trend might be because the superelastic nature of TiNi is no longer operative and permanent deformation takes place as martensite becomes stabilized. EDS analysis of wear track after reciprocating wear tests revels oxide formation on wear track as shown in Figure 4.40(b).

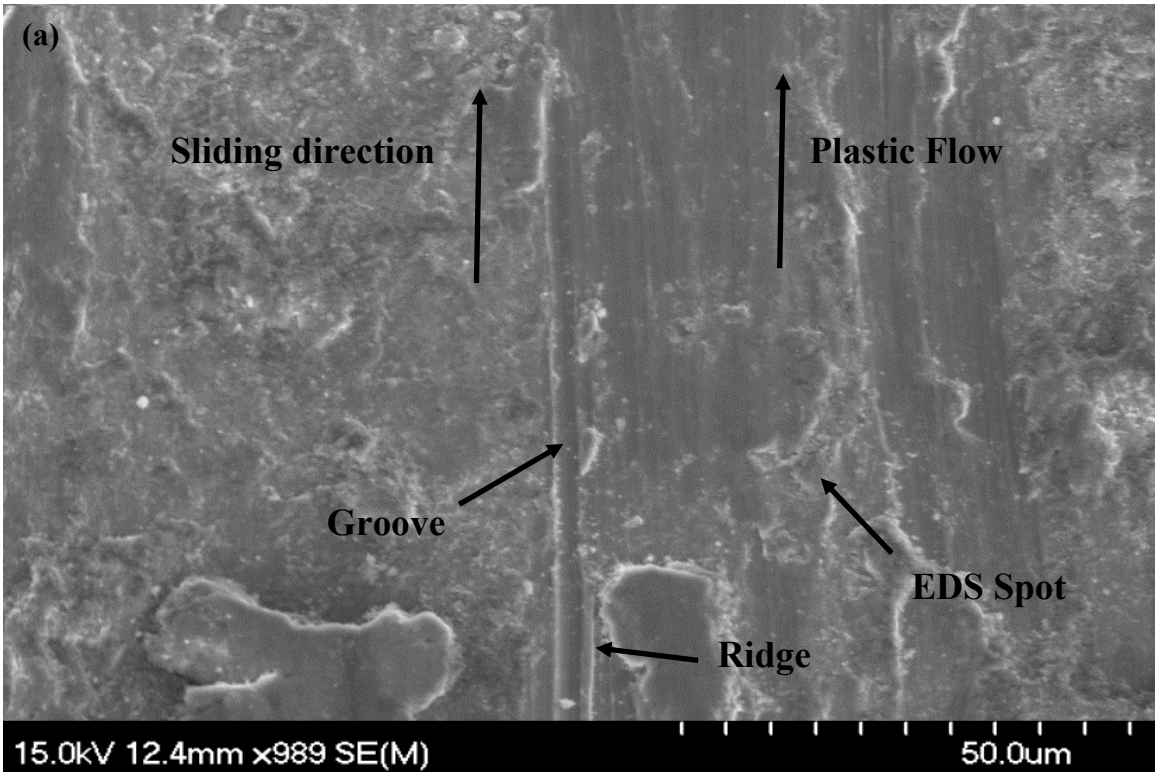

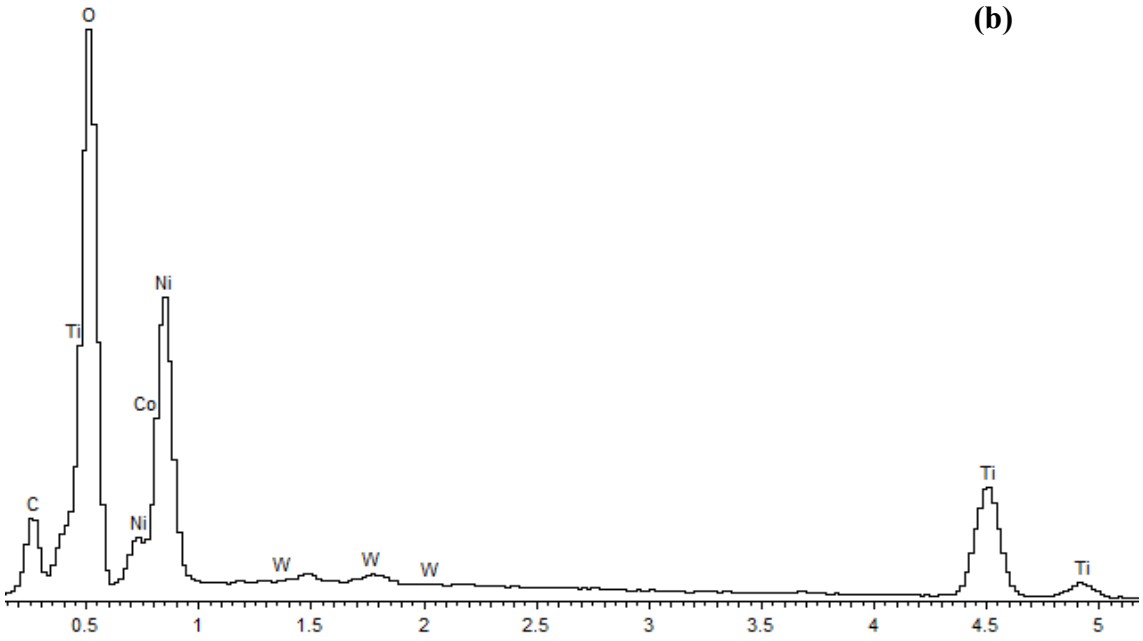

Figure 4.40 (a) SEM micrograph of TiNi wear track subjected to 100N load and 5 Hz frequency at the end of the wear test, (b) EDS analysis of wear track under 100N load and 5 Hz frequency

Delamination wear has been identified as another wear mechanism during reciprocating wear tests of superelastic TiNi. Delamination is more prominent at high normal loads. Delamination wear occurs due to heavy plastic deformation of the surface layers, nucleation of subsurface cracks, where shear stress is maximum, and propagation of these cracks parallel to the surface as a result, sheet-like wear particles are generated. Surface pits form as a result of delamination as shown in Figure 4.41. It is believed that delamination is promoted by the mismatch in the elastic properties of superelastic TiNi across the sample cross section. During reciprocating wear, the top surface of TiNi loses its superelastic property due to heavy plastic deformation, which cause martensite to stabilize; while, subsurface layers still behave in a superelastic manner. Hence, this mismatch in mechanical properties causes nucleation of cracks at the interface and propagation of these cracks parallel to the surface forming wear debris.

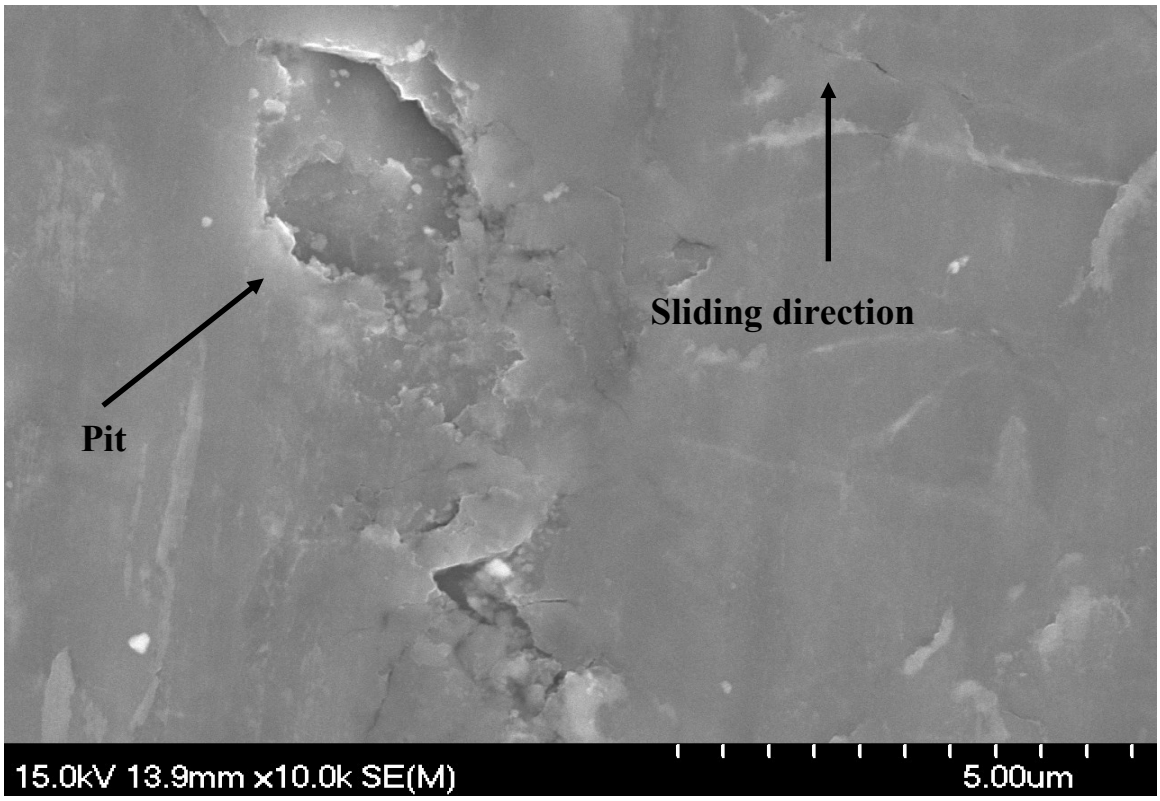

Figure 4.41 SEM micrograph of TiNi wear track subjected to 100N load and 5 Hz frequency at the end of the wear test showing pit formation post delamination

A high magnification image of the wear track after wear tests subjected to 60 N load and 20 Hz frequency shows extensive micro-cracks (Figure 4.42). Micro-cracks i.e., hertzian cracks, are developed due to surface tensile stress as a result of repeated sliding cycles and extend perpendicular to the sliding direction. It was found that micro-cracks are more prominent at high load.

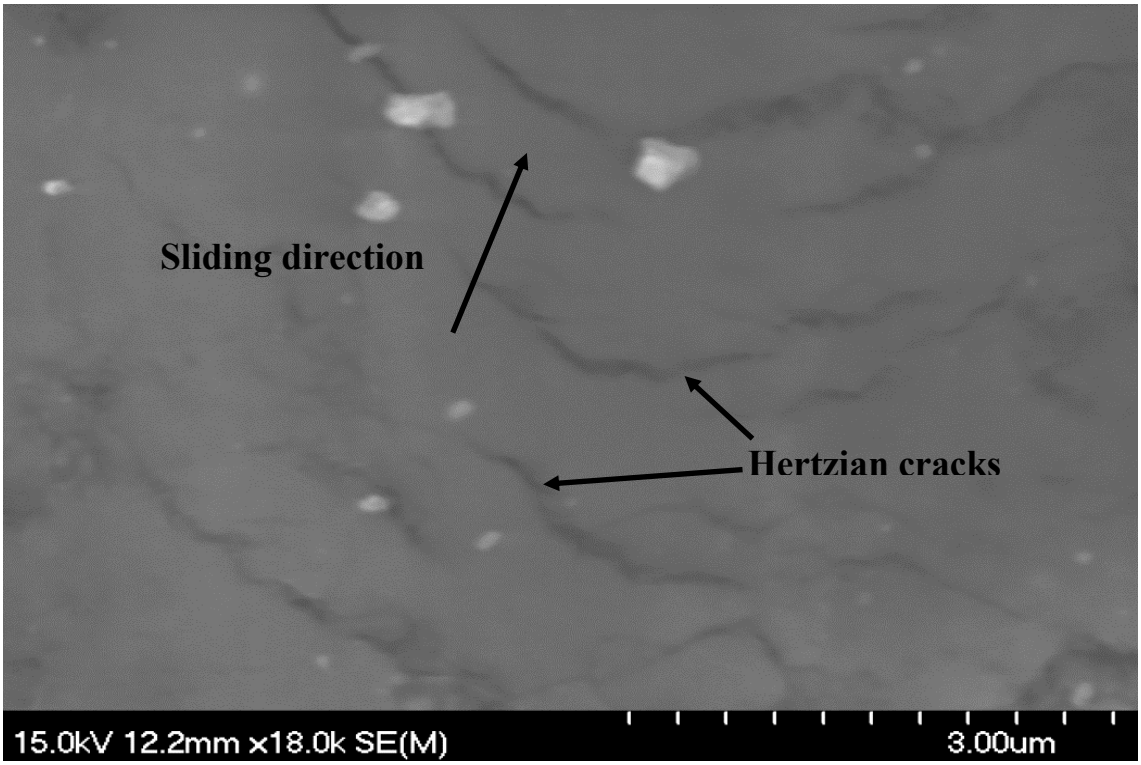

Figure 4.42 High magnification SEM micrograph of TiNi wear subjected to 60 N load and 20 Hz frequeny

SEM analysis of wear debris in Figure 4.43(a-d) reveal wear particles of superelastic TiNi after reciprocating wear tests subjected to 100 N load and 5, 10, 15 and 20 Hz frequency, respectively. Examination of wear debris reveals two types of wear particles i.e. equiaxed irregular morphology with average size of 10 μm and plate like morphology with an in-plate diameter of up to 50 μm. The plate-like morphology of wear particle is a result of delamination wear. It is also evident from Figure 4.43 that the size of plate-like particles rises with frequency. The high cyclic loading (high fatigue-type loading) may have resulted in increased subsurface crack propagation, hence, larger plates.

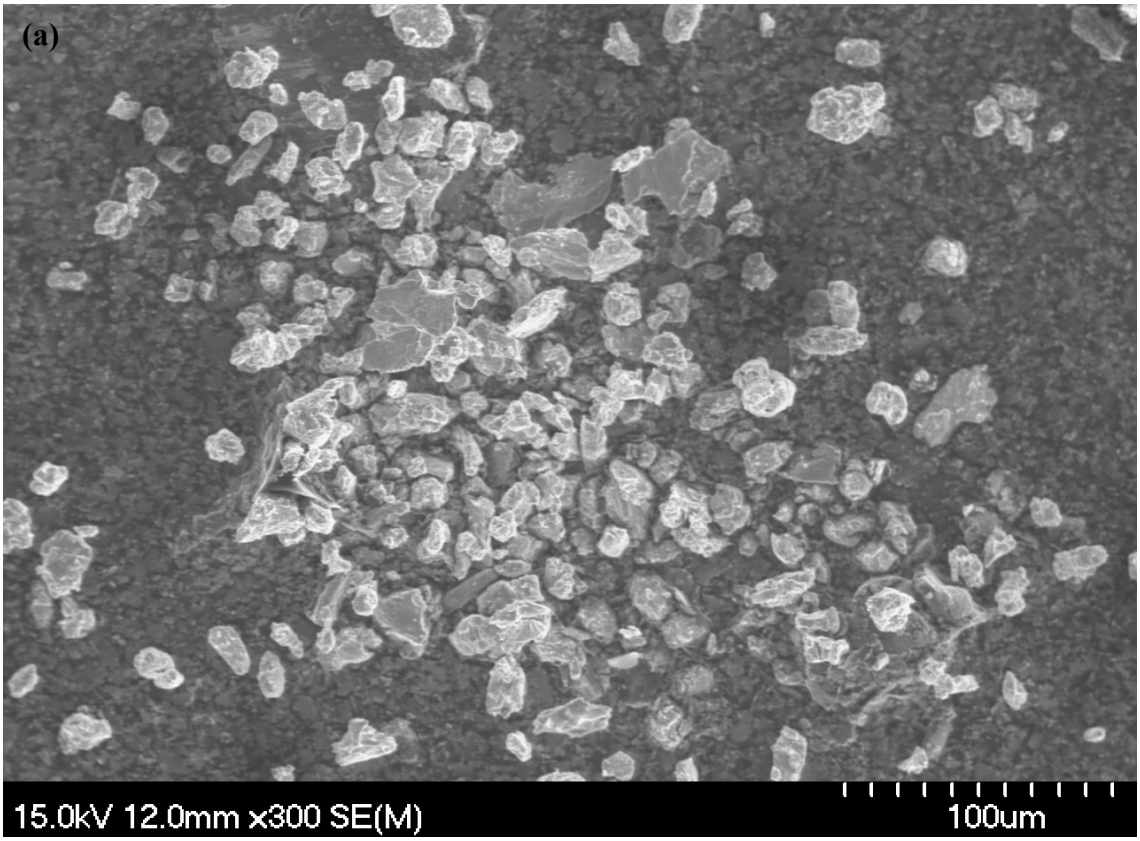
(a)
15.0kV 12.0mm x300 SE(M)
100um

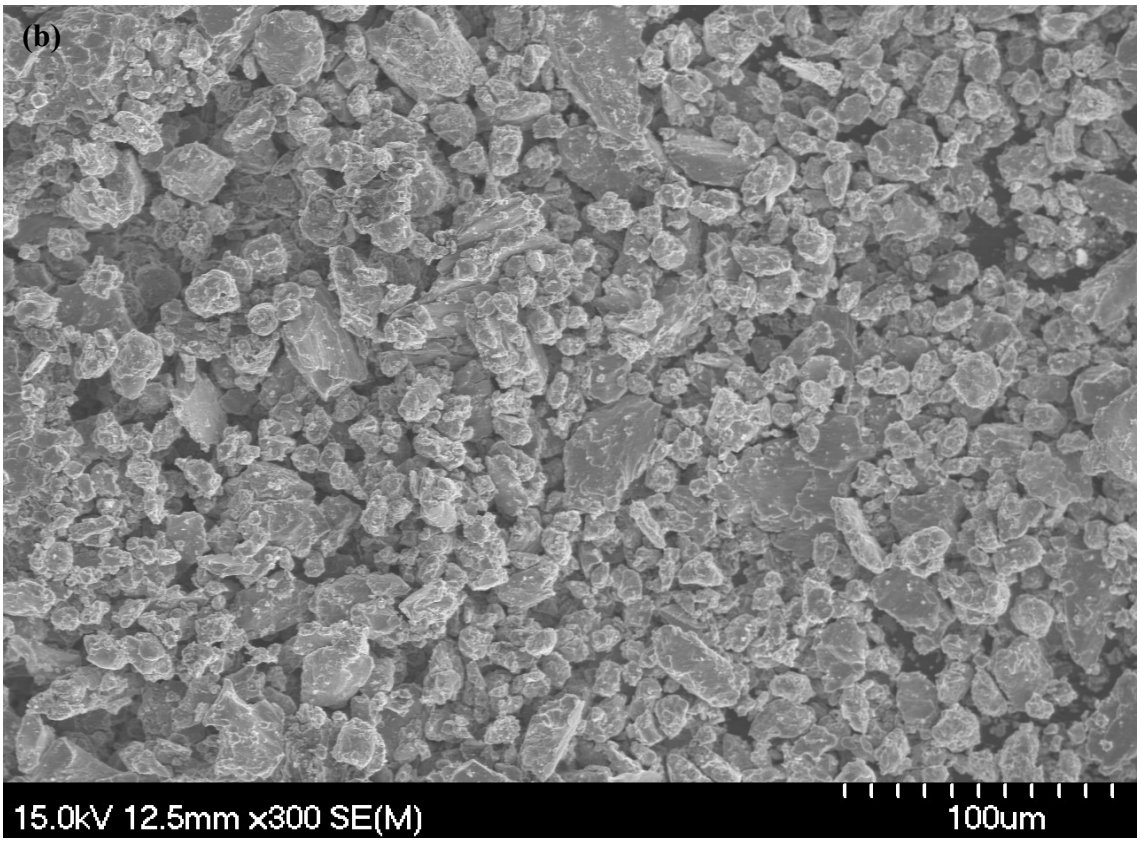
(b)
15.0kV 12.5mm x300 SE(M)
100um

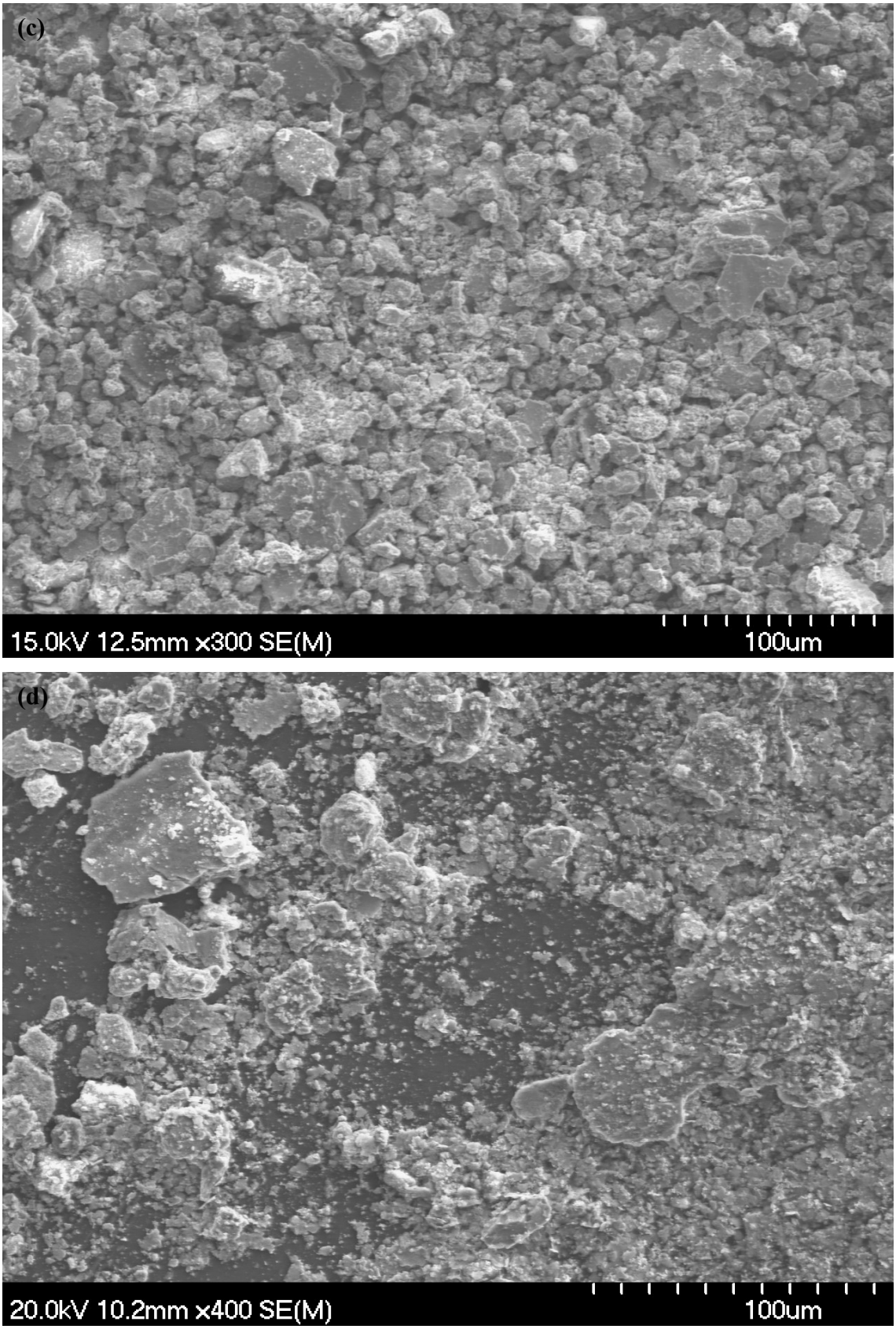

Figure 4.43 SEM micrograph of TiNi wear particles after wear test subjected to 100N load: (a) 5 Hz, (b) 10 Hz, (c) 15 Hz, (d) 20 Hz

5 CONCLUSION

In the present study, indentation and wear behavior of superelastic equiatomic TiNi and 60NiTi (aged, annealed and solution treated) were investigated. The following main conclusions have emerged.

- Within the indentation condition employed in this study, the indenation behavior and dent resistance of TiNi and 60NiTi are not significantly affected by loading rate. Only a mild drop of about 10-15% in the superelasticity is observed as the loading rate is increased. This drop might be attributed to retardation of martensitic transformation upon loading at high loading rates.
- The superior wear and dent resistance of superelastic equiatomic TiNi and 60NiTi is attributed to low E/H and high elastic recovery ratio. The E/H value of TiNi is 15 while that of AISI 304 steel is 85. The average elastic recovery ratio for superelastic TiNi obtained from nanoindentation tests is over 7 times that of AISI 304 stainless steel, although both have similar hardness. The load (for a given indenter) that induces plastic deformation in superelastic TiNi is over two orders of magnitude higher than that of AISI 304 steel.
- Aged and solution treated 60NiTi exhibit slightly enhanced superelasticity compared to equiatomic TiNi (i.e., lower E/H), yet they show about 3 times the hardness and about 40% improvement in wear resistance.
- An effective elastic modulus is developed for superelastic TiNi that is a function of martensite and austenite moduli and elasticity associated with phase transition. The effective elastic modulus of TiNi is depth dependent due to the superelastic effects.
- A load-depth curve is predicted that takes into consideration the reversible martensite transformation. The predicted load-depth curve generated using an effective elastic modulus is in good agreement with experimental data. Predicted forward and reverse transformation loads and their corresponding depths agree well with experimental values.
- Wear rates of TiNi and 60NiTi are found to drop with reciprocating frequency up to 15Hz for loads up to 60N (contact pressure 234 MPa). Under these conditions, hardening as a result of increasing strain rate and austenite to martensite transition

stress, is the dominating effect. For reciprocating frequencies higher than 15Hz and normal loads up to 60N, the wear rate rises as a result of softening due to frictional heating effect. For reciprocating frequencies higher then 15Hz and normal loads higher than 60N (for equiatomic TiNi), wear rate continues to drop as a result of martensite stabilization and work hardening of martensite.

- About 20-25% drop in the steady-state coefficient of friction of TiNi and 60NiTi with frequency was observed due to frictional heating.
- The steady-state coefficient of friction of TiNi and 60NiTi is independent of load up to 60N. Above 60N, the coefficient of friction rises abruptly as the normal load increases to 80N. This rise is believed to be due to increase in shear strength as a result of stabilization and work hardening of martensite.
- Abrasion and delamination are found to be the dominant wear mechanisms at high loads, while mild plastic flow and adhesive wear are dominant at low loads.

Although a fair amount of work has been performed in this study, more work is needed for a comprehensive understanding of indentation and wear behavior. A number of recommendations for future work are listed below:

- Compare indentation and wear behavior of equiatomic TiNi and 60NiTi to tribological materials used for bearings (i.e., AISI 52100 bearing steel).
- Carry out detailed microstructural study of 60NiTi (aged, annealed and solution treated) and relate to its superior dent and wear resistance.
- Develop a comprehensive model to determine hardness and elastic modulus for multi-phase materials that undergo phase transformation during deformation from nanoindentation data.

REFERENCES

Abedini, M., Ghasemi, H. M., & Ahmadabadi, M. N. (2009). Tribological behavior of NiTi alloy in martensitic and austenitic states. *Materials and Design , 10*, 4493-4497.

Adharapurapu, R. R., Jiang, F., Vecchio, K., & Gary III, G. (2006). Response of NiTi shape memory alloy at high strain rate: A systematic investigation of temperature effects on tension-compression asymmetry. *Acta Materialia , 54* (17), 4609-4620.

Amini, A., & Sun, Q. (2010). Rate dependency of depth in nanoindentation of polycrystalline NiTi. *EPJ Web of Conferences , 6*, 29004.

Amini, A., He, Y., & Sun, Q. (2011). Loading rate dependancy of maximum nanoindentation depth in nao-grained NiTi shape memory alloy. *Materials Letters , 65* (3), 464-466.

Amini, A., Yan, W., & Sun, Q. (2011). Depth dependency of indentation hardness during solid-state phase transition of shape memory alloys. *Applied Physics Letters , 99* (2), 021901.

Archard, J. F. (1953). Contact and rubbing of flat surfaces. *Journal of applied physics , 24* (8), 981-988.

Ashby, M. F. (2005). *Materials Selection in Mechanical Design.* Amsterdam: Butterworth-Heinemann.

ASM Handbook: Volume 18. (1992). Materials Park, Ohio: ASM International.

(2010). ASTM Standard G133-05(2010). In *Standard Test Method for Linearly Reciprocating Ball-on Flat Sliding Wear.* West Conshohocken, PA: ASTM International.

Bhushan, B. (2002). *Introduction to Tribology.* New York: John Wiley & Sons.

Bowden, F. P., & Tabor, D. (1950). *The Friction and Lubrication of Solids (Pt.1).* Oxford: Clarendon Press.

Bowden, F. P., & Tabor, D. (1964). *The Friction and Lubrication of Solids (Pt.2).* Oxford: Clarendon Press.

Cheng, Y. T., & Cheng, C. M. (2005). Relationships between initial unloading slope, contact depth, and mechanical properties for spherical indentation in linear viscoelastic solids. *Materials Science and Engineering: A , 409* (1-2), 93-99.

Cheng, Y. T., & Cheng, C. M. (2004). Scaling, dimensional analysis, and indentation measurements. *Materials Science and Engineering: R , 44* (4-5), 91-149.

Dayananda, G. N., & Rao, M. S. (2008). Effect of strain rate on properties of superelastic NiTi thin wires. *Materials Science and Engineering A , 486* (1-2), 96-103.

De Guzman, M. S., Neubauer, G., Flinn, P., & Nix, W. D. (1993). The Role of Indentation Depth on the Measured Hardness of Materials. *Materials Research Society Symposium Proceedings , 308*, 613-618.

DellaCorte, C., Pepper, S. V., Noebe, R., Hull, D. R., & Glennon, G. (2009). Intermetallic nickel-titanium alloys for oil-lubricated bearing applications. *Power Transmission Engineering , 8*, 26-35.

Dieter, G. E. (1976). *Mechanical Metallurgy* (2nd ed.). New York: McGraw-Hill.

Duwezand, P., & Talor, J. L. (1950). The structure of intermediate phase in alloys of titanium with iron, cobalt and nickel. *Trans AIME , 188*, 1173-1176.

Ebenstein, D. M., & Pruitt, L. A. (2006). Nanoindentation of biological materials. *Nano Today , 1* (3), 26-33.

Farhat, Z. N., & Zhang, C. (2010). The Role of Reversible Martensite Transformation in the Wear Process of TiNi Shape Memory Alloy. *Tribology Transactions , 53*, 917-926.

Farhat, Z., & Zhang, C. (2010). On the Deformation of Superelastic TiNi Alloy. *Tribology Letters , 37* (2), 169-173.
Farhat, Z., Jarjoura, G., & Shahirnia, M. (2013). Dent Resistance and Effect of Indentation Loading Rate on Superelastic TiNi Alloy. *Metallurgical and Materials Transaction A , 44* (8), 3544-3551.
Feng, X.-Q., Qian, L., Yan, W., & Sun, Q. (2008). Wearless scratch on NiTi shape memory alloy due to phase transformation shakedown. *Applied Physics Letters , 92* (12).
Fischer-Cripps, A. C. (2000). *Introduction to Contact Mechanics.* New York: Springer.
Fischer-Cripps, A. C. (2007). *Introduction to Contact Mechanics* (2nd ed.). New York: Springer.
Fischer-Cripps, A. C. (2011). *Nanoindentation* (Vol. 1). New York: Springer.
Fleck, N. A., & Hutchinson, J. W. (1997). Strain Gradient Plasticity. *Advances in Applied Mechanics , 33*, 295-361.
Gao, H., Huang, Y., Nix, W. D., & Hutchinson, J. W. (1999). Mechanism-based strain gradient plasticity— I. Theory. *Journal of the Mechanics and Physics of Solids , 47* (6), 1239-1263.
Gohar, R., & Homer, R. (2008). *Fundamentals of Tribology.* London: Imperial College Press.
Guda Vishnu, K., & Strachan, A. (2010). Phase stability and transformations in NiTi from density function theory calculations. *Acta Materialia , 58* (3), 745-752.
He, Y. J., & Sun, Q. P. (2010). Macroscopic equilibrium domain structure and geometric compatibility in elastic phase transition of thin plates. *International Journal of Mechanical Sciences , 52* (2), 198-211.
Hertz, H. (1896). *Miscellaneous Papers.* London: Macmillan and Co., Ltd.
Hirth, J. P., & Rigney, D. A. (1976). Crystal Plasticity and the Delamination Theory of Wear. *Wear , 39* (1), 133-141.
Huang, W. M., Su, J. F., Hong, M. H., & Yang, B. (2005). Pile-up and sink-in in micro-indentation of a NiTi shape-memory alloy. *Scripta Materialia , 53* (9), 1055-1057.
Huang, Y., Gao, H., Nix, W. D., & Hutchinson, J. W. (2000). Mechanism-based strain gradient plasticity—II. Analysis. *Journal of the Mechanics and Physics of Solids , 48* (1), 99-128.
Jin, C., & Wei, W. (2009). Wear. In R. Nayaran (Ed.), *Biomedical Materials* (pp. 183-199). New York: Springer.
Kan, Q., Yan, W., Kang, G., & Sun, Q. (20013). Oliver–Pharr indentation method in determining elastic moduli of shape memory alloys—A phase transformable material. *Journal of the Mechanics and Physics of Solids , 61* (10), 2015-2033.
Kang, G., & Yan, W. (2010). Scaling relationships in sharp conical indentation of shape memory alloys. *Philosophical Magazine , 90* (5), 599-616.
Kang, G., Kan, Q., Qian, L., & Liu, Y. (2009). Ratchetting deformation of super-elastic and shape-memory NiTi alloys. *Mechanics of Materials , 41* (2), 139-153.
Kim, S., & Cho, M. (2010). A strain rate effect of Ni-Ti shape memory alloy wire. *Japanese Journal of Applied Physics , 49* (11), 115801.
Kumar, P. K., & Lagoudas, D. C. (2008). Introduction to Shape Memory Alloys. In D. C. Lagoudas, *Shape Memory Alloys : Modeling and Engineering Applications* (pp. 1-51). New York: Springer.
Lagoudas, D. C. (Ed.). (2008). *Shape Memory Alloys Modeling and Engineering Applications.* New York: Springer.

Larsen-Basse, J. (1992). Basic theory of solid friction. In P. Blau (Ed.), *ASM Handbook Volume 18: Friction, Lubrication, and Wear Technology* (pp. 27-38). Materials Park, OH: ASM International.
Li, D. Y. (1998). A new type of wear-resistant material; pseudo-elastic TiNi alloy. *Wear , 221* (2), 116-123.
Li, D. Y. (2000). Develpoment of novel wear-resistance materials: TiNi-based pseudoelastic tribomaterials. *Materials & Design , 21* (6), 551-555.
Li, D. Y., & Liu, R. (1999). The Mechanism Responsible for High Wear Resistance of Pseudo-Elastic TiNi Alloy-a Novel Tribo-Material. *Wear , 225-229* (Part 2), 777-783.
Liang, Y. N., Li, S. Z., Jin, Y. B., Jin, W., & Li, S. (1996). Wear behavior of a TiNi alloy. *Wear , 198* (1/2), 236-241.
Lim, S. C. (1998). Recent Developments in Wear-Mechanism Maps. *Tribology International , 31* (1/2), 87.
Lim, S. C., Ashby, M. F., & Brunton, J. H. (1987). Wear-rate transitions and their relationship to wear mechanisms. *Acta Metallurgica , 35* (6), 1343-1348.
Lin, H. C., He, J. L., Chen, K. C., Liao, H. M., & Lin, K. M. (1997). Wear characteristics of TiNi shape memory alloys. *Metallurgical and Materials Transactions A , 28* (9), 1871-1877.
Lin, P., Tobushi, H., Tanaka, K., Hattori, T., & Makita, M. (1994). Pseudoelastic behaviour of TiNi shape memory alloy subjected to strain variations. *Journal of Intelligent Materials Systems and Structures , 5*, 694-701.
Liu, R., & Li, D. Y. (2000). Experimental Studies on Tribological Properties of Pseudoelastic TiNi Alloy with Comparison to Stainless Steel 304. *Metallurgical and Materials Transactions A , 31* (11), 2773-2783.
Liu, R., Li, D. Y., Xie, Y. S., Llewellyn, R., & Hawthorne, H. M. (1999). Indentation behavior of pseudoelastic TiNi alloy. *Scripta Materialia , 41* (7), 691-696.
Liu, Y., Li, Y., & Ramesh, K. T. (2002). Rate dependence of deformation mechanisms in a shape memory alloy. *Philosophical Magazine A , 82*, 2461-2473.
Liu, Y., Ramesh, K. T., & Humbeeck, J. V. (1999). High strain rate deformation of martensite NiTi shape memory alloy. *Scripta Materialia , 41* (1), 89-95.
Ludema, K. C. (1996). *Friction, wear, lubrication: a textbook in tribology.* Boca Raton: CRC Press.
Ma, Z., Long, S., Pan, Y., & Zhou, Y. (2008). Indentation depth dependence of the mechanical strength of Ni films. *Journal of Applied Physics , 103* (4), 043512.
Meng, H. C., & Ludema, K. C. (1995). Wear Models and Predictive Equations: Their Form and Content. *Wear , 181/183* (2), 443.
Miyazaki, S., Imai, T., Igo, Y., & Otsuka, K. (1986). Effect of Cyclic Deformation on the Pseudoelasticity Characteristics of Ti-Ni Alloys. *Metallurgical Transaction A , 17A*, 115-120.
Nemat-Nasser, S., Choi, J., Guo, W., & Isaacs, J. (2005). Very high strain-rate response of a NiTi shape memory alloy. *Mechanics of Materials , 37* (2), 287-298.
Nemat-Nasser, S., Choi, J., Guo, W., Isaacs, J., & Taya, M. (2005). High Strain-Rate, Small Strain Response of a NiTi Shape-Memory Alloy. *Journal of Engineering Materials and Technology , 127* (1), 83-89.
Neupane, R., & Farhat, Z. (2013). Wear and dent resistance of superelastic TiNi alloy. *Wear , 301* (1-2), 682-687.

Ni, W., Cheng, Y. T., & Grummon, D. S. (2003). Microscopic superelastic behavior of a nickel-titanium alloy under complex loading conditions. *Applied Physics Letters , 82* (17), 2811-2813.
Nishida, M., Wayman, C. M., & Honma, T. (1986). Precipitation processes in near-equiatomic TiNi shape memory alloys. *Metallurgical Transaction A , 17* (9), 1505-1515.
Nix, W. D., & Gao, H. (1998). Indentation size effects in crystalline materials: A law for strain gradient plasticity. *Journal of the Mechanics and Physics of Solids , 46* (3), 411-425.
Oliver, W. C., & Pharr, G. M. (1992). An Improved Technique for Determining Hardness and Elastic Modulus Using Load and Displacement Sensing Indentation Experiments. *Journal of Materials Research , 7* (6), 1564-1583.
Oliver, W. C., & Pharr, G. M. (2004). Measurement of hardness and elastic modulus by instrumented indentation: Advances in understanding and refinements to methodology. *Journal of Materials Research , 19* (1), 3-20.
Otsuka, K., & Ren, X. (2005). Physical metallurgy of Ti-Ni based shape memory alloys. *Progress in Materials Science , 50*, 511-678.
Otsuka, K., & Shimizu, K. (1986). Pseudoelasticity and shape memory effects in alloys. *International Metals Reviews , 31*, 93-114.
Otsuka, K., & Wayman, M. (1999). Mechanism of shape memory effect and superelasticity. In K. Otsuka, & M. Wayman (Eds.), *Shape Memory Materials* (pp. 27-48). Cambridge, England: Cambridge University Press.
Pike, R., & Conway-Jones, J. M. (1992). Friction and wear of sliding bearings. In P. Blau (Ed.), *ASM Handbook, Volume 18: Friction, Lubrication, and Wear Technology* (pp. 515-521). Materials Park, OH: ASM International.
Poole, D. M., & Hume-Rothery, W. (1954). The equilibrium diagram of the system nickel-titanium. *Journal: Institute of Metals , 83*, 473-480.
Purdy, G. R., & Parr, J. G. (1961). The Study of the Titanium-Nickel System between Ti2Ni and TiNi. *Trans AIME , 221*, 636-639.
Qian, L., Sun, Q., & Xiao, X. (2006). Role of phase transition in the unusual microwear behavior of superelastic NiTi shape memory alloy. *Wear* , 509-522.
Qian, L., Xiao, X., Sun, Q., & Yu, T. (2004). Anomalous relationship between hardness and wear properties of a superelastic nickel-titanium alloy. *Applied Physics Letters , 84*, 1076-1078.
Saletti, D., Pattofatto, S., & Zhao, H. (2010). Evolution of the martensite transformation in shape memory alloys under high strain rates. *EPJ Web of Conferences , 6*.
Sen, S., & Sen, U. (2009). The effect of boronizing and boro-chromizing on tribological performance of AISI 52100 bearing steels. *Industrial Lubrication and Tribology , 61* (3), 146-153.
Shahirnia, M., Farhat, Z., & Jarjoura, G. (2011). Effects of Temperature and Loading Rate on the Deformation Characteristics of Superelastic TiNi Shape Memory Alloys under Localized Compressive Loads. *Materials Science and Engineering: A , 530*, 628-632.
Sittner, P., Landa, M., Lukas, P., & Novak, V. (2006). R-phase transformation phenomena in thermomechanically loaded NiTi polycrystals. *Mechanics of Materials , 38* (5), 475-492.
Stachowiak, G. W., & Batchelor, A. W. (2005). *Engineering Tribology* (3rd ed.). Amsterdam: Elsevier Butterworth-Heinemann.
Suh, N. P. (1973). The Delamination Theory of Wear. *Wear , 25* (1), 111-124.

Suh, N. P. (1977). *The Delamination Theory of Wear.* Lausanne: Elsevier Sequoia.
Tabor, D. (1996). Indentation hardness: Fifty years on - A personal view. *Philosophical Magazine A , 74* (5), 1207-1212.
Tobushi, H., Iwanaga, H., Tanaka, K., Hori, T., & Sawada, T. (1992). Stress–Strain–Temperature Relationship of TiNi Shape Memeory Alloy Suitable for Thermomechanical Cycling. *JSME International Journal , 35* (3), 271-277.
Tobushi, H., Yoshirou, S., Takashi, H., & Kikuaki, T. (1998). Influence of strain rate on superelastic properties of TiNi shape memory alloy. *Mechanics of Materials , 30* (2), 141-150.
Vogel, R., & Wallbaum, H. J. (1938). The system FeNi-NiTi-FeTi. *Archivfuer das. EisenbuettenWesen , 12*, 296-304.
Wang, Z., Lei, H., Zhou, B., Wang, Y., & Zhang, C. (2011). Influence of strain rate on mechanical properties of shape memory alloy. *Key Engineering Materials , 467-469*, 585-588.
Wen, S., & Huang, P. (2012). *Principles of Tribology.* Singapore: John Wiley & Sons (Asia) Pte Ltd.
Xu, Z. H., & Agren, J. (2004). An analysis of piling-up or sinking-in behaviour of elastic-plastic materials under a sharp indentation. *Philosophical Magazine , 84* (23), 2367-2380.
Xue, Z., Hwang, K. C., Li, M., & Huang, Y. (2002). The Influence of Indenter Tip Radius on the Micro-Indentation Hardness. *Journal of Engineering Materials and Technology , 124* (3), 371-379.
Yan, L., Liu, Y., & Liu, E. (2013). Wear behaviour of martensitic NiTi shape memory alloy under ball-on-disc sliding tests. *Tribology International , 66* (1-2), 219-224.
Yan, W., Sun, Q., Feng, X., & Qian, L. (2007). Analysis of spherical indentation of superelastic shape memory alloys. *International Journal of Solids and Structures , 44* (1), 1-17.
Zaki, W., & Moumni, Z. (2007). A 3D model of the cyclic thermomechanical behavior of shape memory alloys. *Journal of the Mechanics and Physics of Solids , 55* (11), 2427-2454.
Zhang, C., & Farhat, Z. N. (2009). Sliding Wear of Superelastic TiNi Alloy. *267*, 394-400.
Zhang, Y., Cheng, Y. T., & Grummon, D. S. (2007). Finite element modeling of indentation-induced superelastic effect using a three-dimensional constitutive model for shape memory materials with plasticity. *Journal of Applied Physics , 101* (5), 053507.
Zhou, Y., Zhang, J., Fan, G., Ding, X., Sun, J., Ren, X., et al. (2005). Origin of 2-stage R-phase transformation in low-temperature aged Ni-rich Ti-Ni alloys. *Acta Materialia , 53* (20), 5365-5377.

Appendix A: Raw Data (Indentation)

Nanoindentation test results (equiatomic TiNi and 60NiTi under different treatments)

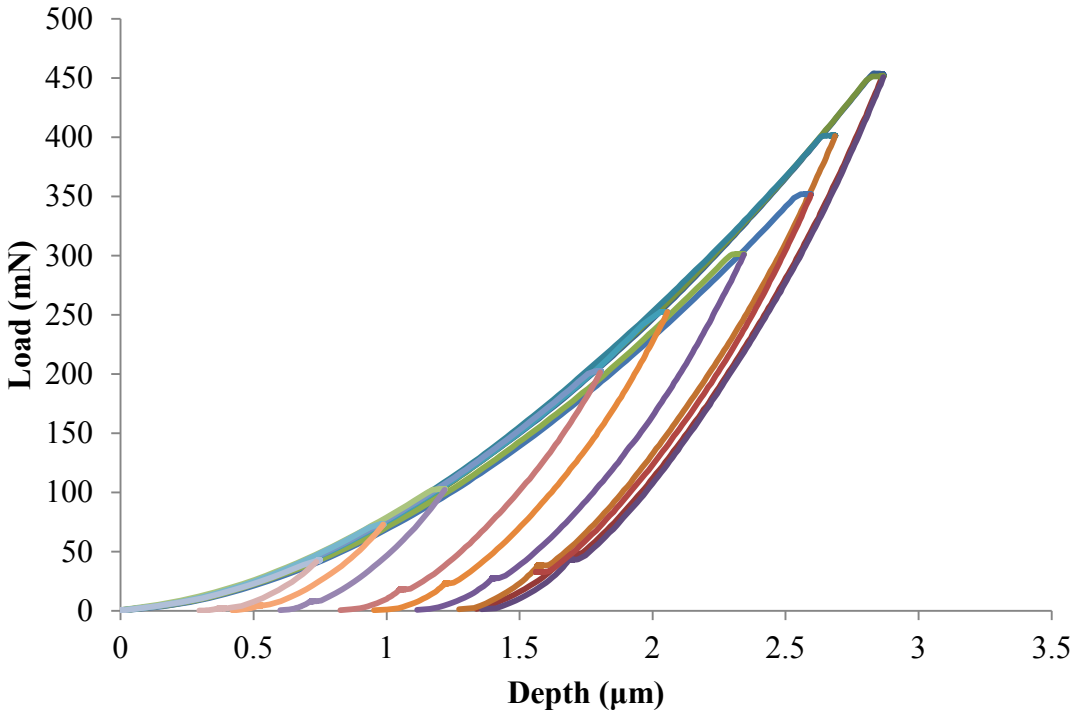
500
450
400
350
300
250
200
150
100
50
0
Load (mN)
0
0.5
1
1.5
2
2.5
3
3.5
Depth (µm)

(a)

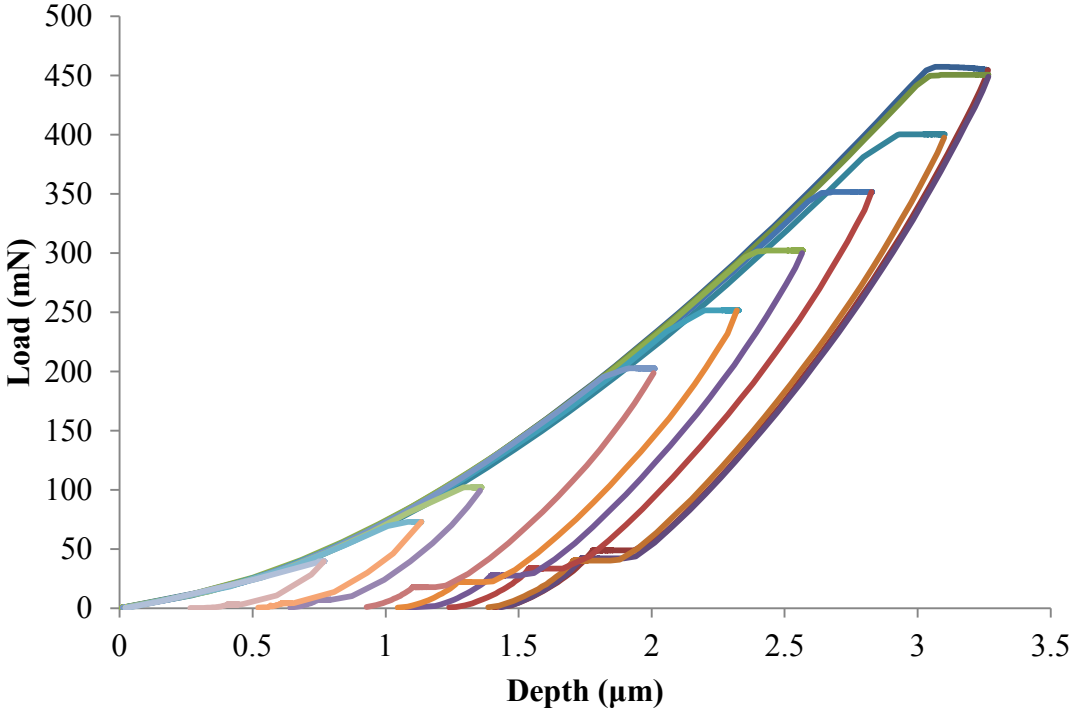
500
450
400
350
300
250
200
150
100
50
0
Load (mN)
0
0.5
1
1.5
2
2.5
3
3.5
Depth (µm)

(b)

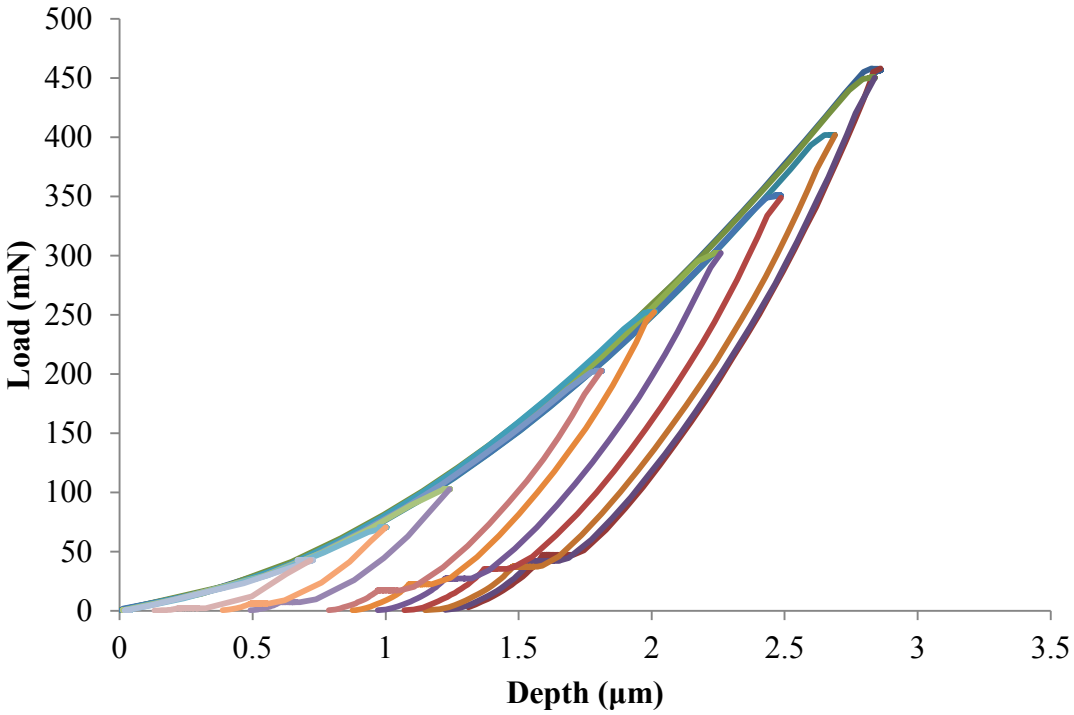
Load (mN)
500
450
400
350
300
250
200
150
100
50
0
0
0.5
1
1.5
2
2.5
3
3.5
Depth (µm)

(c)

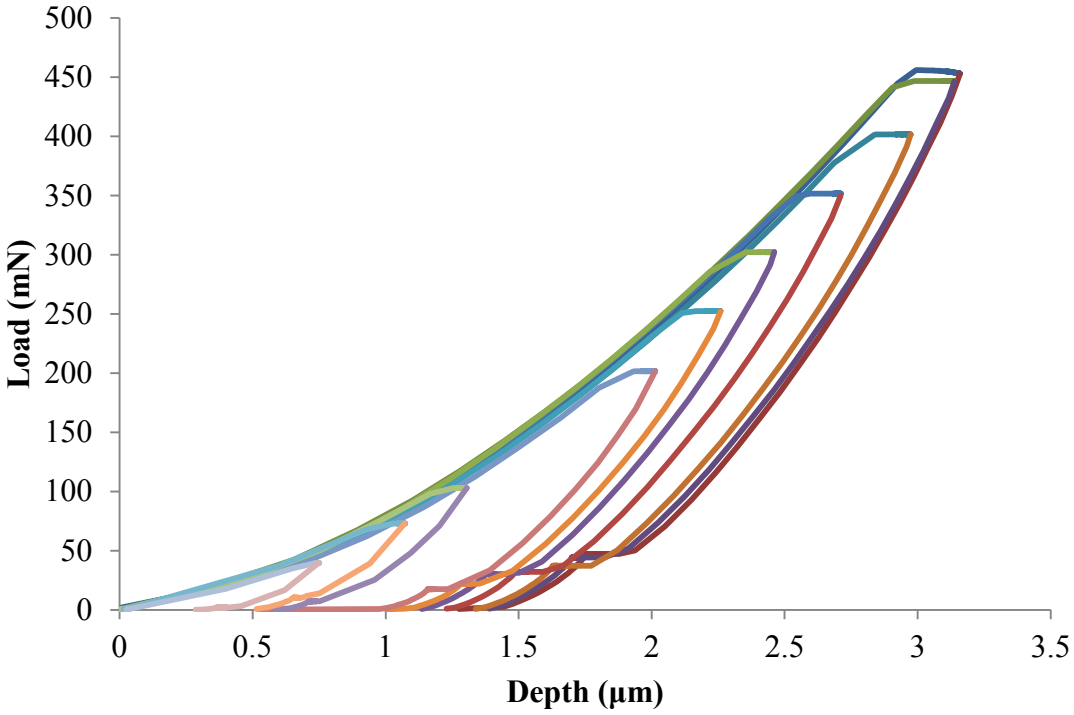
Load (mN)
500
450
400
350
300
250
200
150
100
50
0
0
0.5
1
1.5
2
2.5
3
3.5
Depth (µm)

(d)

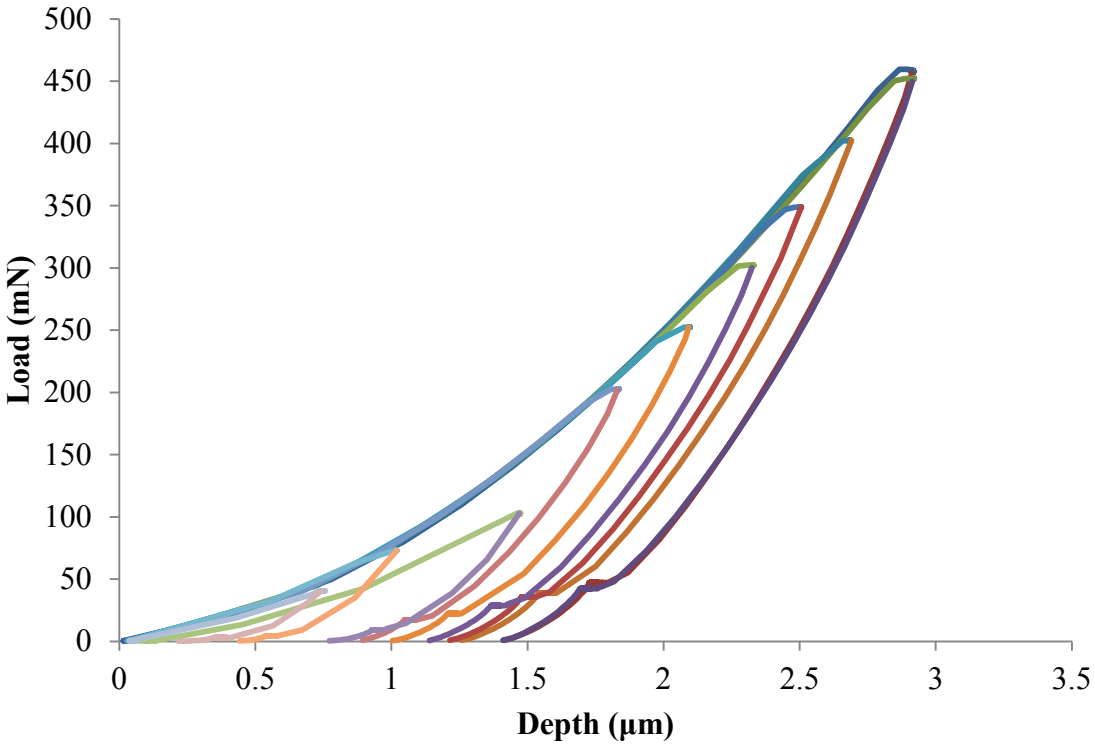
Load (mN)
500
450
400
350
300
250
200
150
100
50
0
0
0.5
1
1.5
2
2.5
3
3.5
Depth (µm)

(e)

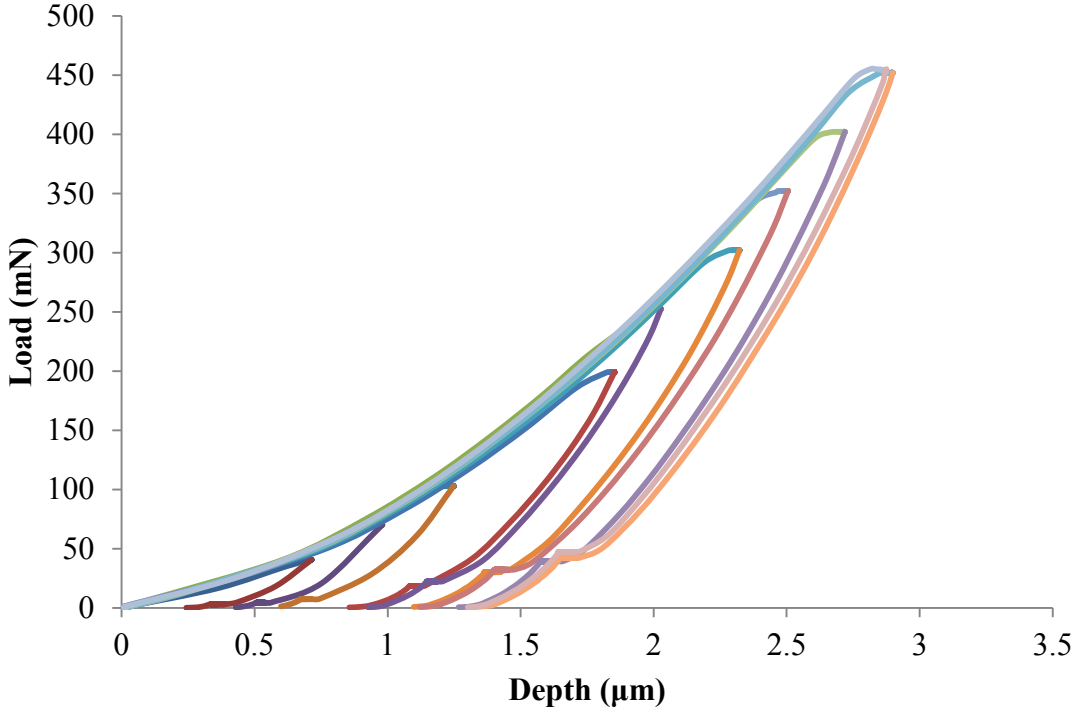
Load (mN)
500
450
400
350
300
250
200
150
100
50
0
0
0.5
1
1.5
2
2.5
3
3.5
Depth (µm)

(f)

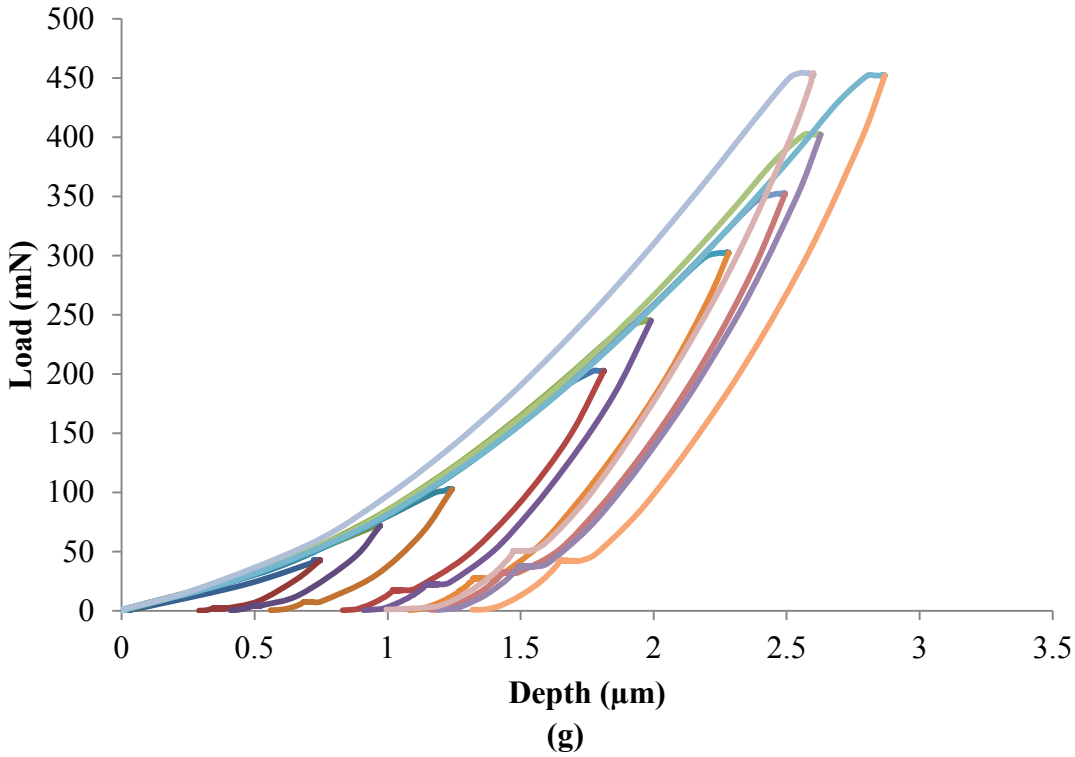

Figure A 1 Indentation curves for equiatomic TiNi with varying maximum loads: (a) 4200mN/min, (b) 18000mN/min, (c) 24000mN/min, (d) 30000mN/min, (e) 36000mN/min, (f) 42000mN/min, (g) 48000mN/min

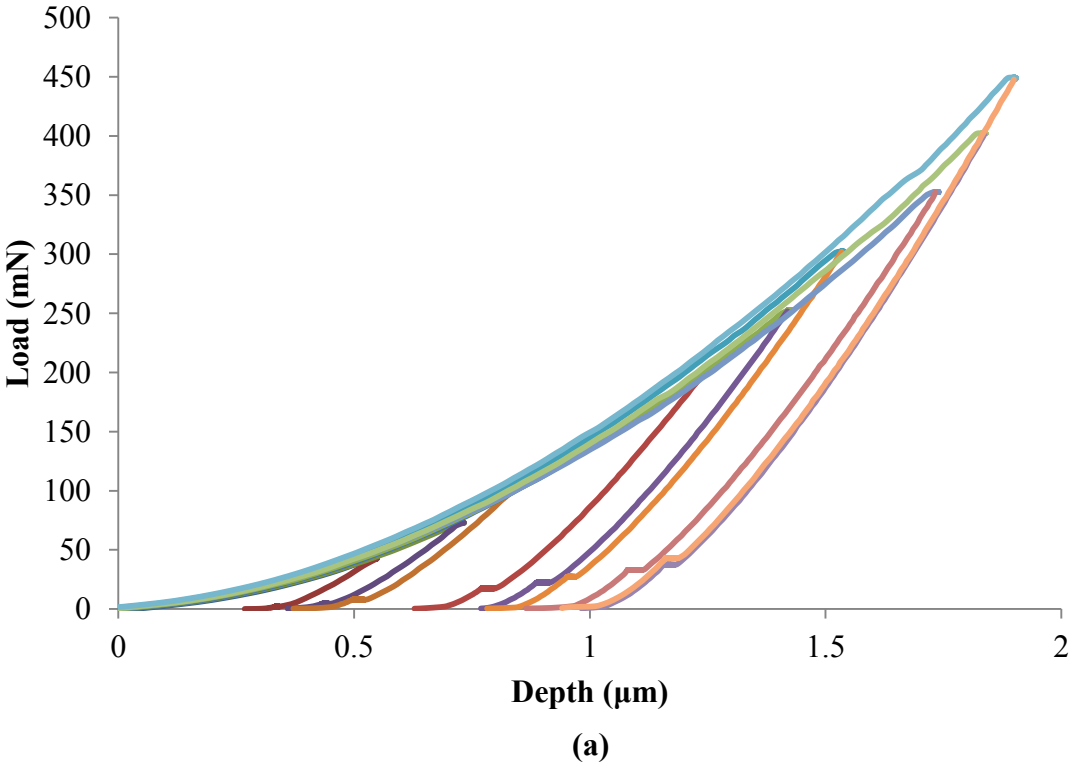

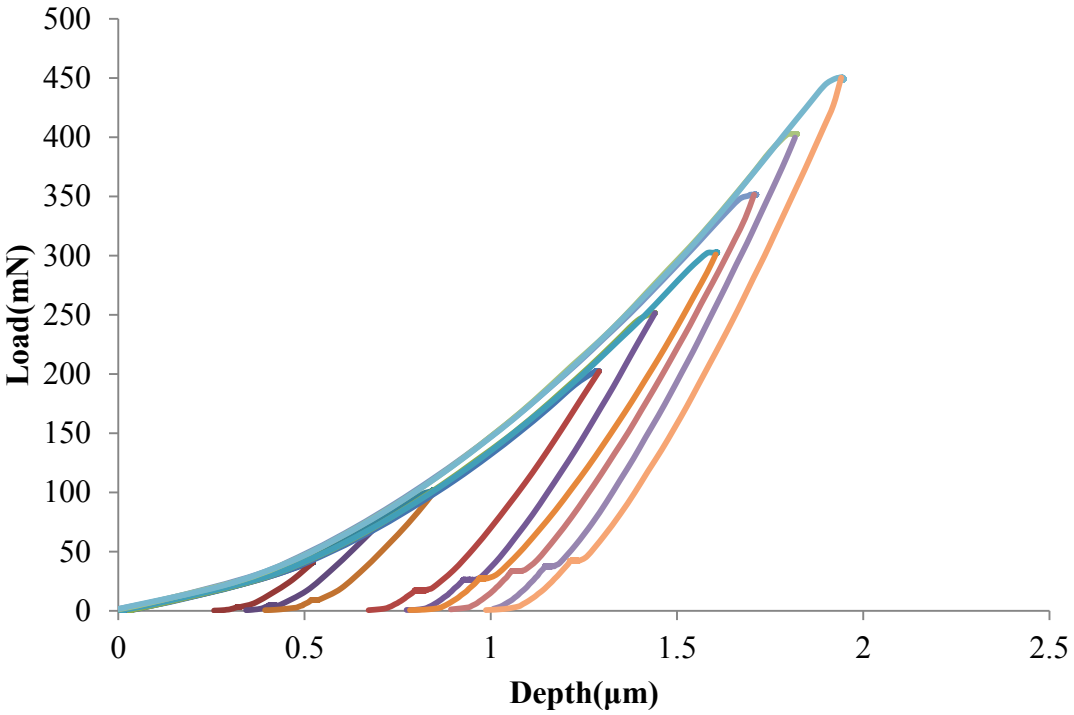

Figure A 2 Indentation curves for aged 60NiTi with varying maximum loads: (a) 4200mN/min, (b) 18000mN/min

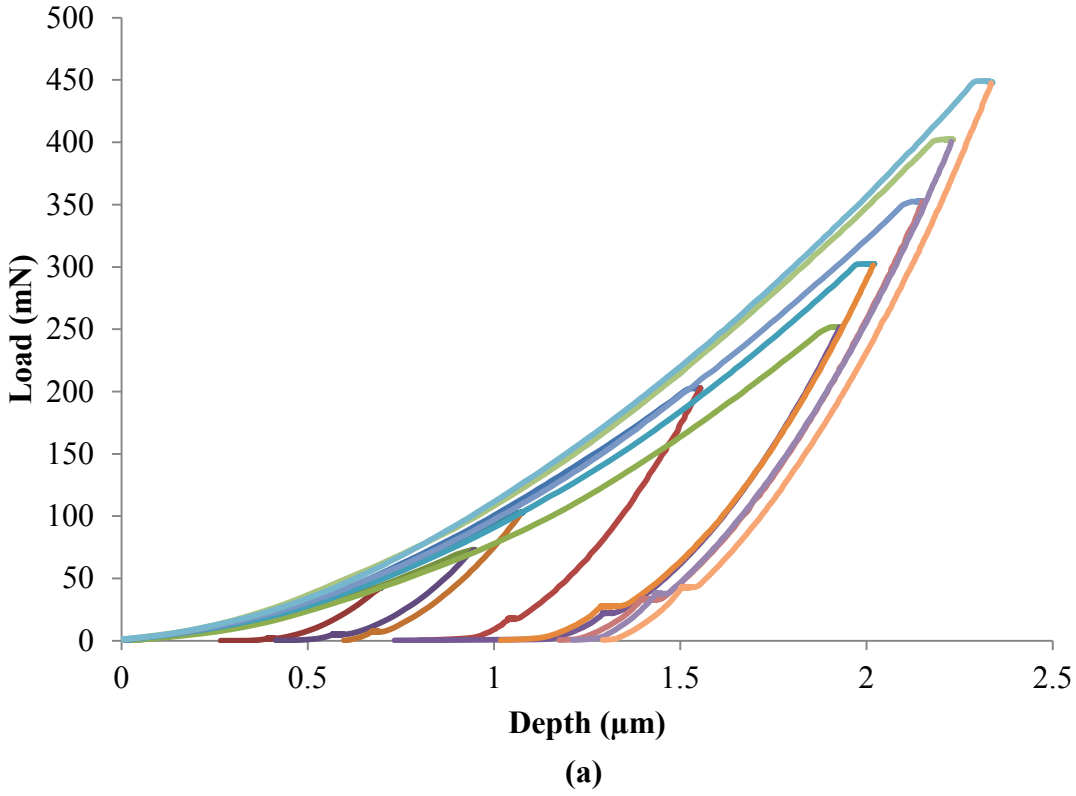

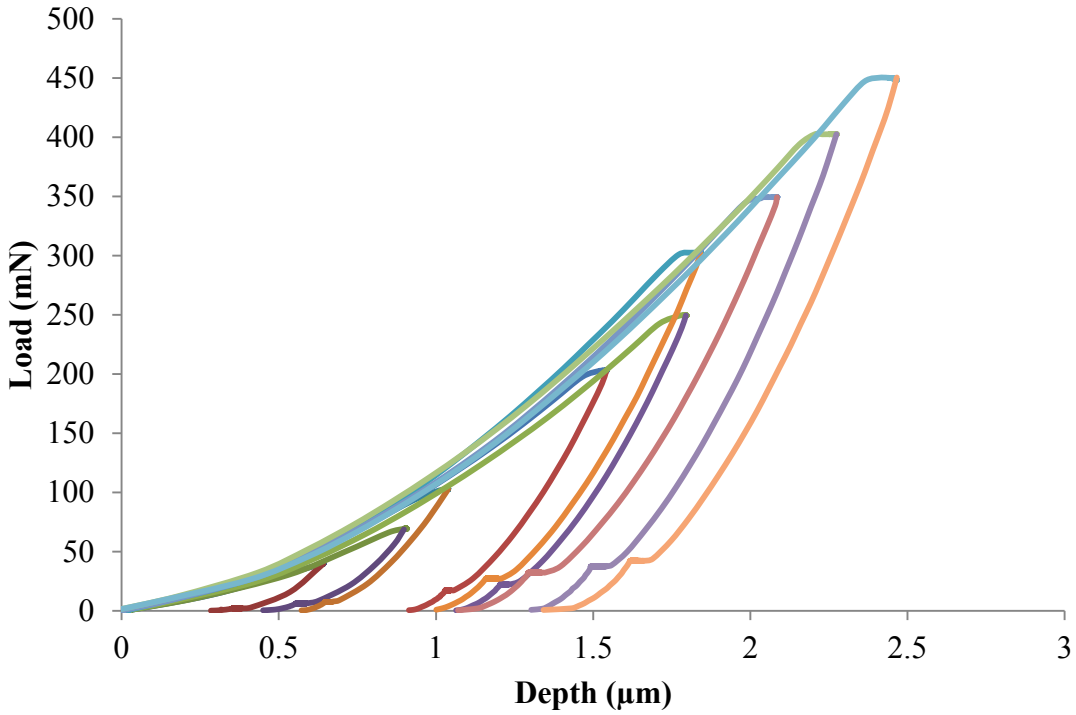

Figure A 3 Indentation curves for annealed 60NiTi with varying maximum loads: (a) 4200mN/min, (b) 18000mN/min

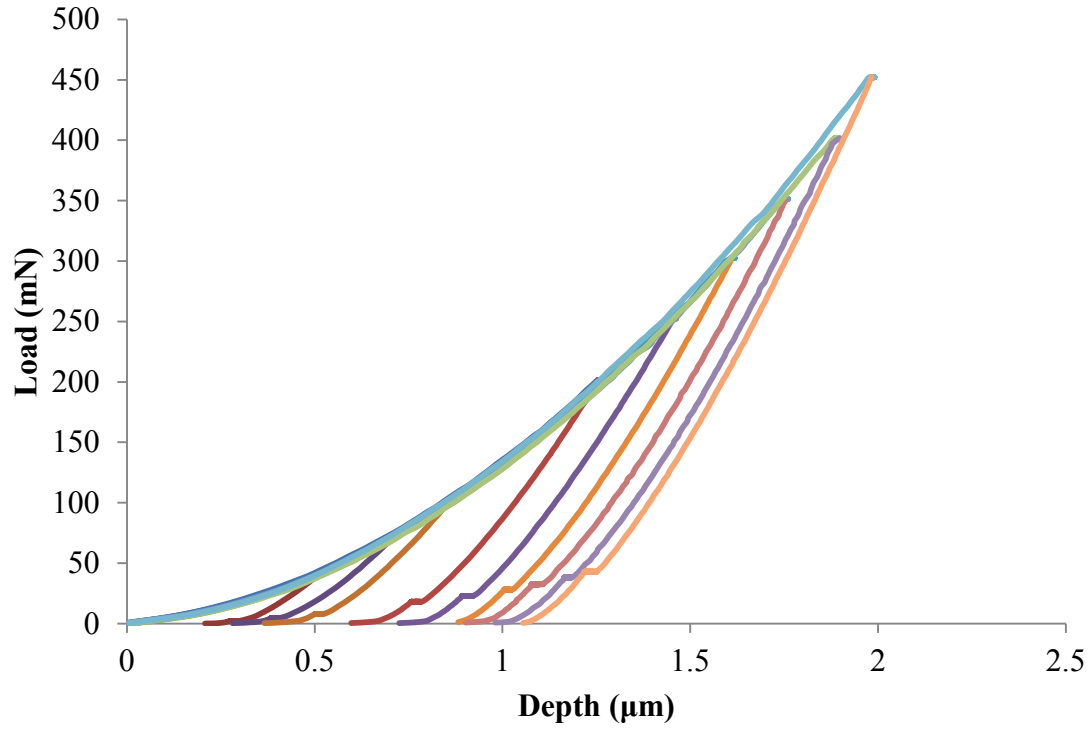

(a)

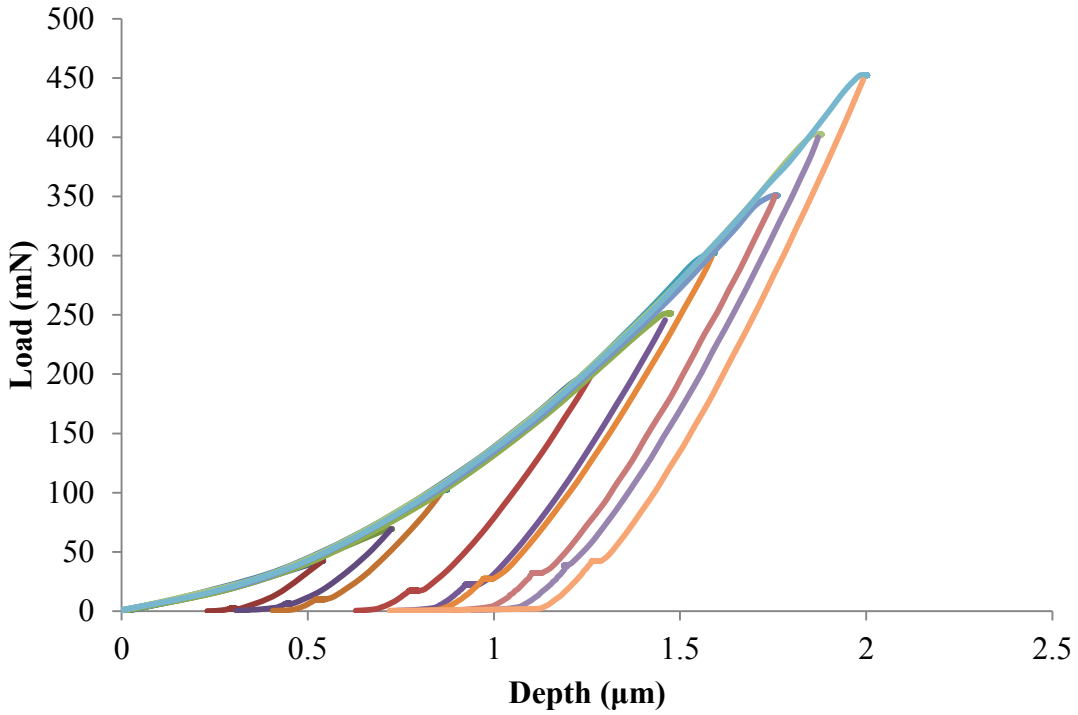

Figure A 4 Indentation curves for solution treated 60NiTi with varying maximum loads: (a) 4200mN/min, (b) 18000mN/min

Appendix B: Raw Data (Wear)

Reciprocating wear test results (equiatomic TiNi and 60NiTi under different treatments)

Table B 1 Reciprocating wear tests data for equiatomic TiNi

Load (N)	Frequency (Hz)	Time (min)	Sliding distance(m)	Weight before(g)	Weight after(g)	Total weight loss(mg)	COF
20	5	30	90.54	13.05351	13.05078	2.73	0.4953
		60	181.08	13.05078	13.0498	3.71	0.6095
		90	271.62	13.0498	13.04855	4.96	0.6198
		120	362.16	13.04855	13.04685	6.66	0.625
		150	452.7	13.04685	13.0457	7.81	0.6138
		180	543.24	13.0457	13.04558	7.93	0.6304
	10	30	181.08	13.04558	13.04064	4.94	0.4269
		60	362.16	13.04064	13.03826	7.32	0.5814
		90	543.24	13.03826	13.03762	7.96	0.5983
		120	724.32	13.03762	13.03741	8.17	0.6095
		150	905.4	13.03741	13.03687	8.71	0.6147
		180	1086.48	13.03687	13.03628	9.3	0.6018
	15	30	271.62	13.03626	13.02858	7.68	0.3688
		60	543.24	13.02858	13.02694	9.32	0.5124
		90	814.86	13.02694	13.0263	9.96	0.5209
		120	1086.48	13.0263	13.02605	10.21	0.5176
		150	1358.1	13.02605	13.02593	10.33	0.5312
		180	1629.72	13.02593	13.02545	10.81	0.509
	20	30	362.16	13.02545	13.02057	4.88	0.3463
		60	724.32	13.02057	13.01813	7.32	0.4363
		90	1086.48	13.01813	13.01723	8.22	0.4397
		120	1448.64	13.01723	13.01445	11	0.4338
		150	1810.8	13.01445	13.01428	11.17	0.4393
		180	2172.96	13.01428	13.01374	11.71	0.4295
40	5	30	90.54	15.24258	15.23796	4.62	0.4635
		60	181.08	15.23796	15.23431	8.27	0.555
		90	271.62	15.23431	15.23149	11.09	0.6128
		120	362.16	15.23149	15.23007	12.51	0.6217
		150	452.7	15.23007	15.22907	13.51	0.6395
		180	543.24	15.22907	15.22677	15.81	0.6473
	10	30	181.08	15.22677	15.21899	7.78	0.4165
		60	362.16	15.21899	15.21326	13.51	0.5551
		90	543.24	15.21326	15.21126	15.51	0.5843
		120	724.32	15.21126	15.20918	17.59	0.5936
		150	905.4	15.20918	15.20865	18.12	0.6108
		180	1086.48	15.20865	15.2078	18.97	0.6173

Table B 1 (contd..)

Load (N)	Frequency (Hz)	Time (min)	Sliding distance(m)	Weight before(g)	Weight after(g)	Total weight loss(mg)	COF
40	15	30	271.62	15.2078	15.20052	7.28	0.3924
		60	543.24	15.20052	15.19469	13.11	0.4452
		90	814.86	15.19469	15.1933	14.5	0.546
		120	1086.48	15.1933	15.19217	15.63	0.5329
		150	1358.1	15.19217	15.19128	16.52	0.5551
		180	1629.72	15.19128	15.19062	17.18	0.5683
	20	30	362.16	15.19425	15.18611	8.14	0.3449
		60	724.32	15.18611	15.18115	13.1	0.3926
		90	1086.48	15.18115	15.1779	16.35	0.4628
		120	1448.64	15.1779	15.17619	18.06	0.4768
		150	1810.8	15.17619	15.17466	19.59	0.4806
		180	2172.96	15.17466	15.17341	20.84	0.4543
60	5	30	90.54	15.27435	15.26824	6.11	0.4889
		60	181.08	15.26824	15.26171	12.64	0.5409
		90	271.62	15.26171	15.25684	17.51	0.5912
		120	362.16	15.25684	15.25391	20.44	0.6574
		150	452.7	15.25391	15.25273	21.62	0.6832
		180	543.24	15.25273	15.2512	23.15	0.6912
	10	30	181.08	15.2512	15.2406	10.6	0.4334
		60	362.16	15.2406	15.23402	17.18	0.5398
		90	543.24	15.23402	15.23151	19.69	0.5703
		120	724.32	15.23151	15.2278	23.4	0.5703
		150	905.4	15.2278	15.22628	24.92	0.6152
		180	1086.48	15.22628	15.22554	25.66	0.6239
	15	30	271.62	15.21896	15.20912	9.84	0.437
		60	543.24	15.20912	15.20614	12.82	0.473
		90	814.86	15.20614	15.20333	15.63	0.4996
		120	1086.48	15.20333	15.20257	16.39	0.5355
		150	1358.1	15.20257	15.20135	17.61	0.553
		180	1629.72	15.20135	15.19987	19.09	0.5589
	20	30	362.16	14.27266	14.26098	11.68	0.3736
		60	724.32	14.26098	14.25643	16.23	0.4534
		90	1086.48	14.25643	14.2533	19.36	0.4767
		120	1448.64	14.2533	14.25091	21.75	0.5188
		150	1810.8	14.25091	14.24875	23.91	0.531
		180	2172.96	14.24875	14.24654	26.12	0.4953

Table B 1 (contd..)

Load (N)	Frequency (Hz)	Time (min)	Sliding distance(m)	Weight before(g)	Weight after(g)	Total weight loss(mg)	COF
80	5	30	90.54	15.30218	15.2955	6.72	0.5898
		60	181.08	15.29546	15.2867	15.45	0.7038
		90	271.62	15.28673	15.2801	22.08	0.8062
		120	362.16	15.2801	15.2745	27.64	0.8228
		150	452.7	15.27454	15.2717	30.49	0.8467
		180	543.24	15.27169	15.27	32.14	0.7576
	10	30	181.08	14.71974	14.7063	13.45	0.6375
		60	362.16	14.70629	14.7003	19.44	0.6922
		90	543.24	14.7003	14.6976	22.19	0.7274
		120	724.32	14.69755	14.6953	24.41	0.7185
		150	905.4	14.69533	14.6931	26.69	0.7446
		180	1086.48	14.69305	14.6908	28.9	0.7946
	15	30	271.62	15.25099	15.2402	10.79	0.4617
		60	543.24	15.2402	15.2357	15.26	0.5941
		90	814.86	15.23573	15.232	19.01	0.6221
		120	1086.48	15.23198	15.229	21.97	0.6776
		150	1358.1	15.22902	15.227	23.95	0.6767
		180	1629.72	15.22704	15.225	26.02	0.7258
	20	30	362.16	15.22497	15.2144	10.61	0.4328
		60	724.32	15.21436	15.2102	14.79	0.5523
		90	1086.48	15.21018	15.2063	18.71	0.5986
		120	1448.64	15.20626	15.2033	21.72	0.6093
		150	1810.8	15.20325	15.2	24.96	0.6185
		180	2172.96	15.20001	15.1971	27.86	0.6445
100	5	30	90.54	13.45078	13.4416	9.23	0.5319
		60	181.08	13.44155	13.4321	18.7	0.6679
		90	271.62	13.43208	13.4248	25.96	0.7636
		120	362.16	13.42482	13.42	30.79	0.7868
		150	452.7	13.41999	13.416	34.76	0.825
		180	543.24	13.41602	13.4138	36.95	0.8634
	10	30	181.08	13.41383	13.3987	15.15	0.4738
		60	362.16	13.39868	13.3915	22.38	0.682
		90	543.24	13.39145	13.3877	26.18	0.7259
		120	724.32	13.38765	13.3844	29.44	0.7507
		150	905.4	13.38439	13.3817	32.09	0.7889
		180	1086.48	13.38174	13.3796	34.25	0.8289

Table B 1 (contd..)

Load (N)	Frequency (Hz)	Time (min)	Sliding distance(m)	Weight before(g)	Weight after(g)	Total weight loss(mg)	COF
100	15	30	271.62	13.38132	13.3674	13.91	0.4169
		60	543.24	13.36741	13.3625	18.81	0.5256
		90	814.86	13.36251	13.3576	23.72	0.5735
		120	1086.48	13.3576	13.3531	28.2	0.6263
		150	1358.1	13.35312	13.3496	31.75	0.6858
		180	1629.72	13.34957	13.3465	34.8	0.7357
	20	30	362.16	13.34652	13.3333	13.27	0.3946
		60	724.32	13.33325	13.3276	18.9	0.4991
		90	1086.48	13.32762	13.3221	24.39	0.5416
		120	1448.64	13.32213	13.3174	29.13	0.5919
		150	1810.8	13.31739	13.3138	32.75	0.6402
		180	2172.96	13.31377	13.3098	36.72	0.677

Table B 2 Reciprocating wear tests data for aged 60NiTi

Load (N)	Frequency (Hz)	Time (min)	Sliding distance(m)	Weight before(g)	Weight after(g)	Total weight loss(mg)	COF
20	5	30	90.54	17.21034	17.20956	0.78	0.5255
		60	181.08	17.20956	17.20844	1.9	0.6069
		90	271.62	17.20844	17.20806	2.28	0.6283
		120	362.16	17.20806	17.20745	2.89	0.6337
		150	452.7	17.20745	17.20705	3.29	0.6186
		180	543.24	17.20705	17.20674	3.6	0.6133
	10	30	181.08	17.21704	17.21475	2.29	0.4976
		60	362.16	17.21475	17.21368	3.36	0.5645
		90	543.24	17.21368	17.21216	4.88	0.5856
		120	724.32	17.21216	17.21165	5.39	0.588
		150	905.4	17.21165	17.21034	6.7	0.5908
		180	1086.48	17.21127	17.21034	7.63	0.5931
	15	30	271.62	17.22423	17.22079	3.44	0.488
		60	543.24	17.22079	17.21964	4.59	0.4974
		90	814.86	17.21964	17.21887	5.36	0.517
		120	1086.48	17.21887	17.2183	5.93	0.5262
		150	1358.1	17.2183	17.21745	6.78	0.5252
		180	1629.72	17.21745	17.21704	7.19	0.5452
	20	30	362.16	17.23347	17.22902	4.45	0.4316
		60	724.32	17.22902	17.22777	5.7	0.4455
		90	1086.48	17.22777	17.22655	6.92	0.4706
		120	1448.64	17.22655	17.22541	8.06	0.4837
		150	1810.8	17.22541	17.22432	9.15	0.4906
		180	2172.96	17.22432	17.22306	10.41	0.488
40	5	30	90.54	18.2218	18.22011	1.69	0.472
		60	181.08	18.22011	18.21748	4.32	0.5328
		90	271.62	18.21748	18.2155	6.3	0.5667
		120	362.16	18.2155	18.21367	8.13	0.5813
		150	452.7	18.21367	18.21229	9.51	0.6069
		180	543.24	18.21229	18.21152	10.28	0.6268
	10	30	181.08	18.23534	18.23082	4.52	0.4926
		60	362.16	18.23082	18.22662	8.72	0.5134
		90	543.24	18.22662	18.22452	10.82	0.5737
		120	724.32	18.22452	18.2231	12.24	0.5882
		150	905.4	18.2231	18.22186	13.48	0.6008
		180	1086.48	18.22186	18.22067	14.67	0.6102

Table B 2 (contd..)

Load (N)	Frequency (Hz)	Time (min)	Sliding distance(m)	Weight before(g)	Weight after(g)	Total weight loss(mg)	COF
40	15	30	271.62	18.25	18.2437	6.3	0.4555
		60	543.24	18.2437	18.24074	9.26	0.4991
		90	814.86	18.24074	18.2389	11.1	0.5137
		120	1086.48	18.2389	18.23764	12.36	0.5299
		150	1358.1	18.23764	18.23655	13.45	0.5416
		180	1629.72	18.23655	18.23534	14.66	0.548
	20	30	362.16	18.26884	18.26265	6.19	0.3814
		60	724.32	18.26265	18.25943	9.41	0.4397
		90	1086.48	18.25943	18.25719	11.65	0.4539
		120	1448.64	18.25719	18.25462	14.22	0.479
		150	1810.8	18.25462	18.25251	16.33	0.4917
		180	2172.96	18.25251	18.25	18.84	0.5085
60	5	30	90.54	20.06726	20.06478	2.48	0.479
		60	181.08	20.06478	20.06162	5.64	0.4943
		90	271.62	20.06162	20.0595	7.76	0.539
		120	362.16	20.0595	20.05804	9.22	0.5588
		150	452.7	20.05804	20.05608	11.18	0.5641
		180	543.24	20.05608	20.05498	12.28	0.5816
	10	30	181.08	20.05498	20.04694	8.04	0.4511
		60	362.16	20.04694	20.04036	14.62	0.5318
		90	543.24	20.04036	20.03839	16.59	0.5639
		120	724.32	20.03839	20.03696	18.02	0.5641
		150	905.4	20.03625	20.0359	18.37	0.5872
		180	1086.48	20.0359	20.03517	19.1	0.592
	15	30	271.62	20.03517	20.02393	11.24	0.4034
		60	543.24	20.02393	20.02255	12.62	0.4903
		90	814.86	20.02255	20.02102	14.15	0.5038
		120	1086.48	20.02102	20.01981	15.36	0.5322
		150	1358.1	20.01981	20.01854	16.63	0.5158
		180	1629.72	20.01854	20.01745	17.72	0.5669
	20	30	362.16	20.01023	19.99845	11.78	0.3713
		60	724.32	19.99845	19.99628	13.95	0.4223
		90	1086.48	19.99628	19.99471	15.52	0.4273
		120	1448.64	19.99471	19.9928	17.43	0.436
		150	1810.8	19.9928	19.99063	19.6	0.4534
		180	2172.96	19.99063	19.98829	21.94	0.449

Table B 3 Reciprocating wear tests data for annealed 60NiTi

Load (N)	Frequency (Hz)	Time (min)	Sliding distance(m)	Weight before(g)	Weight after(g)	Total weight loss(mg)	COF
20	5	30	90.54	18.36511	18.36254	2.57	0.5314
		60	181.08	18.36254	18.36063	4.48	0.5715
		90	271.62	18.36063	18.35986	5.25	0.588
		120	362.16	18.35986	18.35904	6.07	0.5903
		150	452.7	18.35904	18.35823	6.88	0.592
		180	543.24	18.35823	18.35771	7.4	0.6466
	10	30	181.08	18.37372	18.36966	4.06	0.4727
		60	362.16	18.36966	18.3679	5.82	0.5658
		90	543.24	18.3679	18.3669	6.82	0.5634
		120	724.32	18.3669	18.36658	7.14	0.5707
		150	905.4	18.36658	18.36559	8.13	0.5756
		180	1086.48	18.36559	18.36511	8.61	0.5911
	15	30	271.62	18.38367	18.37734	6.33	0.4055
		60	543.24	18.37734	18.37554	8.13	0.5303
		90	814.86	18.37554	18.37469	8.98	0.5432
		120	1086.48	18.37469	18.37375	9.92	0.549
		150	1358.1	18.37375	18.37291	10.76	0.552
		180	1629.72	18.37291	18.37259	11.08	0.5577
	20	30	362.16	18.39668	18.38963	7.05	0.3348
		60	724.32	18.38963	18.38793	8.75	0.4718
		90	1086.48	18.38793	18.38659	10.09	0.4739
		120	1448.64	18.38659	18.38501	11.67	0.485
		150	1810.8	18.38501	18.3841	12.58	0.4893
		180	2172.96	18.3841	18.38308	13.6	0.4923
40	5	30	90.54	17.56126	17.55738	3.88	0.5272
		60	181.08	17.55738	17.55338	7.88	0.5678
		90	271.62	17.55338	17.55046	10.8	0.5842
		120	362.16	17.55046	17.5473	13.96	0.598
		150	452.7	17.5473	17.54453	16.73	0.6438
		180	543.24	17.54453	17.5437	17.56	0.6647
	10	30	181.08	17.58058	17.57304	7.54	0.4604
		60	362.16	17.57304	17.56709	13.49	0.5229
		90	543.24	17.56709	17.56456	16.02	0.5907
		120	724.32	17.56456	17.56256	18.02	0.6062
		150	905.4	17.56256	17.56208	18.5	0.6163
		180	1086.48	17.56208	17.56126	19.32	0.6275

Table B 3 (contd..)

Load (N)	Frequency (Hz)	Time (min)	Sliding distance(m)	Weight before(g)	Weight after(g)	Total weight loss(mg)	COF
40	15	30	271.62	17.59831	17.58865	9.66	0.4011
		60	543.24	17.58865	17.5847	13.61	0.4962
		90	814.86	17.5847	17.58259	15.72	0.5375
		120	1086.48	17.58259	17.58085	17.46	0.5596
		150	1358.1	17.58085	17.5798	18.51	0.5652
		180	1629.72	17.5798	17.57884	19.47	0.5788
	20	30	362.16	17.61781	17.60957	8.24	0.3715
		60	724.32	17.60957	17.60733	10.48	0.4585
		90	1086.48	17.60733	17.60483	12.98	0.479
		120	1448.64	17.60483	17.60205	15.76	0.4907
		150	1810.8	17.60205	17.60012	17.69	0.5116
		180	2172.96	17.60012	17.59831	19.5	0.5127
60	5	30	90.54	22.23098	22.22525	5.73	0.4824
		60	181.08	22.22525	22.222	8.98	0.5104
		90	271.62	22.222	22.21863	12.35	0.5608
		120	362.16	22.21809	22.21756	12.88	0.5704
		150	452.7	22.21756	22.21585	14.59	0.6282
		180	543.24	22.21585	22.21575	14.69	0.6208
	10	30	181.08	22.13911	22.12773	11.38	0.4083
		60	362.16	22.12773	22.12275	16.36	0.526
		90	543.24	22.12275	22.11959	19.52	0.5103
		120	724.32	22.11959	22.11805	21.06	0.5442
		150	905.4	22.11805	22.11694	22.17	0.5496
		180	1086.48	22.11694	22.11542	23.69	0.5861
	15	30	271.62	22.19481	22.18232	12.49	0.4015
		60	543.24	22.18232	22.17755	17.26	0.4982
		90	814.86	22.17791	22.17484	20.33	0.5383
		120	1086.48	22.17484	22.17308	22.09	0.5693
		150	1358.1	22.17308	22.17199	23.18	0.5704
		180	1629.72	22.17199	22.17065	24.52	0.5771
	20	30	362.16	22.17065	22.15739	13.26	0.3702
		60	724.32	22.15827	22.15057	20.96	0.4338
		90	1086.48	22.15057	22.14753	24	0.4655
		120	1448.64	22.14753	22.14446	27.07	0.479
		150	1810.8	22.14446	22.14171	29.82	0.486
		180	2172.96	22.14171	22.13854	32.99	0.5001

Table B 4 Reciprocating wear tests data for solution treated 60NiTi

Load (N)	Frequency (Hz)	Time (min)	Sliding distance(m)	Weight before(g)	Weight after(g)	Total weight loss(mg)	COF
20	5	30	90.54	19.36731	19.36613	1.18	0.4964
		60	181.08	19.36613	19.36498	2.33	0.5176
		90	271.62	19.36498	19.3646	2.71	0.5252
		120	362.16	19.3646	19.36368	3.63	0.527
		150	452.7	19.36368	19.36297	4.34	0.5661
		180	543.24	19.36297	19.36266	4.65	0.5633
	10	30	181.08	19.37241	19.37053	1.88	0.4777
		60	362.16	19.37053	19.36813	4.28	0.5283
		90	543.24	19.36813	19.36766	4.75	0.5407
		120	724.32	19.36766	19.36657	5.84	0.5428
		150	905.4	19.36657	19.36628	6.13	0.5428
		180	1086.48	19.36628	19.36554	6.87	0.5467
	15	30	271.62	19.38056	19.37713	3.43	0.4379
		60	543.24	19.37713	19.37597	4.59	0.4941
		90	814.86	19.37597	19.37543	5.13	0.5202
		120	1086.48	19.37543	19.3744	6.16	0.5242
		150	1358.1	19.3744	19.37362	6.94	0.5119
		180	1629.72	19.37362	19.37241	8.15	0.5215
	20	30	362.16	19.39215	19.38723	4.92	0.4101
		60	724.32	19.38723	19.38618	5.97	0.4074
		90	1086.48	19.38618	19.38483	7.32	0.4373
		120	1448.64	19.38483	19.38338	8.77	0.4263
		150	1810.8	19.38338	19.38234	9.81	0.4043
		180	2172.96	19.38234	19.38056	11.59	0.429
40	5	30	90.54	18.96206	18.96036	1.7	0.4755
		60	181.08	18.96036	18.95823	3.83	0.4964
		90	271.62	18.95823	18.95584	6.22	0.53
		120	362.16	18.95584	18.95447	7.59	0.549
		150	452.7	18.95447	18.95288	9.18	0.5304
		180	543.24	18.95288	18.95174	10.32	0.5588
	10	30	181.08	18.95372	18.94839	5.33	0.4773
		60	362.16	18.94839	18.94504	8.68	0.492
		90	543.24	18.94504	18.94268	11.04	0.5382
		120	724.32	18.94268	18.94122	12.5	0.57
		150	905.4	18.94122	18.94003	13.69	0.5629
		180	1086.48	18.94003	18.93853	15.19	0.5758

Table B 4 (contd..)

Load (N)	Frequency (Hz)	Time (min)	Sliding distance(m)	Weight before(g)	Weight after(g)	Total weight loss(mg)	COF
40	15	30	271.62	18.99331	18.98704	6.27	0.401
		60	543.24	18.98704	18.9837	9.61	0.4823
		90	814.86	18.9837	18.98168	11.63	0.5226
		120	1086.48	18.98168	18.98015	13.16	0.5404
		150	1358.1	18.98015	18.97884	14.47	0.5444
		180	1629.72	18.97884	18.9769	16.41	0.5492
	20	30	362.16	19.01173	19.00484	6.89	0.3515
		60	724.32	19.00484	19.00198	9.75	0.4186
		90	1086.48	19.00198	18.99952	12.21	0.4522
		120	1448.64	18.99952	18.99745	14.28	0.4554
		150	1810.8	18.99745	18.995	16.73	0.4711
		180	2172.96	18.995	18.99331	18.42	0.4884
60	5	30	90.54	20.84303	20.8397	3.33	0.4911
		60	181.08	20.8397	20.83653	6.5	0.5114
		90	271.62	20.83653	20.83379	9.24	0.5272
		120	362.16	20.83379	20.83069	12.34	0.5391
		150	452.7	20.83069	20.8281	14.93	0.5653
		180	543.24	20.8281	20.82673	16.3	0.6253
	10	30	181.08	20.78427	20.7777	6.57	0.4621
		60	362.16	20.7777	20.77215	12.12	0.4767
		90	543.24	20.77215	20.77019	14.08	0.5327
		120	724.32	20.77019	20.76884	15.43	0.554
		150	905.4	20.76884	20.767	17.27	0.5553
		180	1086.48	20.767	20.76595	18.32	0.5704
	15	30	271.62	20.80128	20.79047	10.81	0.3969
		60	543.24	20.79047	20.78883	12.45	0.4687
		90	814.86	20.78883	20.78746	13.82	0.4755
		120	1086.48	20.78746	20.78667	14.61	0.5001
		150	1358.1	20.78667	20.78552	15.76	0.5136
		180	1629.72	20.78552	20.78427	17.01	0.5158
	20	30	362.16	20.82673	20.8157	11.03	0.3271
		60	724.32	20.8157	20.81162	15.11	0.4133
		90	1086.48	20.81162	20.80861	18.12	0.4185
		120	1448.64	20.80861	20.80649	20.24	0.4229
		150	1810.8	20.80649	20.80211	24.62	0.4602
		180	2172.96	20.80211	20.80032	26.41	0.4641